Experimental Study of Roughness Effect on Turbulent Shear Flow Downstream of a Backward Facing Step

by

Ebenezer Ekow Essel

A Thesis submitted to the Faculty of Graduate Studies of

The University of Manitoba

in partial fulfilment of the requirements of the degree of

MASTER OF SCIENCE

Department of Mechanical and Manufacturing Engineering

University of Manitoba

Winnipeg

ABSTRACT

An experimental study was undertaken to investigate the effect of roughness on the characteristics of separated and reattached turbulent shear flow downstream of a backward facing step. Particle image velocimetry technique was used to conducted refined velocity measurements over a reference smooth acrylic wall and rough walls produced from sandpaper 36 and 24 grits positioned downstream of a backward facing step, one after another. Each experiment was conducted at Reynolds number based on the step height and centerline mean velocity of 7050. The results showed that sandpaper 36 and 24 grits increased the reattachment length by 5% and 7%, respectively, compared with the value obtained over the smooth wall. The distributions of the mean velocities, Reynolds stresses, triple velocity correlations and turbulence production are used to examine roughness effects on the flow field downstream of the backward facing step. Two-point auto-correlation function and proper orthogonal decomposition (POD) are also used to investigate the impact of wall roughness on the large scale structures.

ACKNOWLEDGEMENT

I would like to express my sincere gratitude to my academic advisor Dr. Mark F. Tachie for his invaluable support and guidance during this research.

The financial support provided by University of Manitoba in the form of awards is greatly appreciated.

I would like to acknowledge the technical support from Paul Krueger and also express my gratitude to Dr. Karen Flack for the profiling plots of my rough walls.

DEDICATION

This thesis is dedicated to my parents, George and Rebecca Mensah, for training me to be humble and hardworking.

TABLE OF CONTENTS

LIST OF FIGURES

LIST OF TABLES

NOMENCLATURE

English

B	logarithmic law constant
C_f	skin-friction coefficient
C_p	pressure coefficient
$f_\#$	f-number of camera lens
g	acceleration due to gravity
h	step height
H	shape factor
k	turbulent kinetic energy
k_s	equivalent sand grain roughness
Ku	flatness
L_r	reattachment length
L_{xuu}	streamwise extent of R_{uu}
L_{yuu}	wall normal extent of R_{uu}
L_{xvv}	streamwise extent of R_{vv}
L_{yvv}	wall normal extent of R_{vv}
P_k	production of turbulent kinetic energy
$Re_{\theta,}$	Reynolds number based on momentum thickness and freestream velocity
Re_h	Reynolds number based on step height and freestream velocity
R_{uu}	streamwise two-point auto-correlation function
R_{vv}	wall-normal two-point auto-correlation function
Sk	skewness
u	streamwise turbulence intensity
u^2	streamwise Reynolds normal stress

U	mean streamwise velocity
U_e	freestream mean velocity
U_{max}	local maximum mean velocity
U_τ	friction velocity
u^3, u^2v, uv^2, v^3, uw^2, vw^2	triple velocity correlations
$-uv$	Reynolds shear stress
v	wall-normal turbulence intensity
v^2	wall normal Reynolds normal stress
v_s	settling velocity
V	wall-normal mean velocity
w^2	spanwise Reynolds normal stress
x	streamwise distance
x'	streamwise distance beyond reattachment point normalized by step height
x^*	streamwise distance normalized by step height
y	wall-normal distance
y	wall-normal distance normalized by step height

Greek

δ	boundary layer thickness
δ^*	displacement thickness
δ^+	boundary layer thickness normalized by viscous length scale
δ_ω	vorticity thickness
Δs	local displacement vector

Δt	laser time delay
κ	von Kármán constant
η	Kolmogorov length scale
λ	Taylor micro-scale
ρ_p	particle density
ρ_f	fluid density
θ	momentum thickness
t_r	particle response time
μ_f	dynamic viscosity of the fluid
v	kinematic viscosity
ω	vorticity

Superscript

$(^+)$	normalization with inner variables
$(^*)$	normalization of streamwise or wall-normal distance with step height or normalization of turbulent statistics with freestream or local maximum mean velocity
(')	normalization by step height with reference to the reattachment point

Acronyms

AR	aspect ratio
APG	adverse pressure gradient
BFS	backward facing step
CCD	charged coupled device
DNS	direct numerical simulation
ER	expansion ratio

IA	interrogation area
LDV	laser Doppler anemometry
LES	large eddy simulation
Nd: YAG	neodymium: Yttrium Aluminum Garnet
pdf	probability density function
PIV	particle image velocimetry
POD	proper orthogonal decomposition
PTV	particle tracking velocimetry

CHAPTER 1

INTRODUCTION

1.1 Motivation

Flow separation and reattachment is the entire process of detachment of a boundary layer and its subsequent reattachment and redevelopment after some streamwise distance. Flow separation may be caused by severe adverse pressure gradient and/or sudden changes in the flow geometry. Geometry-induced separated and reattached flows, which are the focus of the present study, occur in many fluid engineering applications such as pipe systems with sudden changes in diameter, diffusers, combustors and flow around buildings. In these and many other applications, flow separations may adversely affect efficiency and performance, and also produce undesirable structural vibrations and noise. In diffusers, for example, flow separation causes loss of pressure rise. In the automobile and aerospace industries, flow separation, to a large extent, increases drag which causes higher fuel consumption. In addition to its diverse practical importance, separated and reattached flows are an important topic in the turbulence research community. In view of their relative complexity compared to classical boundary layers and fully developed channel flows, separated and reattached flows are routinely used as prototypical flow for exploring the characteristics of complex turbulent shear flows, and also as acute test cases for accessing the predictive capability of engineering turbulence models.

Given their fundamental and practical importance, separated and reattached turbulent flows have received considerable research attention over the past decades. Both experimental techniques such as hotwire anemometry, laser Doppler velocimetry (LDV) and particle image velocimetry (PIV) and numerical methodologies such as direct numerical simulation (DNS), large eddy simulation (LES) and turbulence

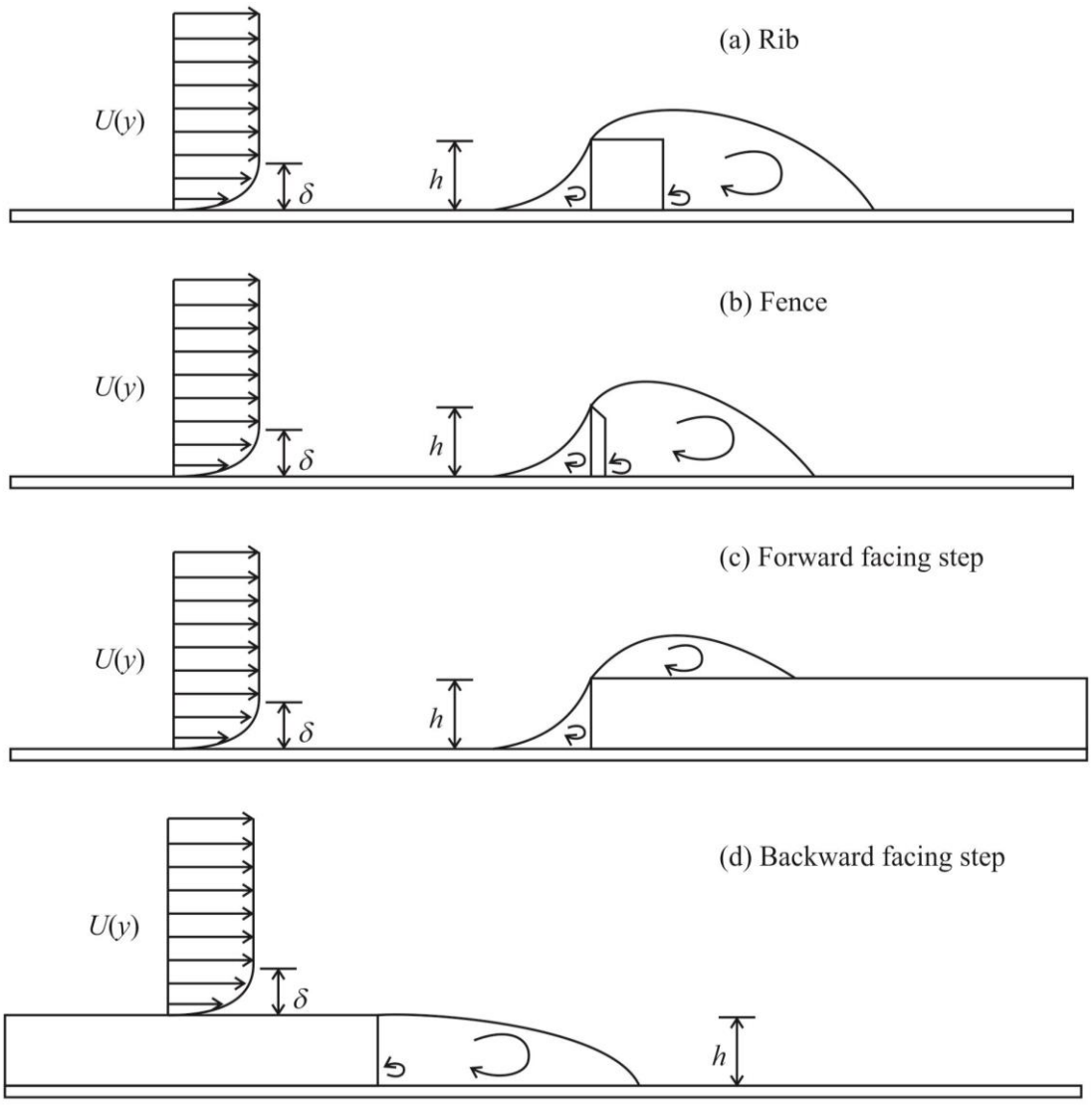

Figure 1.1: Schematic of geometries used to induce flow separation. Note that, *h* is the step or obstacle height and arrows indicate the direction of the flow.

models of varying sophistication have been used to investigate the salient features of separated and reattached flows.

Figure 1.1 shows examples of geometries used to induce separation in previous studies. These include rib, fence, forward facing step and backward facing step (BFS). The BFS is the most extensively used geometry due to its relative simplicity. As can be observed from Figure 1.1, the BFS has only one point of separation, which is fixed at the trailing edge of the step, and a single primary recirculating bubble immediately

downstream of the step whereas the other geometries (rib, fence, and forward facing step) have multiple separation points and recirculating bubbles. Despite its geometric simplicity, the BFS possesses all the salient features of separated and reattached flows.

Although wall roughness is a defining feature in many practical fluid engineering applications, most of the research on separated and reattached turbulent flows to date focused on smooth walls. In fact, at infinite Reynolds number, all surfaces become hydraulically rough. Wall roughness may also be caused by manufacturing defects, corrosion, degradation or biomass accumulation over a period of time. Wall roughness in canonical turbulent boundary layers is observed to cause a considerable modification of the flow structure and turbulent transport phenomena in the region adjacent to the roughness elements. These modifications may include enhanced mass and momentum transport. The effects of roughness on separated and reattached flows are, however, not well understood.

1.2 Objective and scope of research

The overarching objective of the present study is to investigate the effects of wall roughness on separated and reattached turbulent shear flow downstream of a BFS.

This objective is achieved using an experimental methodology. Specifically, refined velocity measurements are conducted over the following three wall conditions; a reference smooth wall made from a clear acrylic plate and rough walls produced from sandpaper 36 and 24 grits positioned downstream of a BFS, one after another. A particle image velocimetry (PIV) system is used to perform the velocity measurements. The velocity data over the three wall conditions were then post-processed to obtain the mean velocities and higher order turbulence statistics. These

statistics were then compared to reveal roughness effects on the flow characteristics. Multi-point turbulence statistics such as two-point correlation functions and proper orthogonal decomposition were also applied to reveal coherent structures within the flow fields, and to investigate the impact of wall roughness on the large scale structures.

The rest of the thesis is organized as follows. A discussion on the salient features of separated and reattached flows over BFS, which is the geometry used in the present study, is presented in Chapter 2. This is followed by a review of the relevant experimental and numerical studies on separated and reattached flows over BFS with smooth and rough downstream walls. Detailed description of the test facility, test conditions, the PIV system used to perform the velocity measurements and the measurement procedure are presented in Chapter 3. In Chapter 4, the effects of roughness on the one-point statistics such as the mean velocities, Reynolds stresses, triple velocity correlations and the production term of the turbulent kinetic energy transport equation are presented and discussed. Discussion on the effects of roughness on coherent structures extracted using two-point auto-correlation function and proper orthogonal decomposition (POD) are also presented in Chapter 4. Conclusions and recommendations for future work are given in Chapter 5.

CHAPTER 2

LITERATURE REVIEW

A review of separated and reattached flows over a backward facing step (BFS) is presented in this chapter. An overview of the salient features of BFS and the characteristics of the three distinct regions of a BFS flow field are first presented. This is followed by presentation and discussion of relevant experimental and numerical studies on separated and reattached flows over both smooth and rough downstream walls.

2.1 Flow features of backward facing step

As stated earlier in Section 1.1, the BFS has the simplest geometry but possesses all the salient features of separated and reattached flows. The flow field over the BFS can be divided into three distinct regions: an upstream region, a recirculation region and a redevelopment region. A schematic of a BFS is shown in Figure 2.1 to demonstrate these distinct regions and also to define some of the principal flow features. The Cartesian coordinate system is adopted with the *x*-coordinate aligned with the

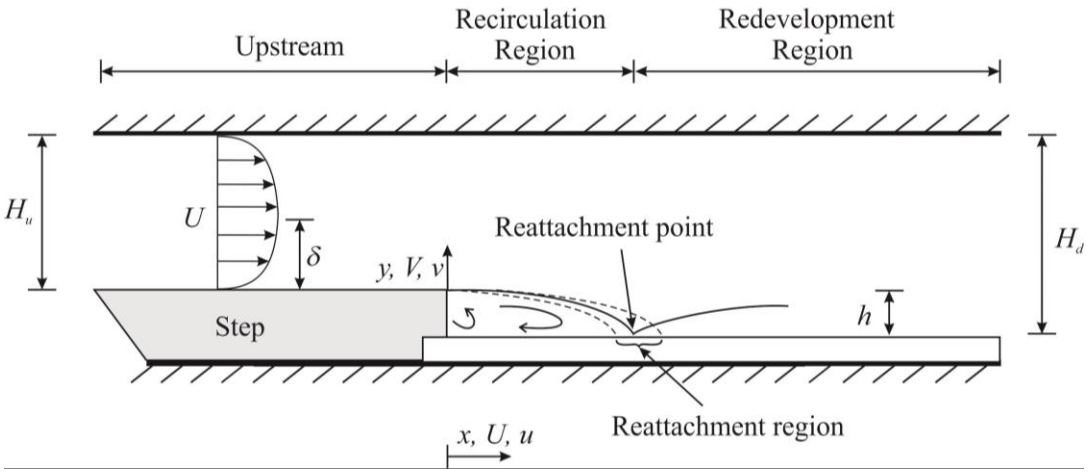

Figure 2.1: Flow features of backward facing step

streamwise direction and the *y*-coordinate is aligned with the wall-normal direction; $x = 0$ is at the trailing edge of the step and $y = 0$ is on the downstream wall. The streamwise and wall-normal mean velocities are denoted, respectively, by U and V while the corresponding root-mean-square values are denoted by u and v, respectively. The upstream channel height is denoted by H_u while the channel height downstream of the trailing edge of the BFS is denoted by H_d.

An approach boundary layer of thickness, δ, separates at the trailing edge of a step of height, h to form a separated shear layer. The separated shear layer curves downwards and reattaches onto a downstream wall. Part of the reattached flow is deflected backwards due to a strong adverse pressure gradient (APG) and forms a primary recirculation bubble. The other part of the reattached flow redevelops into a new boundary layer. The region of the flow where the approach boundary layer develops prior to separation is referred to as the upstream region. The region from the trailing edge of the step to the reattachment point is often referred to as the separated or recirculation region and the region after reattachment is referred to as the recovery or redevelopment region. The reattachment region overlaps the recirculation and redevelopment regions, and plays a significant role in the development of both the recirculation and redevelopment regions. The characteristics of the three main regions are discussed in the following sub-sections.

2.1.1 Upstream region

The flow characteristics in the upstream region of the BFS are similar to that of canonical turbulent shear flows such as turbulent boundary layer and fully developed channel flow (Kasagi and Matsunaga, 1995). A typical boundary layer over a flat plate is shown in Figure 2.2. The boundary layer thickness, (δ) is defined as the wall-

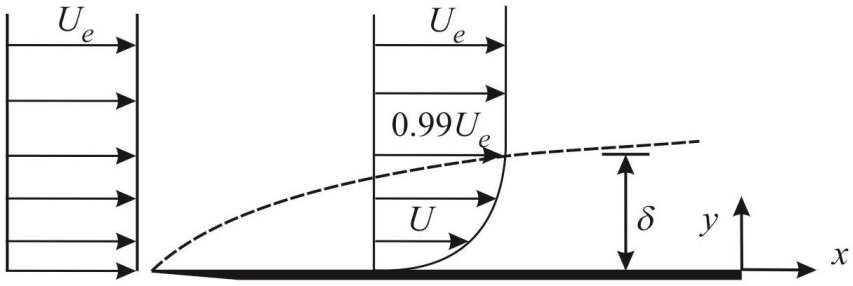

Figure 2.2: Boundary layer over a flat plate

normal distance from the wall to the location where the streamwise mean velocity is 99% of the freestream velocity. Aside the boundary layer thickness, other parameters such as the displacement thickness (δ^*), momentum thickness (θ), shape factor (H) and the skin-friction coefficient (C_f) are used to characterise the boundary layer. The displacement thickness, δ^*, is defined as the wall-normal distance by which the wall would be moved so that the loss of mass flux (due to reduction in uniform flow area by viscous effects) is equivalent to the loss the boundary layer actually causes. Mathematically, δ^* is given by;

$$\delta^* = \int_0^\infty \left(1 - \frac{U}{U_e}\right) dy \tag{2.1}$$

where U is the local streamwise mean velocity and U_e is the freestream velocity.

The momentum thickness, θ, is defined as the wall-normal distance by which the wall would be moved so that the loss of momentum flux is equivalent to the loss the boundary layer actually causes. Mathematically, θ is calculated as;

$$\theta = \int_0^\infty \frac{U}{U_e}\left(1 - \frac{U}{U_e}\right) dy \tag{2.2}$$

The shape factor (H) of the mean velocity profile is defined as the ratio of the displacement thickness to the momentum thickness, $H = \delta^*/\theta$. The skin-fiction coefficient, $C_f = 2\,(U_\tau/U_e)^2$.

The boundary layer profile can be divided into two distinct regions; an inner region and an outer region. In the inner region, viscosity plays an important role on the dynamics of the flow, while the outer region of the boundary layer is dominated by inertial effects. At sufficiently high Reynolds number, an overlap region exists between the inner and outer regions. The friction velocity, U_τ and viscous length scale, $\delta_v = \nu/U_\tau$ (where ν is the kinematic viscosity) are the relevant velocity and length scales in the inner region and they are usually referred to as wall or inner variables. The superscript "$^+$" is often used to denote quantities normalized by inner variables. For example, $U^+ = U/U_\tau$ and $y^+ = yU_\tau/\nu$, where U is the mean velocity and y is the wall-normal distance. The relevant scales in the outer region are the boundary layer thickness, δ and the freestream velocity, U_e. According to Pope, 2000, the inner region spans from the wall ($y^+ = 0$) to $y^+ = 30$. The overlap region extends from $y^+ = 30$ to $0.2\,\delta^+$ while the outer region extends from $y^+ = 30$ to δ^+.

The mean velocity distribution in the inner region is given functionally as

$$U^+ = f(y^+) \tag{2.3}$$

The law of the wall ($U^+ = y^+$) is valid from the wall to $y^+ \approx 5$. The mean velocity distribution in the outer region is expressed functionally as

$$U_e^+ - U^+ = g(y/\delta, \beta) \tag{2.4}$$

where β is a dimensionless pressure gradient parameter. In the overlap region, the mean velocity distribution is described by the classical logarithmic (log) law,

$$U^+ = 1/\kappa \, ln \, y^+ + B \tag{2.5}$$

where κ is the von Kármán constant and B is the logarithmic constant (Millikan, 1938).

2.1.2 Recirculation region

The recirculation region consists of the separated shear layer and the recirculation bubble beneath the shear layer. Through flow visualization, Driver et al., 1987 and Troutt et al., 1984 observed that the separated shear layer has vertical fluctuations, often referred to as flapping, which causes the reattachment point to oscillate within the reattachment region. Westphal et al., 1984 suggested that the streamwise location where the near wall flow moves forward 50% of the time can be used to determine the mean reattachment point. Other methods such as the streamwise location of the mean dividing streamline (Kasagi and Matsunaga, 1995), zero mean velocity (Armaly et al., 1983), zero skin-friction coefficient (Jovic and Driver, 1995) and zero stream function (Le et al., 1997) on the downstream wall have been used in previous studies to estimate the reattachment point. The reattachment lengths reported in previous studies span from 4h to 8h and these values depend on a combination of geometry and initial flow conditions which will be discussed in Section 2.2.

The separated shear layer is associated with energetic large scale structures that are responsible for enhanced turbulence levels in the recirculation region as compared to the redevelopment region. In the reattachment region, the effects of strong APG and intense interaction of the shear layer with the wall cause a rapid decay of the Reynolds stresses (Simpson, 1989).

Beneath the separated shear layer is a primary recirculating bubble and secondary counter-rotating bubble at the corner of the step and the downstream wall. The secondary recirculating bubble is often referred to as a corner eddy. The primary recirculating bubble is characterised by significant backflow mean velocities. The maximum streamwise backflow velocity is approximately 20% of the approach velocity (Eaton and Johnston, 1981). Kasagi and Matsunaga, 1995 observed a maximum wall-normal velocity of approximately 8% of the approach velocity.

2.1.3 Redevelopment region

Downstream of the reattachment point, a new boundary layer develops. The recovery of the mean flow may take more than 20 step heights, and the inner region is observed to recover faster than the outer region (Jovic and Driver, 1995; Simpson, 1989). The slower recovery of the outer region is attributed to the persistence of large scale structures due to separation (Simpson, 1989).

2.2 Previous studies on separated and reattached flows

A large number of studies have been performed to improve our understanding of the characteristics of separated and reattached flows over BFS. Eaton and Johnston, 1981 reviewed prior experimental studies and concluded that a combination of geometry, fluid and flow parameters such as initial boundary layer state, boundary layer thickness, freestream turbulence, pressure gradient, expansion ratio ($ER = H_d/H_u$), and aspect ratio ($AR = W/h$, where W is the channel width) affects the flow characteristics within the recirculation and redevelopment regions of a BFS.

A summary of previous studies that investigated the characteristics of separated and reattached flow over a BFS is presented in Table 2.1. The table includes the downstream wall condition of the BFS used, the measurement technique, the

Table 2.1: Summary of some previous studies on separated and reattached turbulent flow over BFS.

Author(s)	**Wall condition**	**Technique**	Re_h	ER	L_r/h	**Quantities**
(Armaly et al., 1983)	Smooth	LDV & DNS	50-5650	1.94	3.5-17.5	U
(Driver and Seegmiller, 1985)	Smooth	LDV & DNS	561340, $\alpha = 0$ & 6^o	1.13	6.2-8.2	U, k, $-uv$, δ^*, θ, ν_t, C_p, *Budget terms*
(Adams and Johnston, 1988)	Smooth	HWA	8000-40000	1.25	5.0-7.0	C_f, δ
(Isomoto and Honami, 1989)	Smooth	HWA	32000	1.50	6.0-8.5	U, u
(Ötügen, 1991)	Smooth	HWA & LDV	16600	1.50-3.00	6.0-7.0	U, u, C_p
(Jovic and Driver, 1995)	Smooth	HWA & LOI	5000-37500	1.09-1.20	5.4-6.9	U, C_f
(Le et al., 1997)	Smooth	DNS	5100	1.20	6.3	U, C_f, u, v, w, $-uv$, u^2, v^2, *Budget terms*
(Kasagi and Matsunaga, 1995)	Smooth	PTV	5540	1.50	6.51	U, u, v, w,$-uv$, u^3, u^2v, uv^2,v^3, uw^2, u^2w, *Budget terms*
(Piirto et al., 2003)	Smooth	PIV	15000	1.50	6.2	U,V,W,u,v,w,u^2,v^2,$-uv$,u^2w,v^2w,w^3, *Budget terms*
(Kostas et al., 2002)	Smooth	PIV	4660	1.02	4.8	U, ω, u^2, v^2, $-uv$, $-uw$, k
(Kim and Chung, 1995)	Rough; p/k = 1.40-5.70	Split film sensor	26500	1.15	5.8-6.0	U, u^2, H
(Ampadu-Mintah et al., 2012)	Rough; wire mesh, sandpaper 36 grit	PIV	2700		5.5-5.9	U, u,v,$-uv$,δ_ω, R_{uu}, R_{vv}

Reynolds number based on the step height and the freestream velocity (Re_h), expansion ratio (ER), reattachment length (L_r/h) and the flow quantities measured in each of these studies. In the table, α refers to angle of inclination of the top wall of the

channel from the trailing edge of the step, LDV denotes laser Doppler velocimetry, DNS denotes direct numerical simulation, HWA refers to hotwire anemometry and LOI denotes laser-oil interferometer. For the flow quantities, k is the turbulent kinetic energy, u^2 and v^2 are the streamwise and wall-normal Reynolds normal stresses, respectively, $-uv$ is the Reynolds shear stress, ν_t is kinematic eddy viscosity, C_p is pressure coefficient, and the triple velocity correlations are u^3, u^2v, uv^2, v^3, uw^2, and u^2w. The vorticity is represented by ω, δ_ω is the vorticity thickness and R_{uu} and R_{vv} are the streamwise and wall-normal two-point auto-correlation functions, respectively.

Armaly et al., 1983 investigated the flow characteristics of a BFS for a range of Reynolds number based on the step height and approach velocity, $50 \leq Re_h \leq 5650$ and found that the reattachment length varied with the state of the upstream boundary layer. Specifically, the reattachment length increased from $3.0h$ to $17.8h$ for a laminar flow ($Re_h < 850$), then decreased to $6.0h$ for a transitional flow ($850 < Re_h < 4700$) but remained approximately constant at $8.0h$ for a fully turbulent flow ($Re_h > 4700$).

Adams and Johnston, 1988 conducted hot-wire measurements over a BFS at $Re_h = 8000 - 40000$. For a fixed Re_h, the upstream boundary layer thickness, δ/h was changed, independent of Re_h, using a combination of upstream porous - wall suction to thin the boundary layer and trips to thicken it. It was observed that, at a given Re_h, the reattachment length increased with upstream boundary layer thickness if $\delta/h < 0.2$ but remained approximately constant for $\delta/h \geq 0.2$. For example, at $Re_h = 36000$, the reattachment length was found to increase by 30% when δ/h increased from 0 to 0.2.

Isomoto and Honami, 1989 investigated the effect of freestream turbulence on the characteristics of the separated shear layer and the reattachment length. Two-dimensional rods were positioned upstream of the BFS to produce different levels of

freestream turbulence. The reattachment length was observed to decrease with an increase in freestream turbulence. For example, when the turbulence level increased from 0.10 to 0.12, the reattachment length was observed to decrease by 31%. Eaton and Johnston, 1981 also compiled previous results and concluded that elevated freestream turbulence level decreases the reattachment length. Ötügen, 1991 argued that an increase in freestream turbulence increases the rate of growth of the shear layer which results in a shorter reattachment length.

Durst and Tropea, 1981 and Eaton and Johnston, 1981 reviewed previous studies and concluded that the reattachment length increases with expansion ratio if $ER < 1.8$. Eaton and Johnston, 1981, for example, showed a trend that suggests that the reattachment length increases by 30% when *ER* increases from 1.0 to 1.7. In the study by Ötügen, 1991, the reattachment length was observed to decrease by 9% when *ER* was increased from 1.5 to 3.13. Ötügen, 1991 attributed the decrease in reattachment length to enhanced turbulence level in the separated shear layer for larger expansion ratios.

De Brederode and Bradshaw, 1972 showed that the effect of secondary flow from the side walls on the flow characteristics at the mid-span of a BFS channel is negligible for aspects ratio, $AR > 10$. For lower aspect ratios ($AR < 10$), the flow characteristics downstream of the BFS are three-dimensional and the reattachment length increases if the upstream boundary layer is laminar but decreases for a fully turbulent boundary layer.

Driver and Seegmiller, 1985 studied the effect of adverse pressure gradient (APG) on the flow characteristics using a channel whose top wall was inclined from the trailing edge of the step at angles, $0^o \leq \alpha \leq 10^o$. The reattachment length increased with

increasing APG. For example, the reattachment length increased by approximately 65% when the angle was increased from 0° to 10°. It was found that APG increased the spread rate of the separated shear layer. The momentum and displacement thickness in the recirculation and redevelopment regions were observed to increase with APG but the mean velocity, Reynolds stresses and triple velocity correlations were not significantly affected by APG.

Jovic and Driver, 1995 investigated the recovery of the mean flow to that of canonical wall-bounded turbulent flows using hotwire anemometry. A laser-Oil Interferometer was used to obtain an independent measurement of the wall-shear stress. It was found that the mean velocity profiles shifted downwards from the classical log law in the early region of flow redevelopment (i.e., for profiles obtained at $x/h < 25$). The recovery of the mean flow was found to start from $x/h = 25$ and the inner region developed faster than the outer region. It was also argued that the Clauser plot technique, which is a method of estimating the friction velocity, U_τ by fitting the streamwise mean velocity to the classical log law, is not appropriate in the early redevelopment region because the classical log law is not valid in this region.

Le et al., 1997 used direct numerical simulation (DNS) to study the flow characteristics within the recirculation and redevelopment regions downstream of a BFS. It was found that the streamwise mean velocity profiles shifted downwards from the classical log law for profiles obtained at $x/h \leq 20$. These observations are in good agreement with earlier results presented by Jovic and Driver, 1995. It was also found that the turbulence kinetic energy budget was not in local equilibrium (i.e., production $\neq$ dissipation) in the recirculation region. The peak of dissipation was observed to be 60% of the peak of production. Unlike canonical wall-bounded turbulent boundary

flows, turbulent diffusion was observed to contribute significantly to turbulent kinetic energy budget in the recirculation region.

Kostas et al., 2002 used particle image velocimetry (PIV) technique and proper orthogonal decomposition (POD) to examine the dominant flow structures in the recirculation and redevelopment regions of a BFS. Low-order representations of the velocity field were observed to converge towards the PIV results as the number of POD modes used for the velocity field reconstruction increased. The small-scale and orderly vortex interactions were observed to be responsible for the most intense turbulent kinetic energy production in the flow. The large scale structures were found to be largely responsible for the persistent streamwise Reynolds normal stress and Reynolds shear stress in the flow downstream of reattachment, while the wall-normal Reynolds normal stress distribution was governed predominantly by the fine scale structures.

In contrast to the large number of experimental and numerical investigations of turbulent flows over a smooth wall downstream of a BFS, our understanding of roughness effects on separated and reattached turbulent shear flows downstream of a backward facing step is limited to the experimental studies performed by Ampadu-Mintah et al., 2012 and Kim and Chung, 1995.

Kim and Chung, 1995 investigated the effects of roughness on the flow characteristics downstream of a BFS. In their experiments, the BFS was kept smooth but the bottom wall downstream of the step was roughened using two-dimensional transverse square ribs of varying pitch-to-height ratios, p/k = 1.43, 3.50 and 5.71. The measurements were conducted using split film sensor. As shown in Table 2.1, only the reattachment length, streamwise mean velocity and streamwise Reynolds normal stress were

reported. The streamwise mean velocity measurements extended from the tailing edge of the step to 30 step heights but the streamwise Reynolds normal stress measurements were limited to only the recirculation and early redevelopment regions ($x/h < 8$). It was found that the reattachment length for the reference downstream smooth wall and $p/k = 1.43$ ribs was $5.68h$. At the higher p/k values, roughness was observed to increase the reattachment length by 3.4% but reduced the streamwise mean velocity and turbulence intensity in the recirculation region. In the redevelopment region, it was found that the streamwise mean velocity profiles over the rough walls recovered faster to that of wall-bounded turbulent boundary layer than the profiles over the smooth wall.

More recently, Ampadu-Mintah et al., 2012 conducted a PIV measurement over wire mesh, sandpaper 36 grit and reference smooth wall positioned downstream of a BFS in an open channel turbulent flow. The streamwise extent of measurements spanned from the trailing edge of the BFS to 20 step height. It was concluded that the reattachment length and the growth of the vorticity thickness were independent of roughness. The streamwise mean velocity and spatial structures of two-point correlation of streamwise (R_{uu}) and wall-normal (R_{vv}) velocity fluctuations were also independent of roughness in the recirculation and redevelopment regions. The effect of wall roughness reduced the levels of the Reynolds stresses in the recirculation region but in the redevelopment region, roughness effects were not significant.

2.3 Summary

A combination of geometry, fluid and flow parameters such as initial boundary layer state, initial boundary layer thickness, freestream turbulence, pressure gradient, expansion ratio, and aspect ratio have been observed to affect the flow characteristics

within the recirculation and redevelopment regions. The reattachment length is found to be independent of Reynolds number for a fully turbulent flow (Re_h > 4700). A higher level of freestream turbulence decreases the reattachment length but an increase in expansion ratio (ER < 1. 8) and downstream pressure gradient increases the reattachment length. The mean flow characteristics are two-dimensional at the mid-span of the channel for high aspect ratio, AR > 10. Most of the previous studies were conducted using a BFS with a smooth downstream wall so the effects of roughness on the characteristics of separated and reattached flows downstream of a BFS are not well understood.

CHAPTER 3

EXPERIMENTAL SET-UP AND MEASUREMENT PROCEDURE

This chapter presents a description of the test facility, test conditions, the particle image velocimetry system used to conduct the velocity measurements and the measurement procedure employed in the present study.

3.1 Test facility

The experiments were conducted in a test channel that was inserted into a main recirculating open water channel, as shown in Figure 3.1. The main water channel consists of flow conditioning unit, test section, centrifugal pump, variable speed drive, piping and valves, supporting framework and a filtering system. The test section of the main water channel has dimensions of 2500 mm (length) × 200 mm (height) × 200 mm (internal width). The side and bottom walls are made of Super Abrasion Resistant ® (SAR) clear acrylic plate to facilitate optical access. The recirculating flow is

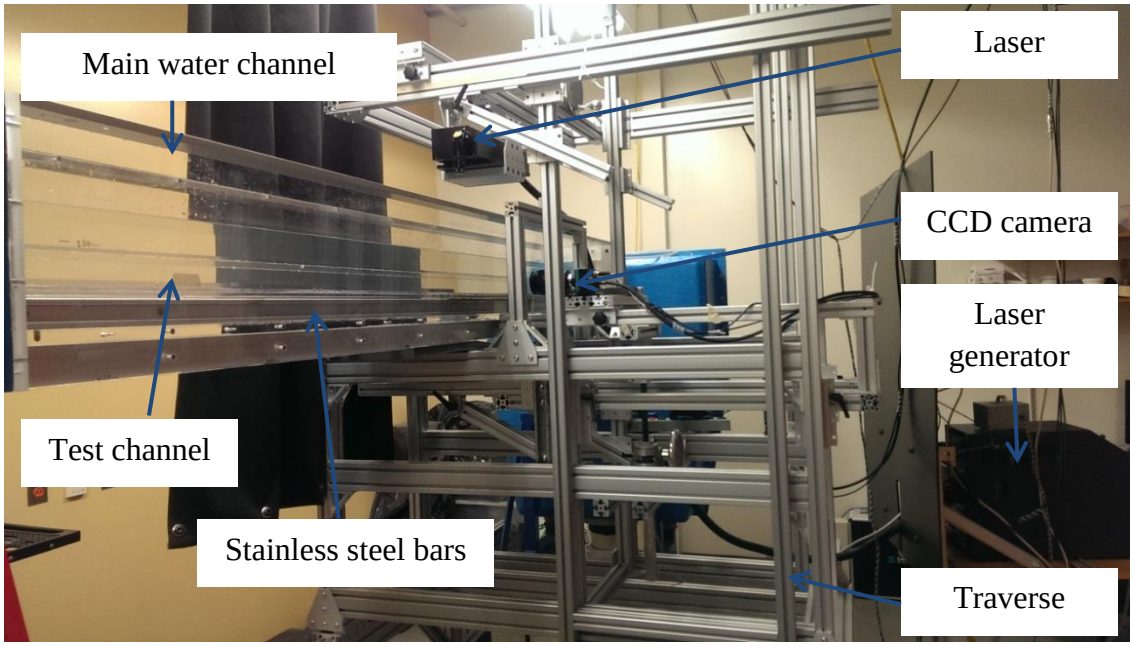

Figure 3.1: Picture of main water channel and components of the PIV system.

driven by a centrifugal pump through the flow conditioning unit at the inlet section of the water channel. A 24 hp variable speed drive motor regulates the speed of the pump. The flow conditioning unit has a wide settling chamber fitted with perforated steel plates and honeycomb followed by a 6:1 contraction section to break down the large scale turbulence and make the flow uniform prior to entering the test section.

3.2 Test channel

The test channel, which was supported by means of two stainless steel bars, was screwed unto the bottom wall of the main water channel (Figure 3.1). A schematic drawing of the test channel is shown in Figure 3.2 (a). The test channel was fabricated from 6 mm thick acrylic plates and it has dimension of 2500 mm (length) × 63 mm (height) × 198 mm (width). The thickness of the side walls reduced the internal

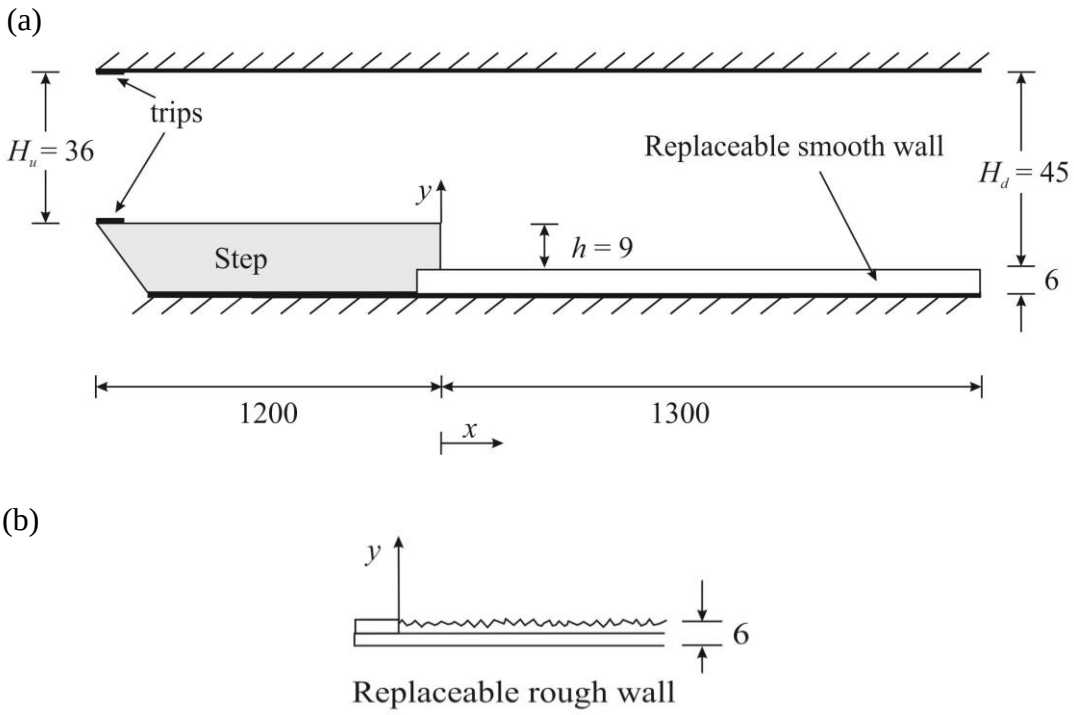

Figure 3.2: Schematic of BFS test channel (a) and replaceable rough wall (b). All dimensions are in millimeters.

width of the test channel to W = 186 mm. The BFS used to induce the flow separation was fabricated from a smooth acrylic plate of nominal height, h = 9 mm, length 1200 mm and width 186 mm. The step was glued on to a 6 mm thick acrylic plate and the resulting insert was screwed on to the bottom wall of the test channel and spanned 1200 mm from the leading edge. The upstream channel height is H_u = 36 mm and the channel height downstream of the trailing edge of the BFS is H_d = 45 mm. The test channel has an aspect ratio ($AR = W/h$) and expansion ratio ($ER = H_d/H_u$) of 21 and 1.25, respectively. The present aspect ratio of AR = 21 is significantly larger than the minimum value of AR = 10 required to establish a two-dimensional mean flow at the mid-span of the test section (De Brederode and Bradshaw, 1972).

3.3 Roughness elements

Three sets of downstream wall or roughness conditions were investigated. In each set, the BFS was kept smooth while a replaceable reference smooth wall and two rough walls of different topography was placed downstream of the step (one after the other) to study the effect of roughness on the velocity field within the recirculation and redevelopment regions. The smooth wall (hereafter denoted by SM) was made of a 6 mm thick clear acrylic plate and spans 1300 mm from the trailing edge of the step. The rough walls were made from sandpaper 36 grit (hereafter denoted by SP-36) and sandpaper 24 grit (hereafter denoted by SP-24) glued unto a 4.5 mm acrylic plate and also spans 1300 mm from the trailing edge of the BFS. Each of the sandpapers had a mean sheet thickness of 1.5 mm so that the combined thickness of the plate and roughness elements wall was 6.0 ± 0.1 mm (Figure 3.2 (b)). Figure 3.3(a) and (b) shows pictures of SP-36 and SP-24. Samples of the rough walls (SP-36 and SP-24) were profiled with a Veeco Wyco NT9100 optical profilometer which utilizes white light interferometry with sub-micron vertical accuracy. The contour plots of the

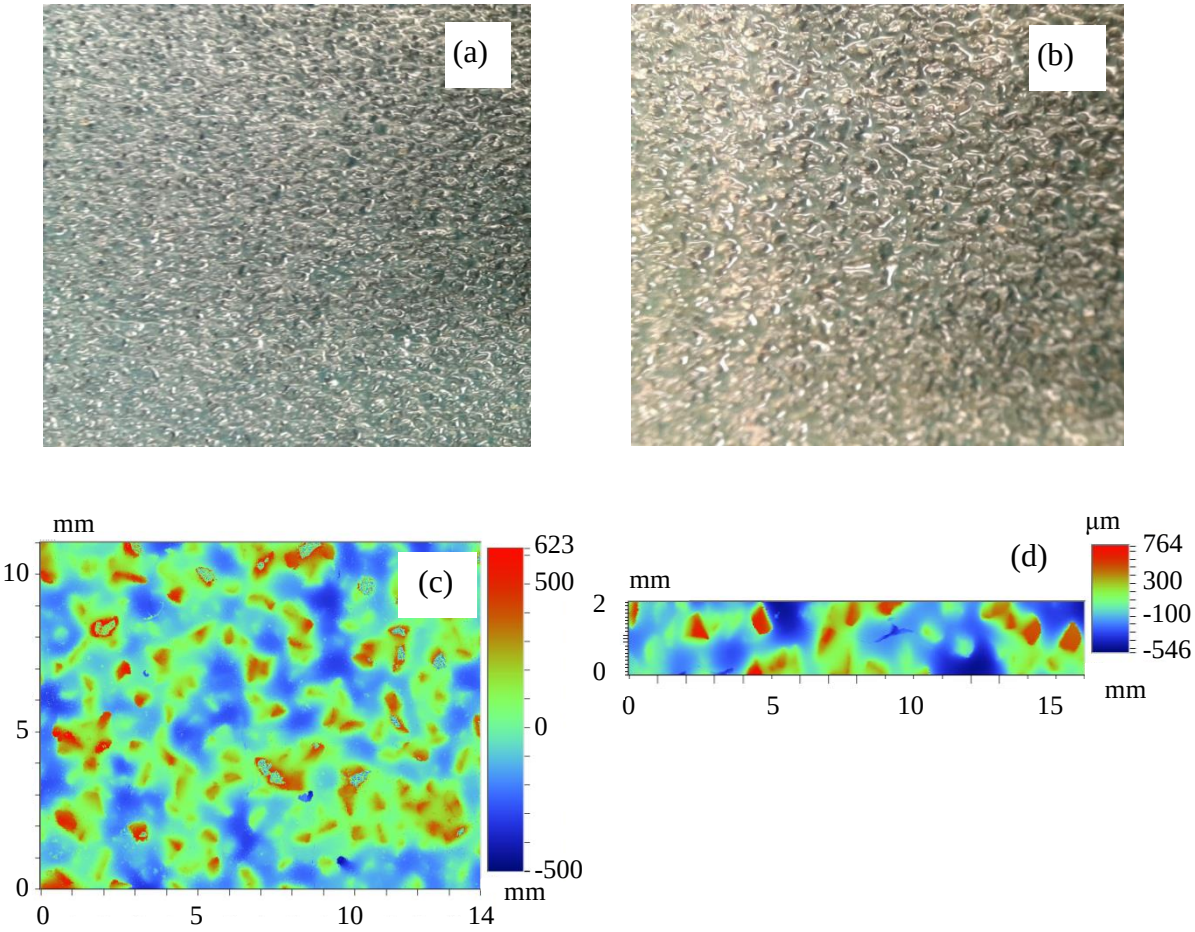

Figure 3.3: Pictures and contour plots of sandpaper 36 grit, SP-36 (a, c) and 24 grit, SP-24 (b, d) topography.

topography of SP-36 and SP-24 are shown in Figure 3.3(c) and (d), respectively, and the surface statistics are summarized in Table 3.1. The average of ten maximum peak-to-trough roughness heights is denoted by k_t, while k_{rms} is the root-mean-square roughness height, Sk is the skewness and Ku is the flatness of the roughness probability density function (pdf). The equivalent sand grain roughness, k_s of the each of the rough walls was estimated from the following formulation proposed by Flack and Schultz, 2010:

$$k_s = 4.43 k_{rms} (1+Sk)^{1.37} \quad (3.1)$$

Table 3.1: Surface statistics of rough walls

Rough wall	k_t (mm)	k_s (mm)	k_{rms} (μm)	*Sk*	*Ku*
SP-36	1.12	1.37	161.07	0.61	3.23
SP-24	1.29	1.70	239.93	0.41	2.39

For SP-36, the equivalent sand grain roughness height, k_s is approximately 20% larger than the average roughness height, k_t. In the case of SP-24, the value of k_s is approximately 30% larger than k_t. The surface statistics also show that the value of k_t of SP-24 is approximately 15% larger than that of SP-36 and values of the skewness imply that there are more peaks than troughs on SP-36 as compared to SP-24.

3.4 PIV system and measurement procedure

A particle image velocimetry (PIV) system was used to conduct detailed velocity measurements in *x*-*y* planes located at mid-span of the test channel. The PIV is a whole-field non-intrusive velocity measurement technique that measures instantaneous velocity vectors simultaneously at thousands of locations within the flow field. Detailed discussion on the basic principles and implementation of the PIV technique are available in many references including Adrian and Westerweel, 2010; Shah, 2008, and will not be repeated here.

In PIV technique, the flow is seeded with tracer particles and the flow field is illuminated by two pulses of laser sheet separated by a time delay, Δt. A couple-charged device (CCD) camera captures the light scattered by the seeding particles on two successive images (image pairs). To obtain the velocity statistics, each image pair is divided into grids of interrogation area (IA) and for each IA, a numerical correlation algorithm is applied to statistically determine the local displacement

vector, Δs, of the particles between the first and second image. The average of the local displacement vector, Δs, of all the particles within an IA, is then divided by the time delay, Δt to obtain the velocity vector within the IA. The numerical correlation algorithm is repeated for all the IAs to obtain the velocity vector map of the flow field captured.

A schematic of the specific PIV system and setup used in the present study is shown in Figure 3.1. The basic components of the PIV comprise double pulsed laser, CCD camera and synchronizer (not shown). In the present study, the flow was seeded with 10 μm fluorescent polymer seeding particles (Rhodamine B) having a specific gravity of 1.19 and refractive index of 1.48. The size of the particles and the refractive index where chosen so as to ensure the seeding particles have good light scattering ability. Since the PIV technique measures the velocity of the particles and not the fluid velocity, it is essential to ensure that the particles follow the flow faithfully. To this end, the particle settling velocity and response time were evaluated. The settling velocity, v_s and response time, t_r were calculated using the following expressions:

$$v_s = \frac{(\rho_\mathrm{p}-\rho_\mathrm{f})g d_\mathrm{p}^2}{18\mu_\mathrm{f}} \tag{3.2}$$

$$t_r = \rho_p \frac{d_p^2}{18\mu_f} \tag{3.3}$$

where ρ_p is the particle density, ρ_f is the fluid density, g is the acceleration due to gravity, d_p is the diameter of the particle and μ_f is the dynamic viscosity of the fluid. The values of the settling velocity and response time of the particles were v_s = 1.04 × 10^{-6} m/s and t_r = 6.61 × 10^{-6} s, respectively. This settling velocity is negligibly small compared with the approach centerline mean velocity (U_e = 0.783 m/s). Similarly, the particle response time is negligibly small in comparison with the

sampling time used in the present study. Based on these analyses, it was concluded that the seeding particles indeed follow the flow faithfully.

The flow field was illuminated using a New Wave Solo Nd:YAG double-pulsed laser that emits green light of 120 mJ/pulse at 532 nm wavelength and 15 Hz repetition rate, and the scattered light from the particles are captured by a 12-bit charge-couple device (CCD) camera with 2048 pixel × 2048 pixel array, 7.4 μm pixel pitch. A synchronizer controlled the trigger rate of the laser and image capturing time of the CCD camera. The fluorescent seeding particles absorb the green laser light and emit orange light at 570 nm wavelength. The CCD camera was equipped with an orange filter with band-pass wavelength of 570 nm. The use of fluorescent particles and orange filter significantly reduced surface glare at the interface between the working fluid (water) and the solid wall, thereby significantly improved the quality of the velocity vectors close to the wall.

The data acquisition was controlled using commercial software (DynamicStudio version 3.40) supplied by Dantec Dynamics. Detailed measurements were obtained in an upstream plane (P0) to characterise the approach flow and 5 other downstream planes (P1 - P5) that extend from the trailing edge of the BFS ($x^* = x/h = 0$) to $x^* = 56$ as illustrated in Figure 3.4. The field of view of each measurement plane was set to 62 mm × 62 mm. Based on preliminary convergence tests (presented and discussed in Section 3.7), a sample size of 6000 instantaneous image pairs was acquired in each plane and post-processed using the adaptive correlation option of DynamicStudio version 3.40. The adaptive correlation algorithm uses a multi-pass fast Fourier transform with a one-dimensional Gaussian peak-fitting function to determine the average particle displacement within the interrogation window to sub-pixel accuracy.

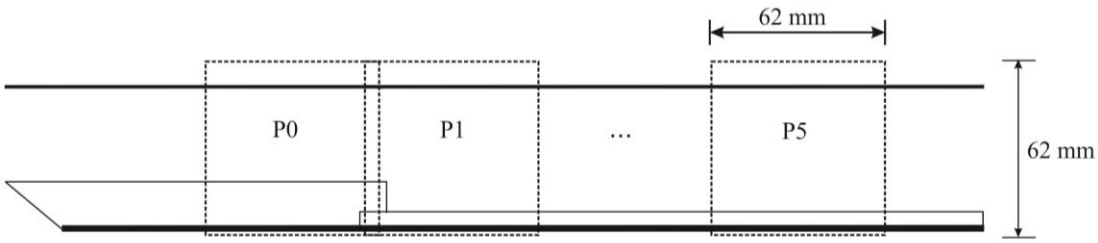

Figure 3.4: Measurement planes

The IA size for the adaptive correlation was set to 32 pixels × 32 pixels with 50% overlap in both the *x* and *y* directions. During the image acquisition, precautionary steps were taken to ensure that the maximum particle displacement was less than 1/4 of the IA size. Therefore, the maximum particle displacement in the streamwise direction was 8 pixels. With 0.1 sub-pixel accuracy and a maximum particle displacement of 8 pixels, the dynamic range was 80.

The spacing between adjacent vectors was $l = 0.054h$ in both the *x* and *y* directions. The Kolmogorov length scale (η) and Taylor micro-scale (λ) were estimated in the upstream plane following the procedure used in prior turbulent boundary layer studies (Johansson and Alfredsson, 1983). Assuming local equilibrium (i.e., production = dissipation), the Kolmogorov length scale (η) and Taylor micro-scale (λ) can be estimated from $\eta = 3\nu/U_\tau$ and $\lambda = 15^{0.5}\tau_\eta U_e$, where $\tau_\eta = \eta^2/\nu$ is the Kolmogorov time scale, ν is the kinematic viscosity. It was determined that, in the upstream plane, the vector spacing corresponds to $l/\eta = 6.0$ and $l/\lambda = 0.02$.

3.5 Test conditions

To enhance a rapid development of the turbulent boundary layer, two trips made from sandpaper 24 grit with dimensions of 70 mm (length) × 186 mm (width) were positioned at the leading edge of the BFS and the top wall with the aid of a double

sided tape (Figure 3.2). In order to ensure that the upstream boundary conditions were similar for all test cases, each of the three sets of experiments was conducted at the same approach centerline mean velocity of U_e = 0.783 m/s. These upstream measurements were obtained in plane (P0) centered at x^* = -7.0h upstream of the trailing edge of the BFS. The Reynolds number based on the step height and the centerline mean velocity was Re_h = 7050. This Reynolds number is high enough to minimize any Reynolds number effects on the reattachment length (Armaly et al., 1983).

Some of the salient parameters of the upstream boundary layer are as follows: boundary layer thickness, δ = 19.8 mm, δ^* = 2.3 mm, θ = 1.7 mm, shape factor, H = 1.36 and Reynolds number based on the momentum thickness, Re_θ = 1320. The shape factor, H obtained in the present study is comparable with H = 1.42 obtained in a zero pressure gradient turbulent boundary layer at Re_θ = 1410 (Spalart, 1988). The ratio of boundary layer thickness to the step height, δ/h > 0.2 implies that the effect of upstream boundary layer on the reattachment length is minimal (Adams and Johnston, 1988).

Profiles of the streamwise mean velocity and the turbulence intensities were also obtained to characterize the state of the approach boundary layer. These profiles are plotted in Figure 3.5 and 3.6. The boundary layer thickness, δ is used as the length scale in Figure 3.5 (a) and 3.6 while the viscous length scale (δ_v) is used in Figure 3.5 (b).

The profile of streamwise mean velocity (Figure 3.5 (a)) shows variation of the streamwise mean velocity from the no-slip condition (U = 0) at the wall (y = 0) to the approach centreline mean velocity (U_e) at the boundary layer thickness ($y = \delta$). The

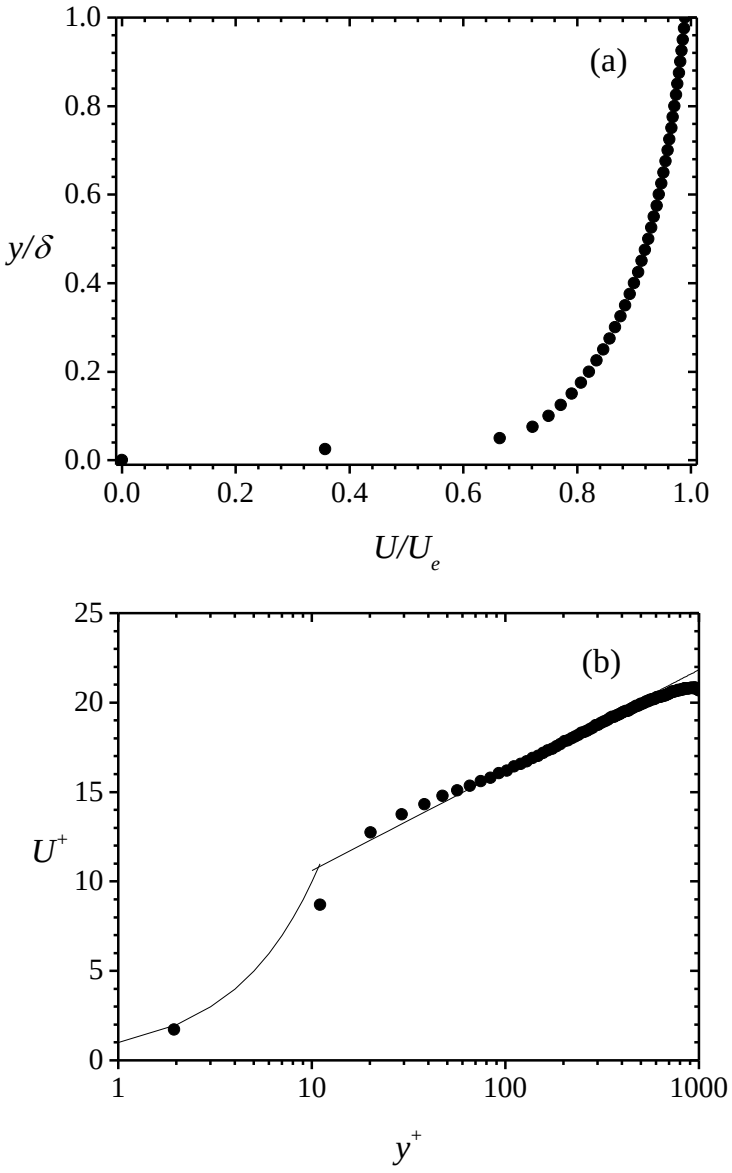

Figure 3.5: Profiles of upstream streamwise mean velocity plotted in outer (a) and inner (b) coordinates.

shape of the streamwise mean velocity profile is significantly altered in the vicinity of the wall where viscous effects are dominant. The mean velocity profile in inner coordinates was fitted to the classical log law as shown in Figure. 3.5 (b) to determine the friction velocity, U_τ and then to estimate the skin-friction coefficient, C_f. The log law constants used were κ = 0.41 and B = 0.50. The log law describes the mean velocity in the region $30 \leq y^+ \leq 450$. The friction velocity, U_τ estimated from the

Clauser plot technique is 0.04 m/s and the skin-friction coefficient, C_f is 0.005. The skin-friction coefficient, C_f was also estimated using the skin-friction correlation for low Reynolds number flow developed by Tachie et al., 2001. This is given as

$$C_f = 4.13\times10^{-2} - 2.68\times10^{-2}(\log Re_\theta) + 6.528\times10^{-3}(\log Re_\theta)^2$$

$$- 5.54\times10^{-3} (\log Re_\theta)^3 \qquad (3.4)$$

The value of C_f = 0.004 obtained from the correlation is 25% less than the value obtained using the Clauser plot technique. The value of C_f obtained from the Clauser plot technique and the correlation are lower than 0.006 reported in fully developed channel turbulent flow at Re_θ = 1280 (Abe et al., 2001). It should be recalled that C_f decreases with increasing Re_θ and since Re_θ = 1320 used in the present study is higher than that of Abe et al., 2001 the difference in the results is expected. The profile of the mean velocity in inner coordinates also show a depressed wake region which is as a result of the relatively low Re_θ and relatively high turbulence level.

The profiles of the streamwise turbulence intensity (u) and wall normal turbulence intensity (v) are shown in Figure 3.6 (a) and (b). In each plot, the turbulence intensities show a rapid increase from the no-slip condition at the wall to a peak value in the immediate vicinity of the wall, and then gradually decay to minimum values at the boundary layer thickness. As expected, the level of the streamwise turbulence intensity is significantly higher than the level of wall-normal turbulence intensity. The peak value of the streamwise turbulence intensity, u/U_e = 0.12 and u^+ = 2.50 while the peak value of the wall-normal turbulence intensity, v/U_e = 0.06 and v^+ = 1.18. The peak values of the turbulence intensities are comparable with values of u^+ = 2.80 and v^+ = 1.10 obtained in a fully developed channel turbulent flow (Abe et al., 2001). The streamwise and wall-normal turbulence intensity at the core of the channel ($y = \delta$) is

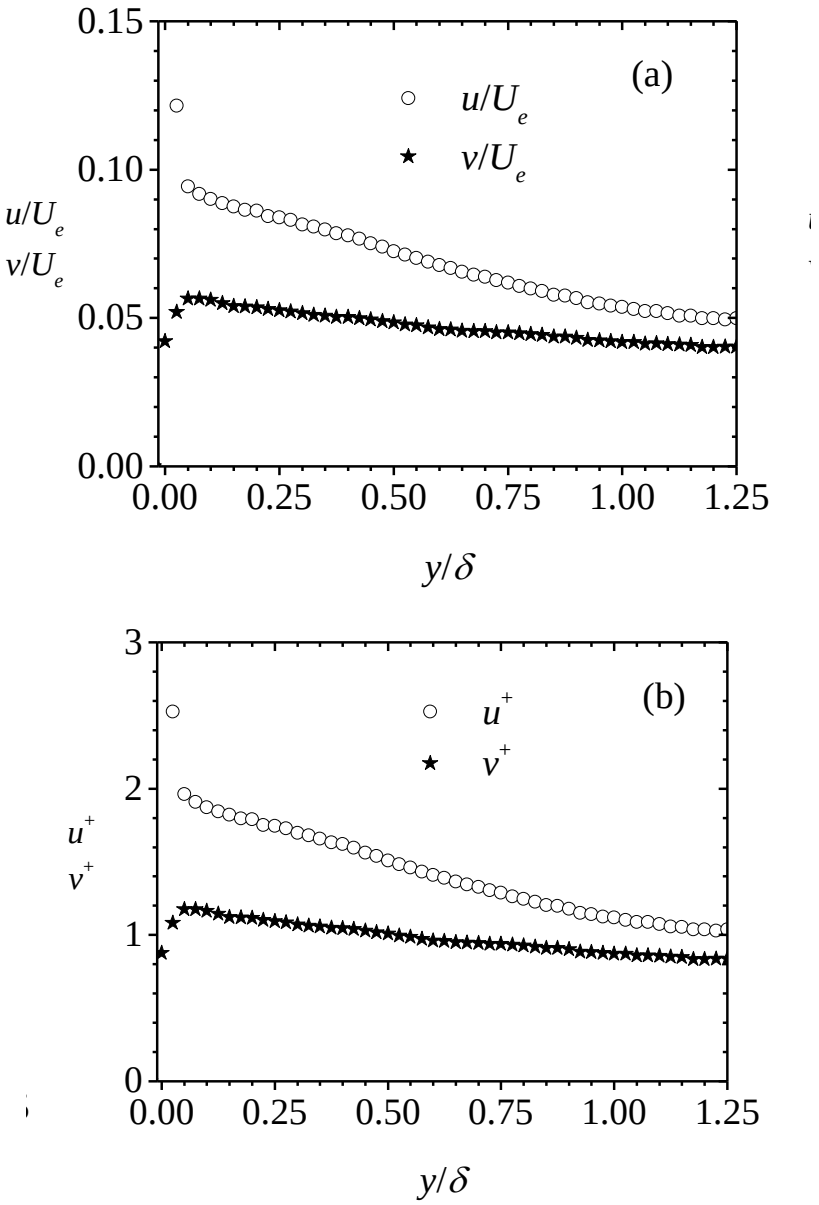

Figure 3.6: Profiles of upstream turbulent intensities plotted in outer (a) and inner (b) coordinates.

u/U_e = 0.04 and v/U_e = 0.03, respectively. The streamwise turbulence intensity at the core of the channel compares well with values of approximately 0.04 ± 0.01 reported in previous channel and zero-pressure gradient turbulent boundary layer studies (Durst et al., 1998).

3.6 Measurement uncertainty

A careful measurement uncertainty analysis was undertaken following the AIAA standard described by Coleman and Steele, 1995 and procedures described in Prasad et al., 1992 and Forliti et al., 2000 for analyzing bias and precision errors in PIV measurements. Detailed uncertainty analysis of the present study is presented in Appendix A. In view of the precautionary measures taken during the measurements, the size of interrogation area, Gaussian peak-fitting algorithm and filtering used to calculate the instantaneous vector maps, and the large number of instantaneous images used to calculate the flow statistics, the uncertainty in the mean velocities at 95% confidence level was estimated to be ± 2% of the streamwise mean velocity. The uncertainties in the turbulence intensities and Reynolds shear stress are, respectively, estimated to be ± 7% and ± 10% of the peak values.

3.7 Convergence test

Prior to acquiring the data for each set of experiments, a convergence test was carried out to determine the sample size required to accurately compute the mean and higher order turbulent statistics. In general, the sample size required depends on the local turbulence level and statistics been measured. Also, the measurement uncertainty is thought to reduce with a larger sample size. Toward this end, 6000 image pairs were acquired in the recirculation region (P1) and the redevelopment region (P3) over sandpaper 24 grit (SP-24). A sample size of N = 2000, 4000 and 6000 were used to calculate the mean velocity, Reynolds stresses and triple velocity correlations. Figure 3.7 and 3.8 shows the results of the convergence test. The error bars on selected data points represent the measurement uncertainty of the respective quantity. As can be observed the differences between the profiles of the mean velocity and Reynolds stresses obtained from the various sample sizes are within measurement uncertainty.

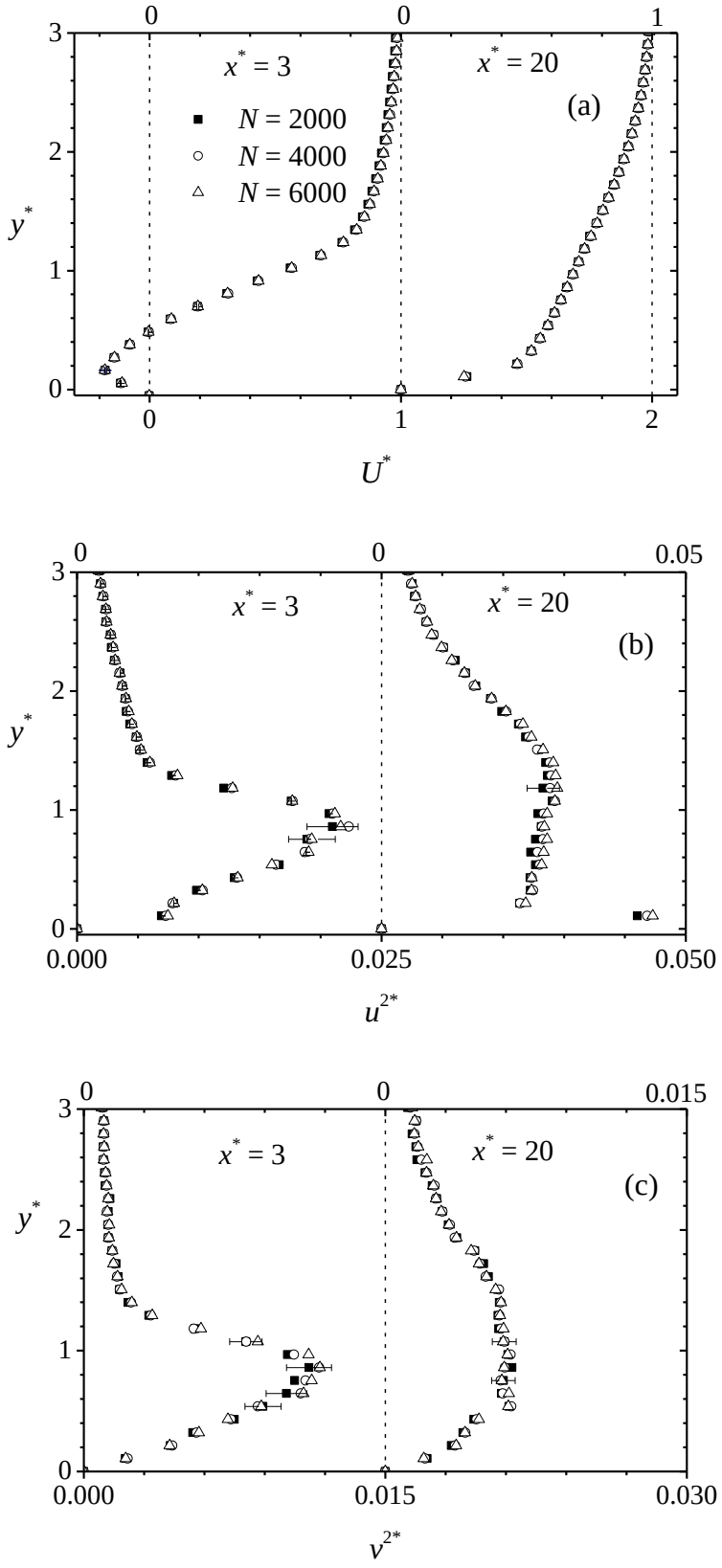

Figure 3.7: Profiles of dimensionless streamwise mean velocity (a), streamwise (b) and wall-normal (c) Reynolds normal stresses computed from sample size, N = 2000, 4000 and 6000 obtained in the recirculation (x^* = 3) and redevelopment (x^* = 20) regions over SP-24.

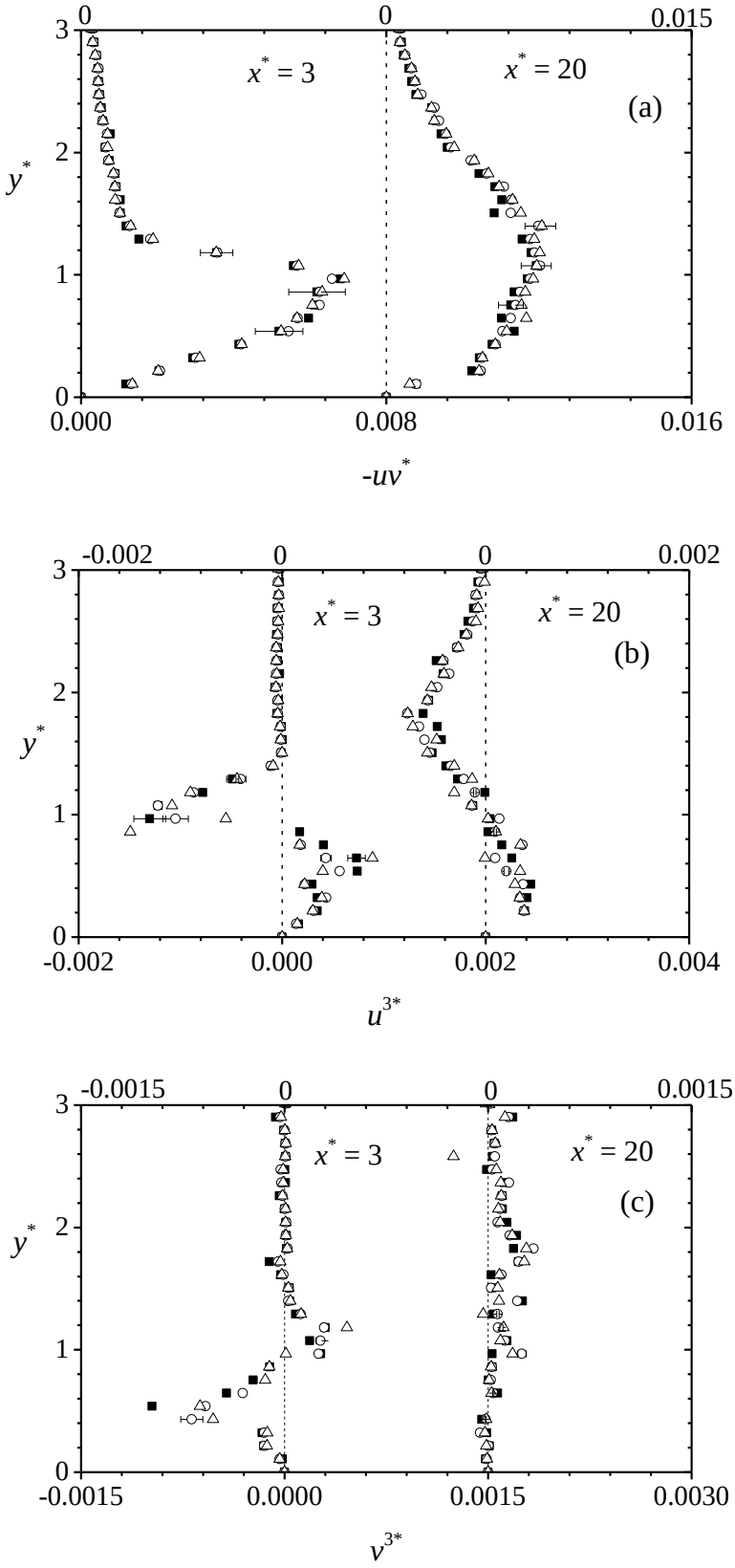

Figure 3.8: Profiles of dimensionless Reynolds shear stress (a) and streamwise (b) and wall-normal (b) triple velocity correlations computed from sample size, N = 2000, 4000 and 6000 obtained in the recirculation (x^* = 3) and redevelopment (x^* = 20) regions over SP-24.

This implies that $N \geq 2000$ is sufficient to obtain statistical convergence of the mean velocity and the Reynolds stresses. In the case of the triple velocity correlations, the profiles obtained from the different sample sizes show significant difference in peak values but similarity of the profiles increases with increasing sample size. As per these observations, 6000 sample size were acquired in each measuring plane and used to compute the mean velocity and higher order turbulent statistics reported in this study. The 6000 image pairs used in the present study is significantly larger than 1024 image pairs used by Kostas et al., 2002, for example, to compute the mean velocity, Reynolds stresses and perform proper orthogonal decomposition in separated and reattached flow downstream of a BFS.

CHAPTER 4

RESULTS AND DISCUSSION

In this chapter, the effects of roughness on the flow dynamics are investigated using both contour plots and profiles of turbulence statistics at selected streamwise locations in the recirculation and redevelopment regions over the smooth wall and rough walls. Contour plots facilitate whole field visualization of the flow characteristics. This is particularly useful in the recirculation and reattachment regions where the flow is evolving very rapidly. The distributions of the turbulence statistics at selected streamwise locations are a more convenient approach to quantify differences among the profiles obtained over the smooth wall and rough walls.

The chapter is organized as follows. In Section 4.1, contour plots of the one-point turbulence statistics including the mean velocities, Reynolds stresses, turbulent kinetic energy and turbulent production are used to examine some of the salient flow features in the recirculation and reattachment regions over the smooth and rough walls. This is followed by Section 4.2 which presents discussion on distributions of one-point turbulence statistics at selected streamwise locations in both the recirculation and redevelopment regions over the smooth and rough walls. In Section 4.3, multi-point turbulence statistics which include two-point auto-correlation function and proper orthogonal decomposition are applied to reveal coherent structures within the recirculation and redevelopment regions, and to investigate the impact of wall roughness on the large scale structures.

4.1 Contour plots of turbulence statistics in the recirculation region

In this section, contour plots of the turbulence statistics in the recirculation region over the smooth wall (SM) and rough walls (SP-36 and SP-24) are presented and

discussed. The contour plots are used to visualize the flow characteristics in the recirculation region as well as examine the effect of roughness on the turbulence statistics. In each of these and subsequent contour plots, the streamwise and wall-normal distances are normalized by the step height, i.e., $x^* = x/h$ and $y^* = y/h$.

4.1.1 Mean streamlines, forward flow fraction and stream function

Mean streamlines are often used to visualize the mean flow direction and reveal the mean flow patterns. The mean streamlines can also be used to estimate the centers of recirculating bubbles and the reattachment point or length over each wall condition. The streamlines shown in Figure 4.1 demonstrate that the approach flow curves downwards from the trailing edge of the step (i.e. point of separation) and attaches on to the downstream wall. Irrespective of the downstream wall condition, the mean streamlines reveal a distinct primary recirculating bubble and a counter- rotating secondary recirculating bubble at the corner of the step. The centers of the primary (P_c) and secondary (S_c) recirculating bubbles over the SM, SP-36 and SP-24 are summarized in Table 4.1. The results presented in the table show that wall roughness did not significantly alter the positions of the centers of the primary and secondary recirculating bubbles.

The reattachment length (L_r) is a parameter that is often used to examine the effects of initial and downstream conditions on the mean flow within the recirculation region. In the present study, the reattachment point was determined using the following four

Table 4.1: Loci of centers of secondary (S_c) and primary (P_c) recirculating bubbles over smooth wall (SM), sandpaper 36 grit (SP-36) and sandpaper 24 grit (SP-24).

	SM (x^*, y^*)	**SP-36 (x^*, y^*)**	**SP-24 (x^*, y^*)**
S_c	0.3, 0.3	0.3, 0.3	0.3, 0.3
P_c	2.8, 0.5	2.8, 0.5	2.9, 0.5

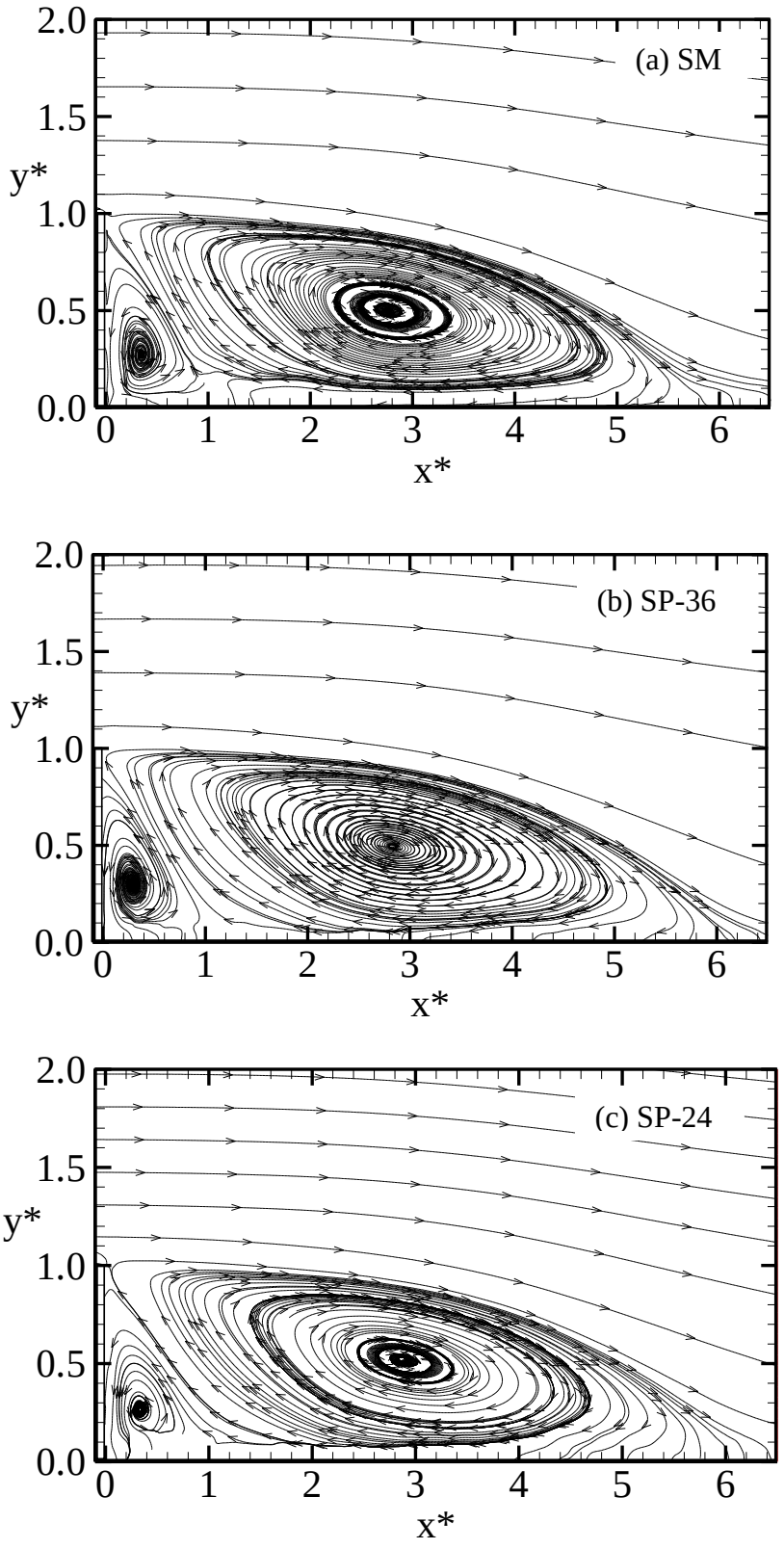

Figure 4.1: Plots of mean streamlines in the recirculation and reattachment regions over smooth wall, SM (a), sandpaper 36 grit, SP-36 (b) and sandpaper 24 grit, SP-24 (c).

independent methods: (i) streamwise location of mean dividing streamline, (ii) 50% forward flow fraction, (iii) zero mean stream function, and (iv) zero mean velocity on the downstream wall. The reattachment length was then determined as the streamwise distance from the trailing edge of the step ($x = 0$) to the reattachment point. As noted in Section 2.1.2, these four methods have been employed to determine the reattachment point in previous experimental and numerical studies on separated and reattached flows (Kasagi and Matsunaga, 1995; Le et al., 1997). For each wall condition, the streamline that emanates from the trailing edge of the step and attaches on to the downstream wall is identified as the mean dividing streamline. To determine the reattachment length using the 50% forward flow fraction method, contours of the forward flow fraction were obtained and these plots over SM, SP-36 and SP-24 are shown in Figure 4.2 (a), (b) and (c), respectively. The streamwise location of the 0.5 contour on the downstream wall is the reattachment point. Contour plots of the stream function over the smooth and rough walls are presented in Figure 4.3 and the reattachment point is determined as the streamwise location on the downstream wall of the zero contour. The streamwise location of the zero mean velocity on the downstream wall is determined from the contour plots of the streamwise mean velocity shown in Figure 4.4.

The reattachment length over the smooth and rough walls obtained using the four independent methods are summarized in Table 4.2. For a given test case, the differences among the values of reattachment length from the four independent methods are within ± 0.1 *h*. This variation is comparable to measurement uncertainty that is estimated to be ± 0.2 *h*. The mean reattachment length obtained from the four techniques over the smooth wall (SM) is 5.8 *h* while the reattachment lengths for the SP-36 and SP-24 are 6.1 *h* and 6.2*h*, respectively. The reattachment length over the

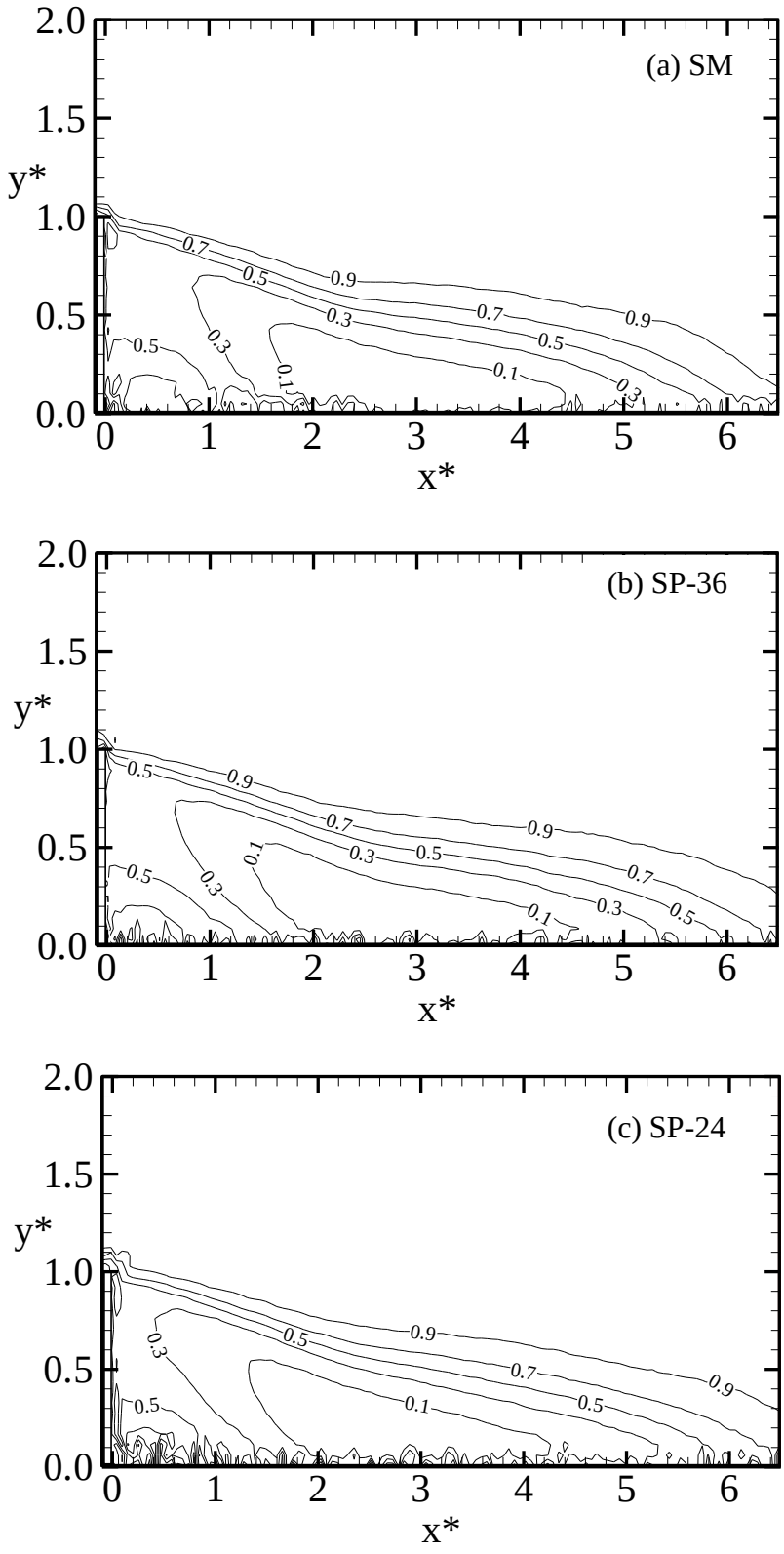

Figure 4.2: Plots of forward flow fraction in the recirculation and reattachment regions over smooth wall, SM (a), sandpaper 36 grit, SP-36 (b) and sandpaper 24 grit, SP-24 (c).

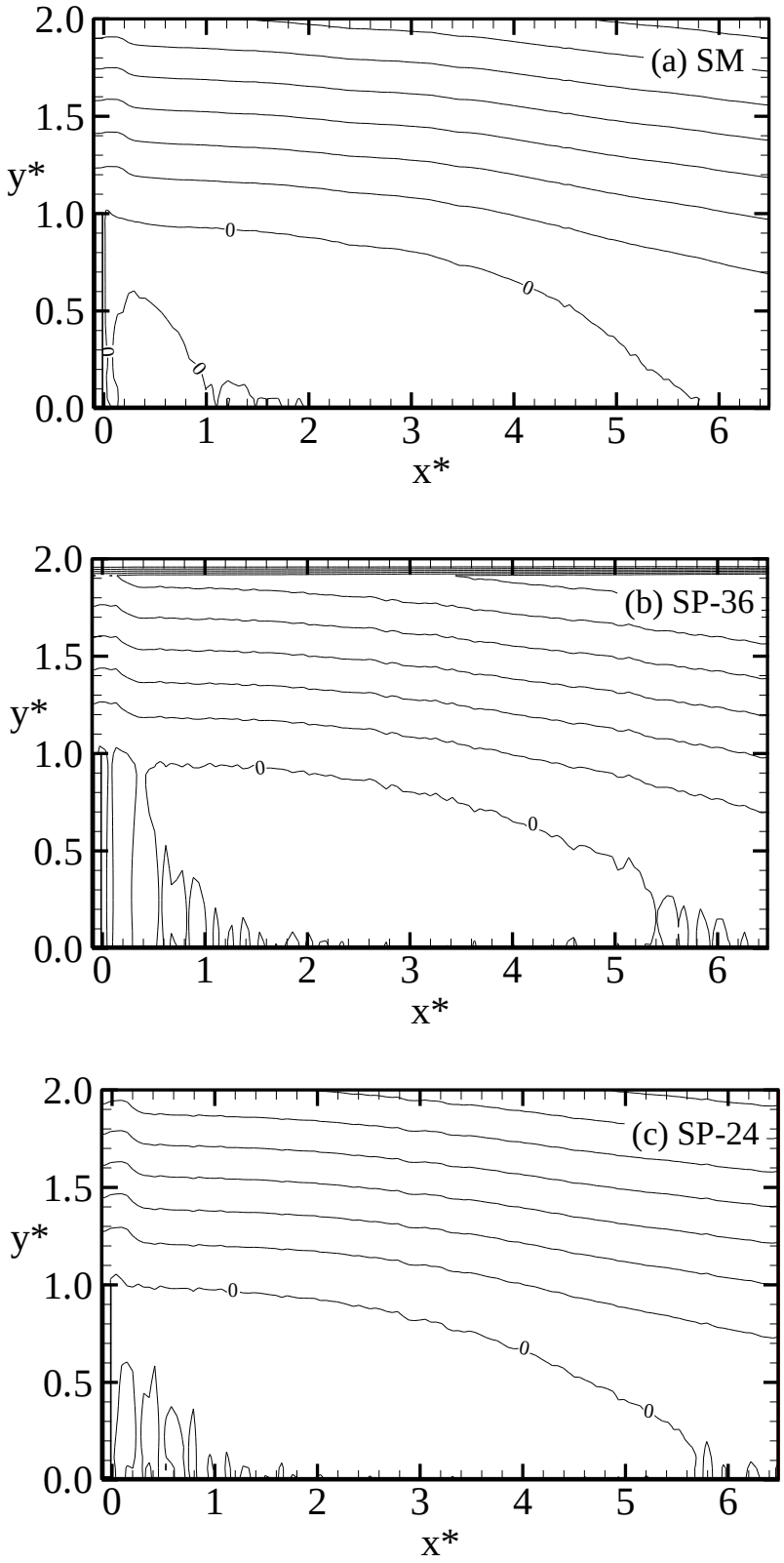

Figure 4.3: Plots of stream function in the recirculation and reattachment regions over smooth wall, SM (a), sandpaper 36 grit, SP-36 (b) and sandpaper 24 grit, SP-24 (c).

Table 4.2: Reattachment length (L_r/h) over smooth wall (SM), sandpaper 36 grit (SP-36) and sandpaper 24 grit (SP-24).

Method	**SM (L_r/h)**	**SP-36 (L_r/h)**	**SP-24 (L_r/h)**
Dividing streamline	5.9	6.2	6.2
50% forward fraction	5.8	6.1	6.2
Zero mean velocity	5.8	6.0	6.2
Zero stream function	5.8	6.2	6.1
Average	5.8	6.1	6.2

smooth and rough walls are within the range of reattachment length (5 h to 7 h) compiled from previous studies by Durst and Tropea, 1981 for expansion ratios ($1.10 < ER < 1.30$).

As explained in Chapter 2, the reattachment length is sensitive to initial conditions such as initial boundary layer state, initial boundary layer thickness, freestream turbulence, pressure gradient, and expansion ratio. The reattachment lengths over the SP-36 and SP-24 are 5% and 7%, respectively, longer than the corresponding value for the smooth wall. Since the initial conditions in the present smooth and rough wall experiments were similar, the differences observed in the reattachment lengths for the smooth and two rough walls are attributed to changes in wall or boundary conditions on the downstream wall. The percentage increases in the reattachment length over the rough walls are comparable to 3.4% increase reported by Kim and Chung, 1995 over transverse square ribs. Ampadu-Mintah et al., 2012, however, did not observe any significant effect of roughness on the reattachment length in their experiments performed in open channel over wire mesh and sandpaper 36 grit.

4.1.2 Mean velocities

Contour plots of the streamwise mean velocities are shown in Figure 4.4. In this figure and subsequent contour plots, the approach centerline mean velocity (U_e) is

used as the velocity scale. For each wall condition, the contour of the streamwise mean velocity shows a separated shear layer emanating from the trailing edge of the step and reattaching on to the downstream wall. As a result of a severe adverse pressure gradient, flow reversal occurs beneath the zero mean velocity contour. The streamwise location of the maximum streamwise backflow velocity coincides with the streamwise location of the center of the primary recirculation bubble. The wall-normal location of the maximum backflow velocity is approximately 0.2 step height away from the wall, irrespective of the wall condition. The maximum streamwise backflow velocity over SM and SP-36 is approximately 18% of the approach centerline mean velocity (U_e), and that over SP-24 is 17% of U_e. These values fall within the range of 20% of U_e reported in previous studies over smooth wall (Eaton and Johnston, 1981; Kasagi and Matsunaga, 1995) and 12% of U_e observed for flow over open channel BFS with smooth and rough downstream walls (Ampadu-Mintah et al., 2012).

The contours of the wall-normal mean velocity over SM, SP-36 and SP-24 are shown in Figure 4.5 (a), (b) and (c), respectively. Irrespective of the wall condition, the contours display positive velocities in the region that spans 3.5 step heights downstream of the trailing edge of the step and one step height away from the wall. Negative velocities are observed in the region above the separated shear layer and in the vicinity of the reattachment point. The relatively high negative values of the wall-normal mean velocity are indication of intense entrainment of higher freestream velocity towards the wall to overcome the momentum deficit caused by the separation. The maximum negative wall-normal mean velocity for all test cases is about 7% of the approach centerline mean velocity and is located at approximately, x^* = 4.6 and y^* = 1.0. The value of the maximum negative wall-normal mean velocity

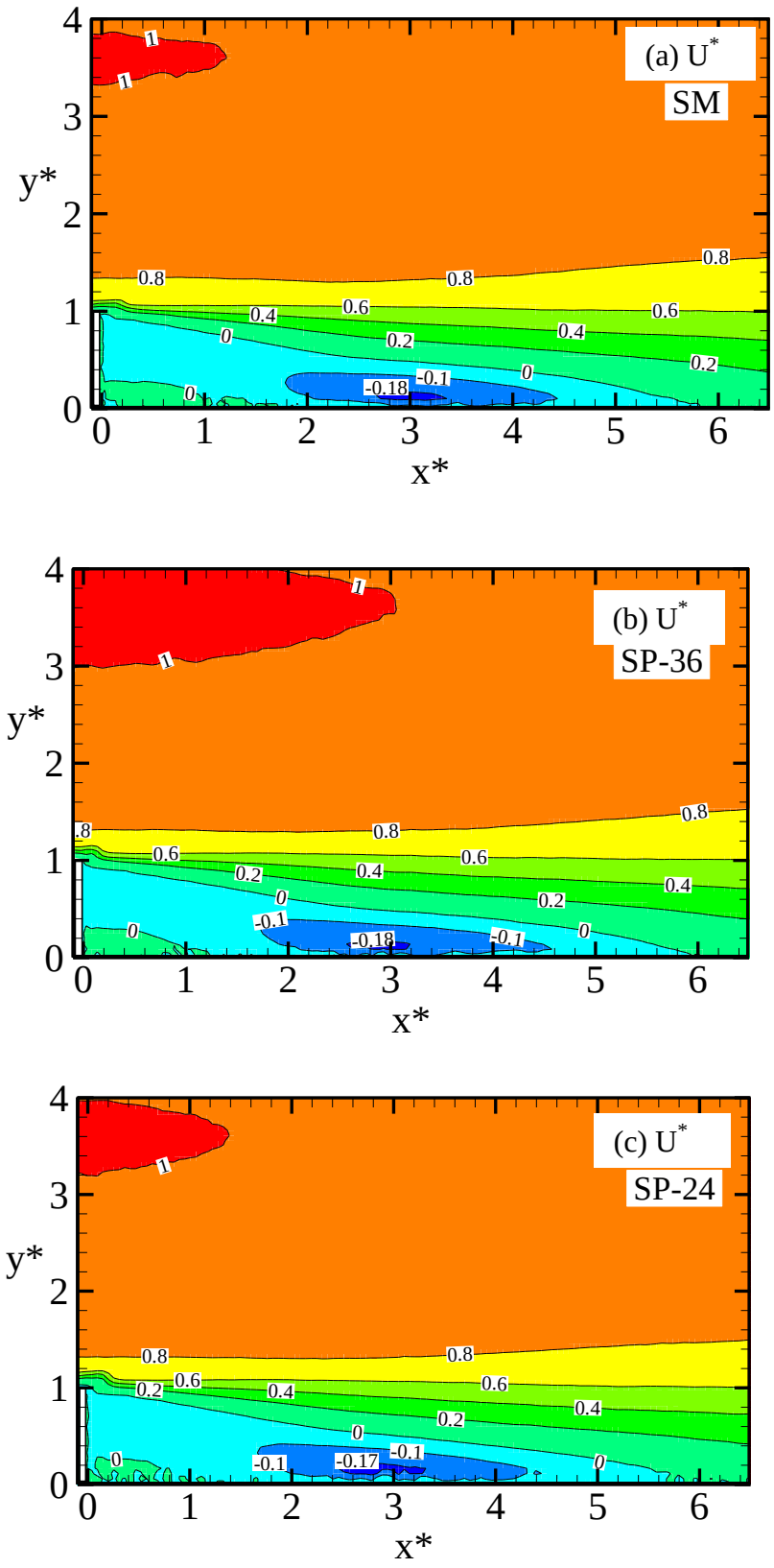

Figure 4.4: Contour plots of dimensionless streamwise mean velocities (U^*) in the recirculation region over smooth wall, SM (a), sandpaper 36 grit, SP-36 (b) and sandpaper 24 grit, SP-24 (c).

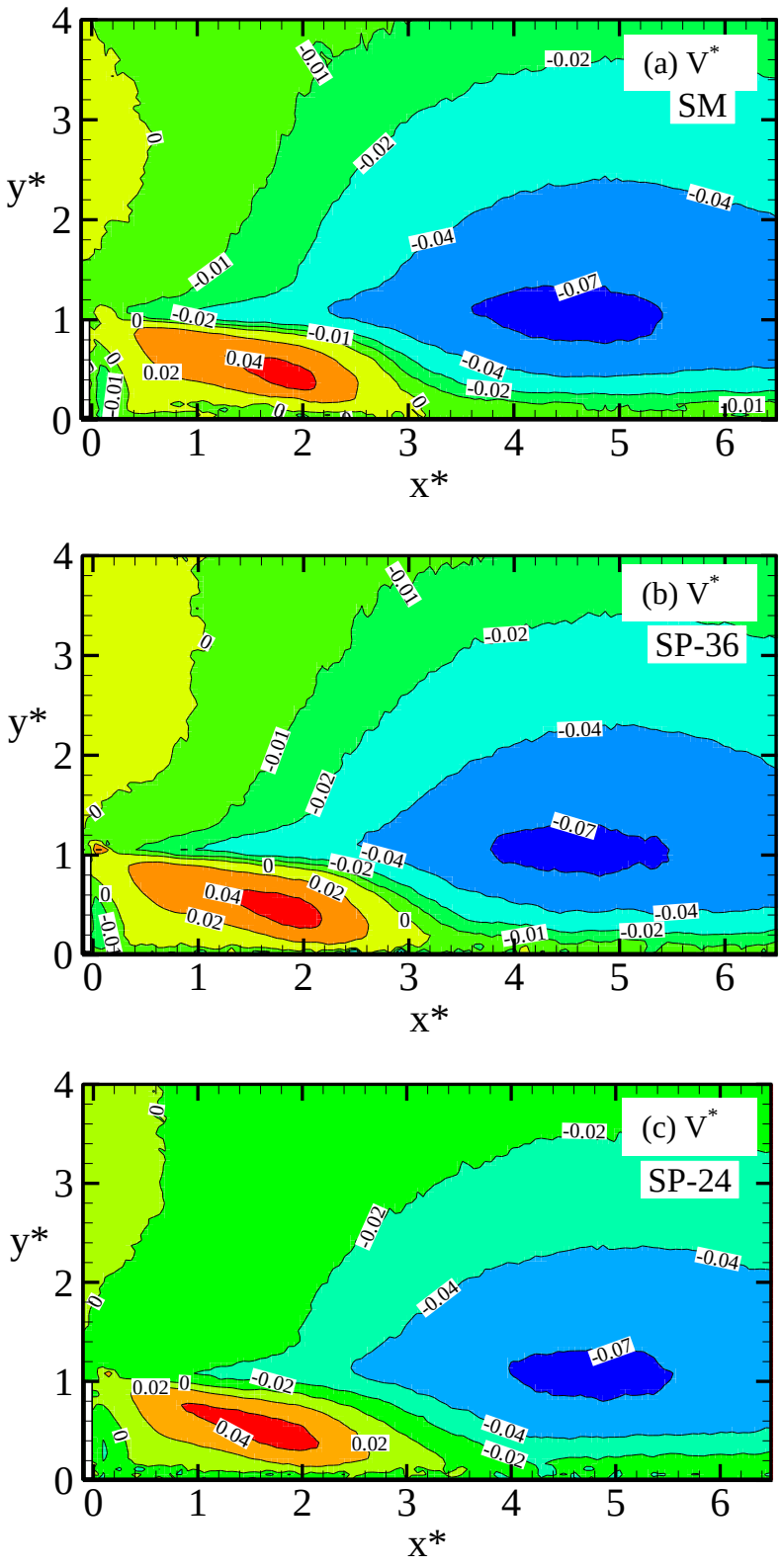

Figure 4.5: Contour plots of dimensionless wall-normal mean velocities (V^*) in the recirculation region over smooth wall, SM (a), sandpaper 36 grit, SP-36 (b) and sandpaper 24 grit, SP-24 (c).

reported in the present study is comparable to 8% of approach centerline mean velocity reported by Kasagi and Matsunaga, 1995 over a smooth wall.

The spatial gradients of the mean velocities: $\partial U/\partial x$, $\partial U/\partial y$, $\partial V/\partial x$ and $\partial V/\partial y$ contribute to the production terms of turbulent kinetic energy and Reynolds stresses transport equations. In canonical shear flows, the dominant velocity gradient is $\partial U/\partial y$ and the other spatial gradients (i.e. $\partial U/\partial x$, $\partial V/\partial x$, $\partial V/\partial y$) are identically zero (for example, in a fully developed channel flow) or negligible in comparison to $\partial U/\partial y$. In view of the significant variation the wall-normal mean velocity with wall-normal distance, as observed in Figure 4.5, it was decided to investigate the individual contributions of the four spatial mean velocity gradients to turbulence production. The contour plots of the four spatial mean velocity gradients over the smooth wall are shown in Figure 4.6 and 4.7. The corresponding plots over the two rough walls are not shown because they are qualitatively similar to those over the smooth wall.

As expected, the variations of the mean velocities in the wall-normal direction are significantly larger than the variations in the streamwise direction (i.e. $\partial U/\partial y > \partial U/\partial x$ and $\partial V/\partial y > \partial V/\partial x$). The values of $\partial U/\partial x$ and $\partial V/\partial x$ are, however, non-negligible and may contribute to the production terms of Reynolds stresses transport equations. The contour of $\partial U/\partial y$ (Figure 4.6 (b)) shows a strong shear between the primary recirculating bubble and the freestream flow in the early region of the separated shear layer. The maximum dimensionless $\partial U/\partial y$ in the early region of the separated shear layer is 2.0 for all wall conditions. Unlike canonical shear flows, the contours of $\partial V/\partial y^*$ reveal that the variation of wall-normal mean velocity with wall-normal distance is non-negligible in the recirculation region. For example, in the early region of the separated shear layer, a maximum negative gradient of - 0.22 is observed over

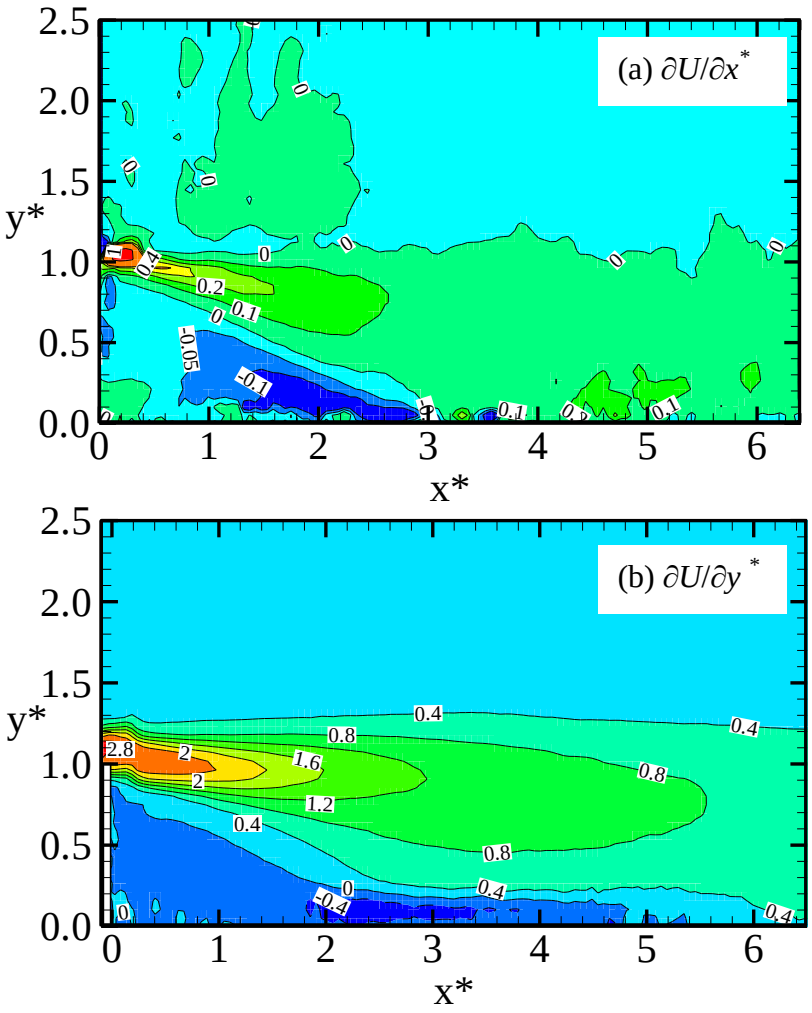

Figure 4.6: Contour plots of dimensionless $\partial U/\partial x$ (a) and $\partial U/\partial y$ (b) in the recirculation region over smooth wall (SM).

the smooth wall and - 0.20 over the rough walls. This implies that $\partial V/\partial y$ will also contribute significantly to the wall-normal transport of momentum and also the production terms in the transport equations for the turbulent kinetic energy and wall-normal Reynolds normal stress.

4.1.3 Reynolds stresses and turbulent kinetic energy

Contour plots of the streamwise and wall-normal Reynolds normal stresses over the smooth wall are compared with the corresponding plots over the rough walls in Figure 4.8 and 4.9, respectively. For each wall condition, the contours of the streamwise

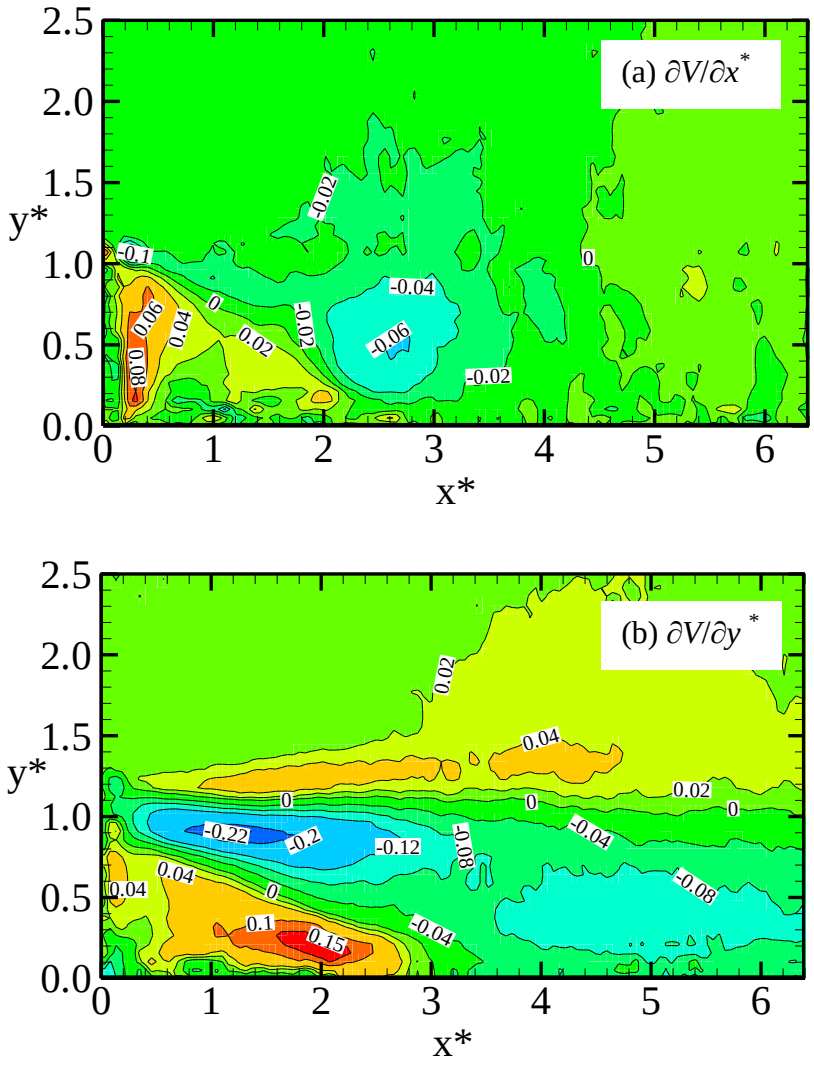

Figure 4.7: Contour plots of dimensionless $\partial V/\partial x$ (a) and $\partial V/\partial y$ (b) in the recirculation region over smooth wall (SM).

Reynolds normal stress (Figure 4.8) reveal maximum turbulence levels in the region of strong shear layer and later stage of the separated shear layer. In the case of the wall-normal Reynolds normal stress (Figure 4.8), the maximum turbulence levels are located further downstream of the separated shear layer. The turbulence levels observed in these plots are significantly higher than the peak values observed in the upstream region. For example, typical peak values of streamwise and wall-normal Reynolds normal stresses are 0.02 and 0.009, respectively. These values are 18% and 84% higher than the corresponding upstream values. It should be recalled that the

separated shear layer is associated with energetic large scale structures, therefore, the high turbulence levels observed in Figure 4.8 and 4.9 are indications of the presence of these energetic structures.

The contour plots of turbulent kinetic energy and Reynolds shear stress over the smooth and rough walls are shown in Figure 4.10 and 4.11, respectively. Since the spanwise Reynolds normal stress, w^2 was not measured in the present study, the turbulent kinetic energy was approximated as $k = 0.75\ (u^2 + v^2)$. The contours of turbulent kinetic energy over the smooth and rough walls are qualitatively similar to the respective contours of the streamwise Reynolds normal stress. This should be expected because the streamwise Reynolds normal stress contributes more significantly to turbulent kinetic energy than the wall-normal Reynolds normal stress. Similar to the distribution of the wall-normal Reynolds normal stress, the maximum Reynolds shear stress over all wall conditions is located at the later stage of the separated shear layer. The shape and distribution of the contours of Reynolds stresses and turbulent kinetic energy in the present study compare well with results presented by Kostas et al., 2002 and Le et al., 1997 over smooth walls.

The maximum values of the Reynolds stresses and turbulent kinetic energy over the smooth and rough walls and the results reported by Kostas et al., 2002 over a smooth wall are compared in Table 4.3. The table demonstrates that the maximum value of the streamwise and wall-normal Reynolds normal stresses and Reynolds shear stress over the smooth wall (SM) is about 5%, 44% and 25% lower than corresponding values reported by Kostas et al., 2002. The disparity between the maximum values of the present study and that of Kostas et al., 2002 is not all surprising because the flow characteristics in the recirculation region significantly depend on a combination of

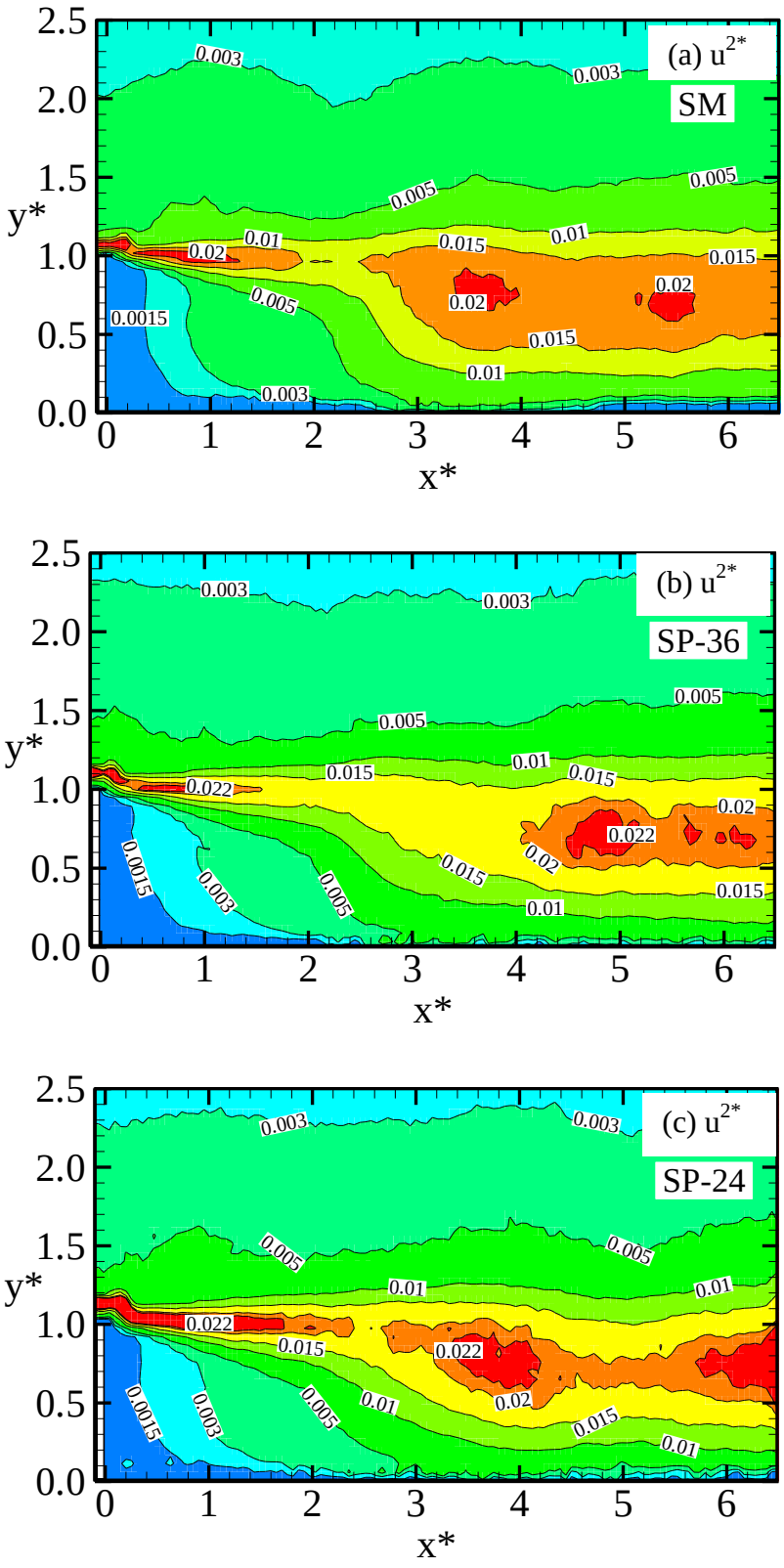

Figure 4.8: Contour plots of dimensionless streamwise Reynolds normal stress (u^{2*}) in the recirculation region over smooth wall, SM (a), sandpaper 36 grit, SP-36 (b) and sandpaper 24 grit, SP-24 (c).

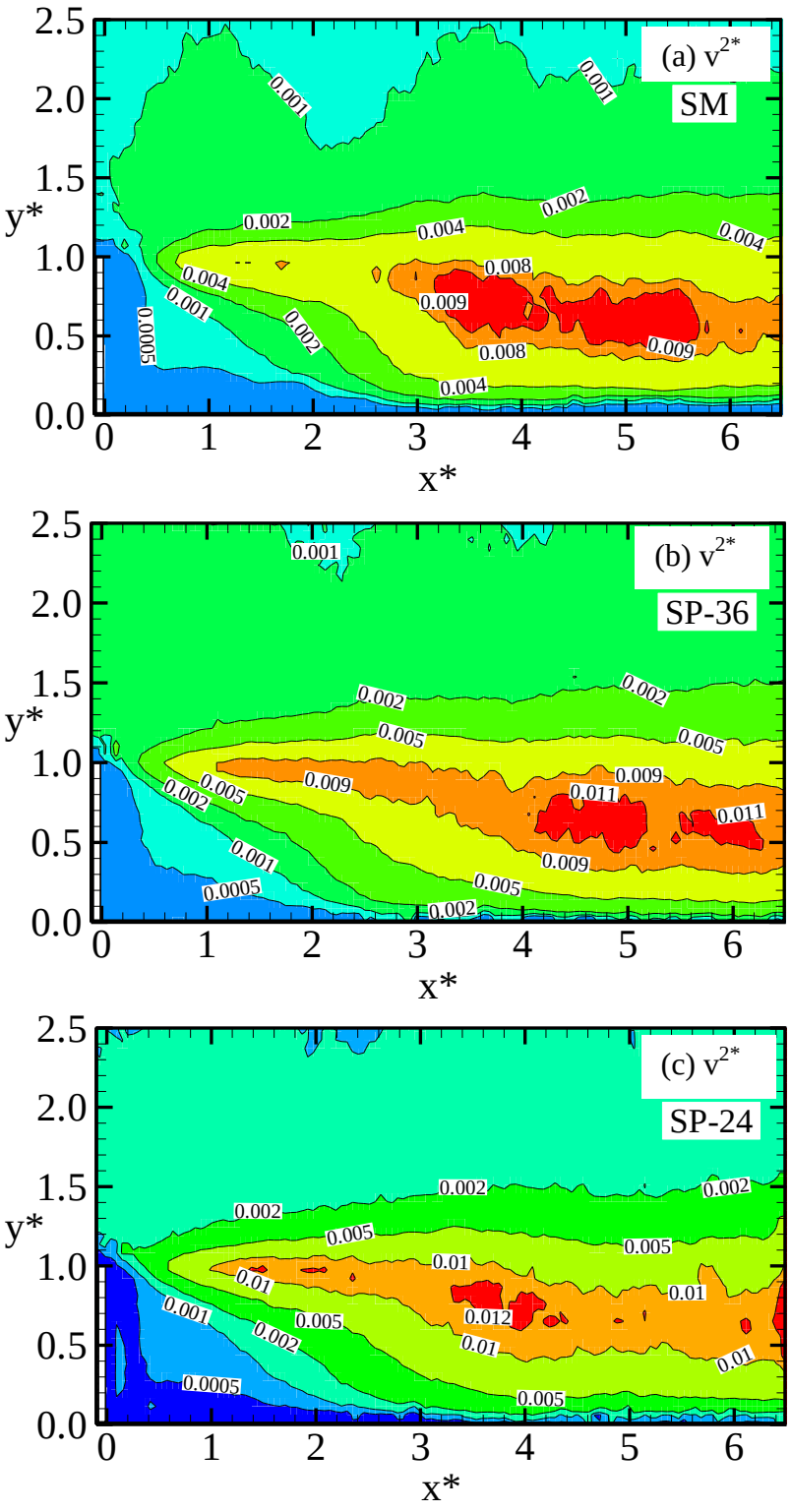

Figure 4.9: Contour plots of dimensionless wall-normal Reynolds normal stress (v^{2*}) in the recirculation region over smooth wall, SM (a), sandpaper 36 grit, SP-36 (b) and sandpaper 24 grit, SP-24 (c).

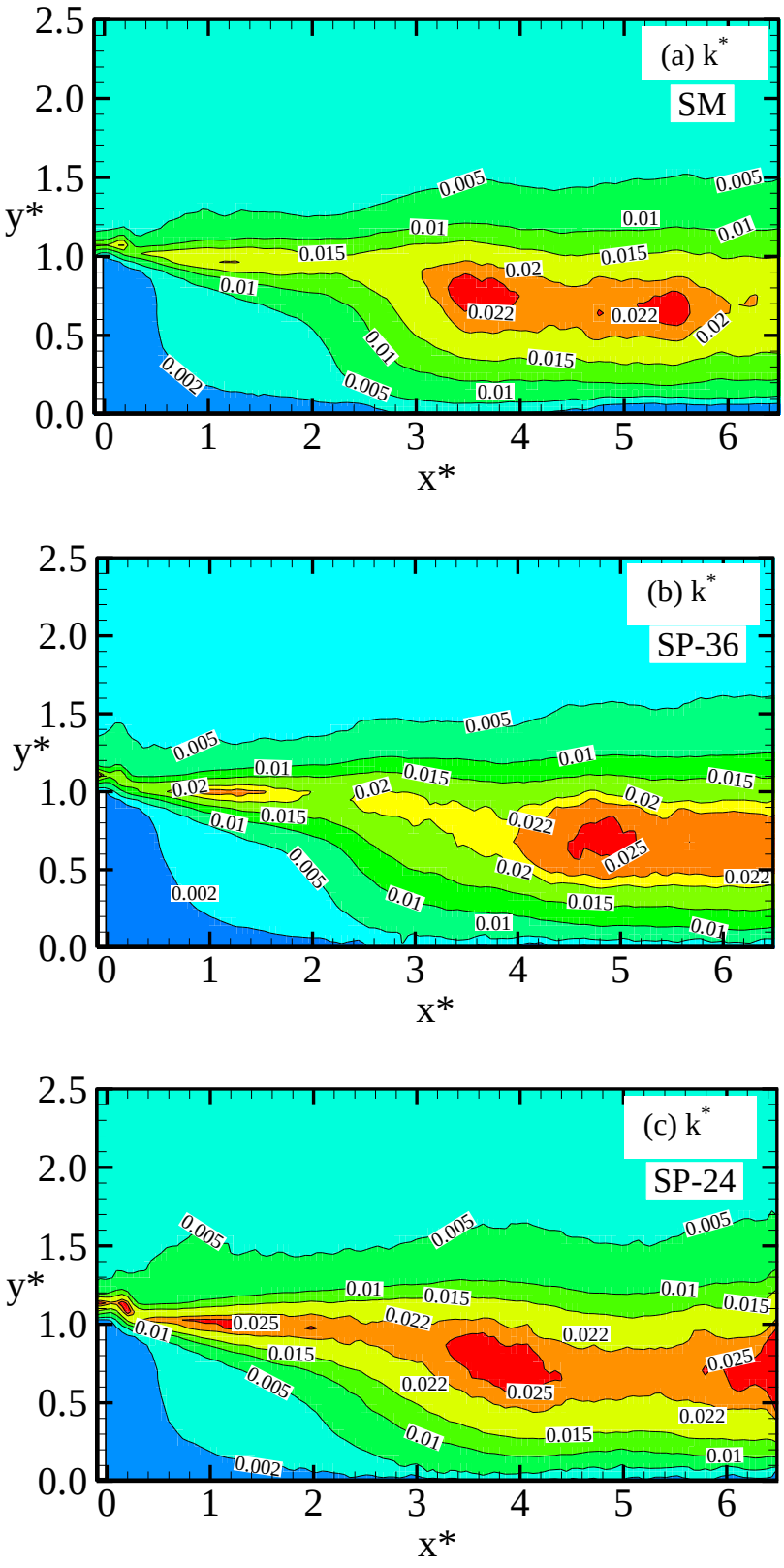

Figure 4.10: Contour plots of dimensionless turbulent kinetic energy (k^*) in the recirculation region over smooth wall, SM (a), sandpaper 36 grit, SP-36 (b) and sandpaper 24 grit, SP-24 (c).

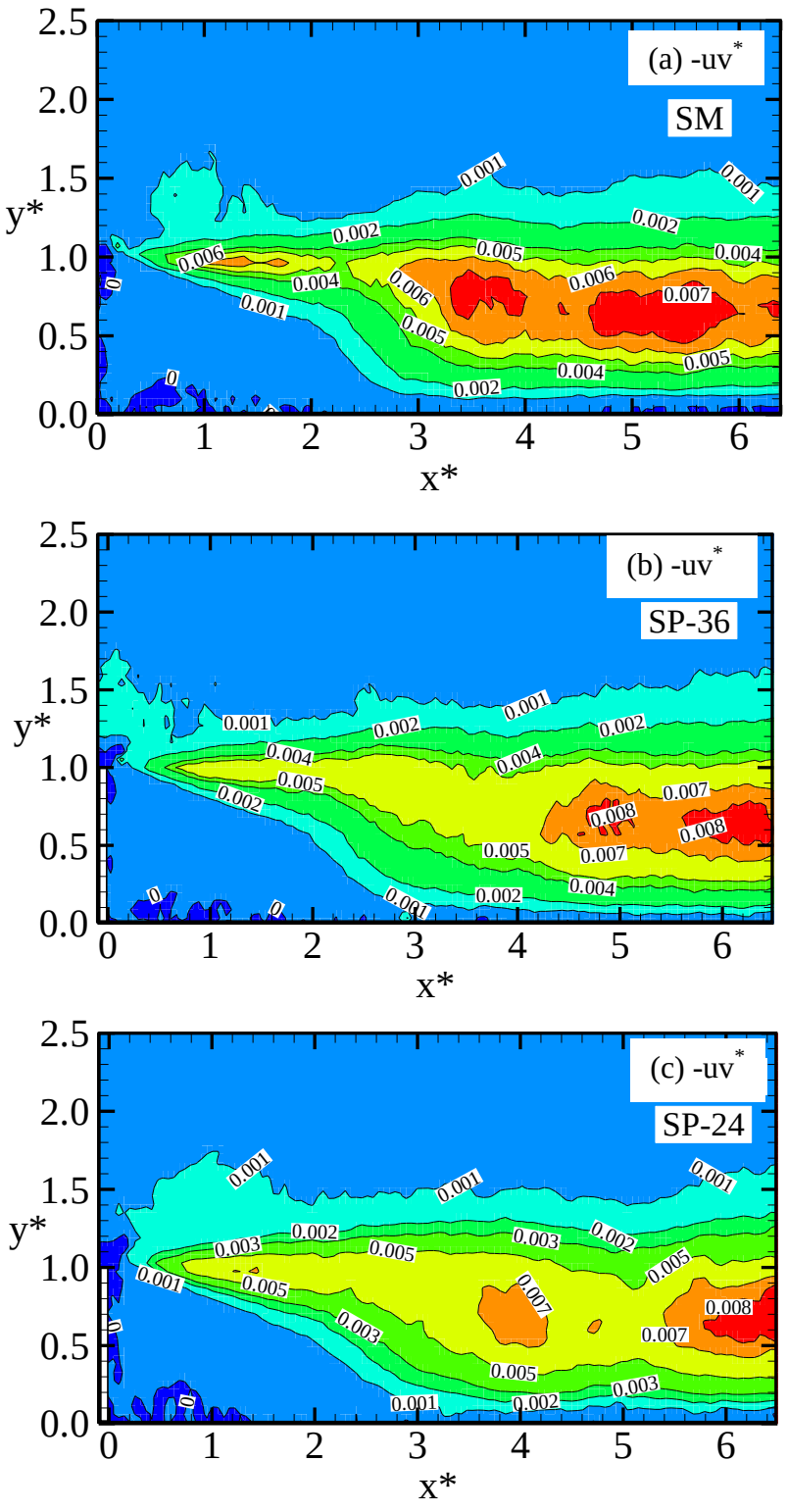

Figure 4.11: Contour plots of dimensionless Reynolds shear stress ($-uv^*$) in the recirculation region over smooth wall, SM (a), sandpaper 36 grit, SP-36 (b) and sandpaper 24 grit, SP-24 (c).

Table 4.3: Maximum values of Reynolds stresses, turbulent kinetic energy and turbulent production in the recirculation region over smooth wall (SM), sandpaper 36 grit (SP-36) and sandpaper 24 grit (SP-24).

	u^{2*}_{max}	v^{2*}_{max}	$-uv^{*}_{max}$	k^{*}_{max}	$P_{-uv}{}^{*}_{max}$	$P_k{}^{*}_{max}$
SM	0.020	0.009	0.007	0.022	0.012	0.011
SP-36	0.022	0.011	0.008	0.025	0.012	0.011
SP-24	0.022	0.012	0.008	0.025	0.013	0.012
Kostas et al., 2002	0.021	0.013	0.009	-	-	0.012

geometry and initial flow conditions such as the expansion ratio and freestream turbulence level. In wall-bounded turbulent shear flows, roughness enhances the levels of Reynolds stresses and turbulent kinetic energy. As can be observed from Table 4.3, the maximum values of the Reynolds stresses and turbulent kinetic energy are higher over the rough walls in comparison to the smooth wall. For example, the streamwise Reynolds normal stress, wall-normal Reynolds normal stress, Reynolds shear stress and turbulent kinetic energy over SP-24 is 10%, 33%, 14% and 14%, respectively, larger than the corresponding maximum values over the reference smooth wall.

4.1.4 Turbulent production

The production term of the turbulent kinetic energy transport equation is given by $P_k = -(u^2\,\partial U/\partial x + v^2\,\partial V/\partial y + uv\,(\partial U/\partial y + \partial V/\partial x))$. The production term can be subdivided into contributions by the normal stresses, $P_n = -(u^2\,\partial U/\partial x + v^2\,\partial V/\partial y)$ and contribution by the shear stresses, $P_s = -uv\,(\partial U/\partial y + \partial V/\partial x)$. The production terms in the transport equations for the streamwise and wall-normal Reynolds normal stresses are, respectively, given by $P_{uu} = -(u^2\,\partial U/\partial x + uv\,\partial U/\partial y)$ and $P_{vv} = -(v^2\,\partial V/\partial y + uv\,\partial V/\partial x)$. In canonical turbulent shear flows such as zero pressure gradient turbulent boundary layers and fully developed channel turbulent flows, $\partial U/\partial y$ is the dominant

velocity gradient (as explained earlier in Section 4.1.2) so $-uv\ \partial U/\partial y$ accounts for virtually the entire production of the turbulent kinetic energy and streamwise Reynolds normal stress. The production term in the wall-normal Reynolds normal stress transport equation is zero or negligibly small since $\partial V/\partial y$ and $\partial V/\partial x$ are negligible or identically zero. In this case, energy is redistributed from the streamwise Reynolds normal stress to the wall-normal Reynolds normal stress. This redistribution of energy is accomplished by the pressure redistribution terms in the Reynolds stress transport equations. It should be noted that, for incompressible turbulent flows, the pressure redistribution term vanishes when the Reynolds stress transport equations are contracted to obtain the turbulent kinetic transport equation by virtue of continuity equation.

Contour plots of P_n, P_s and $-uv\ \partial U/\partial y$ over the smooth wall are shown in Figure 4.12 to investigate the contributions of the normal stresses and shear stress to the total turbulence production. As can be observed in Figure 4.12 (a), the negative values suggest that normal stresses reduce the level of turbulence production in the separated shear layer. Although, the maximum value of P_s is 8% higher than that of $-uv\ \partial U/\partial y$, the shape and the distribution of the contours are remarkably similar. This is an indication that $-uv\ \partial U/\partial y$ is the major contributor to turbulence production in the recirculation region. The contributions of the individual terms of P_n and P_s will be examined in detail in Section 4.1.9.

Contour plots of the total production term, P_k over the smooth and rough walls are shown in Figure 4.13 to examine the effects of roughness on turbulence production in the recirculation region. Figure 4.13 demonstrates that, for each test case, the maximum P_k occur in the region of strong shear layer centered at about a step height

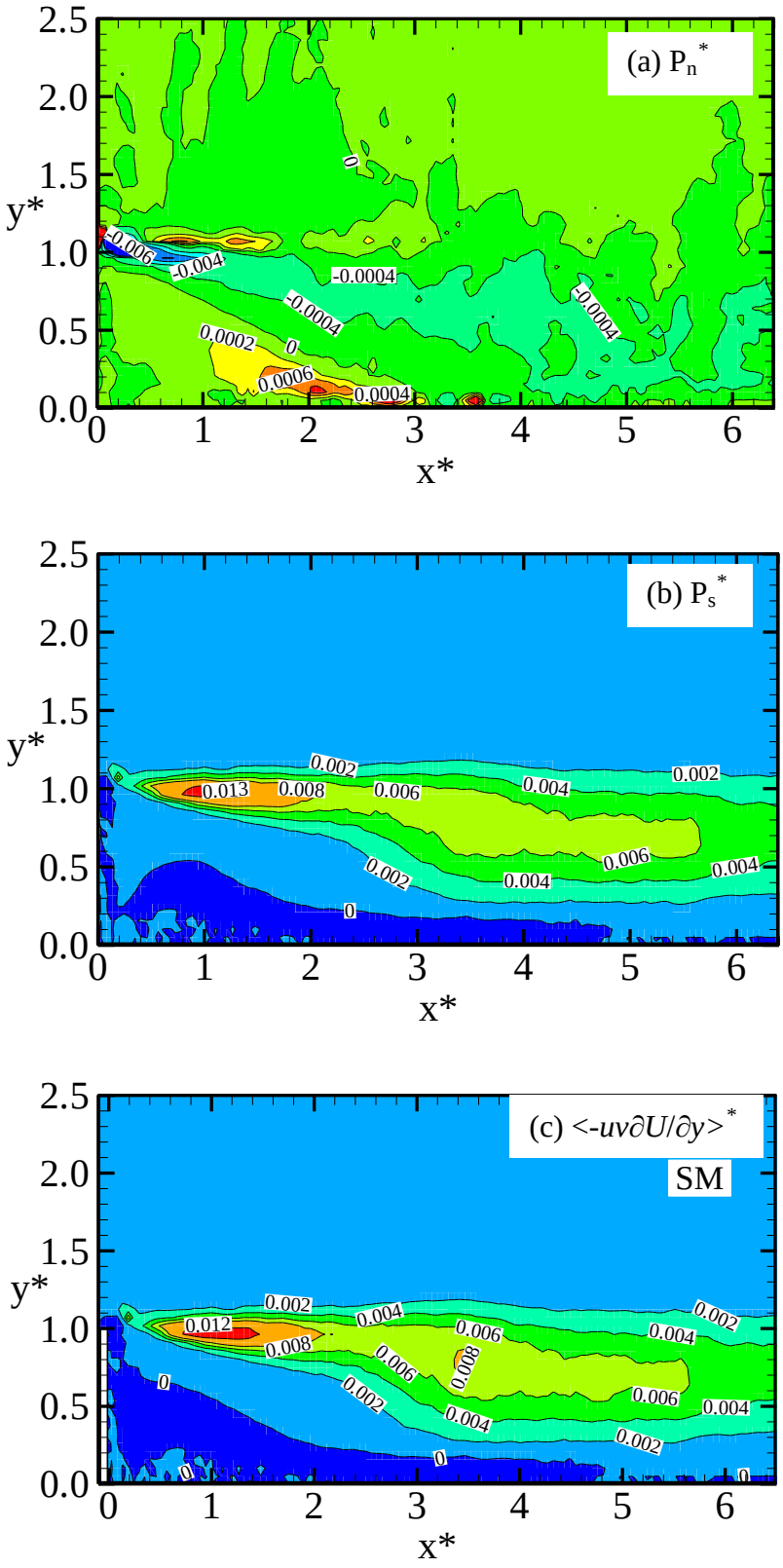

Figure 4.12: Contour plots of dimensionless P_n^* (a), P_s^* (b) and $<-uv\partial U/\partial y>^*$ (c) production terms in the recirculation region over smooth wall (SM). Note that $P_n = -(u^2\,\partial U/\partial x + v^2\,\partial V/\partial y)$ and $P_s = -uv\,(u^2\,\partial U/\partial y + v^2\,\partial V/\partial x)$.

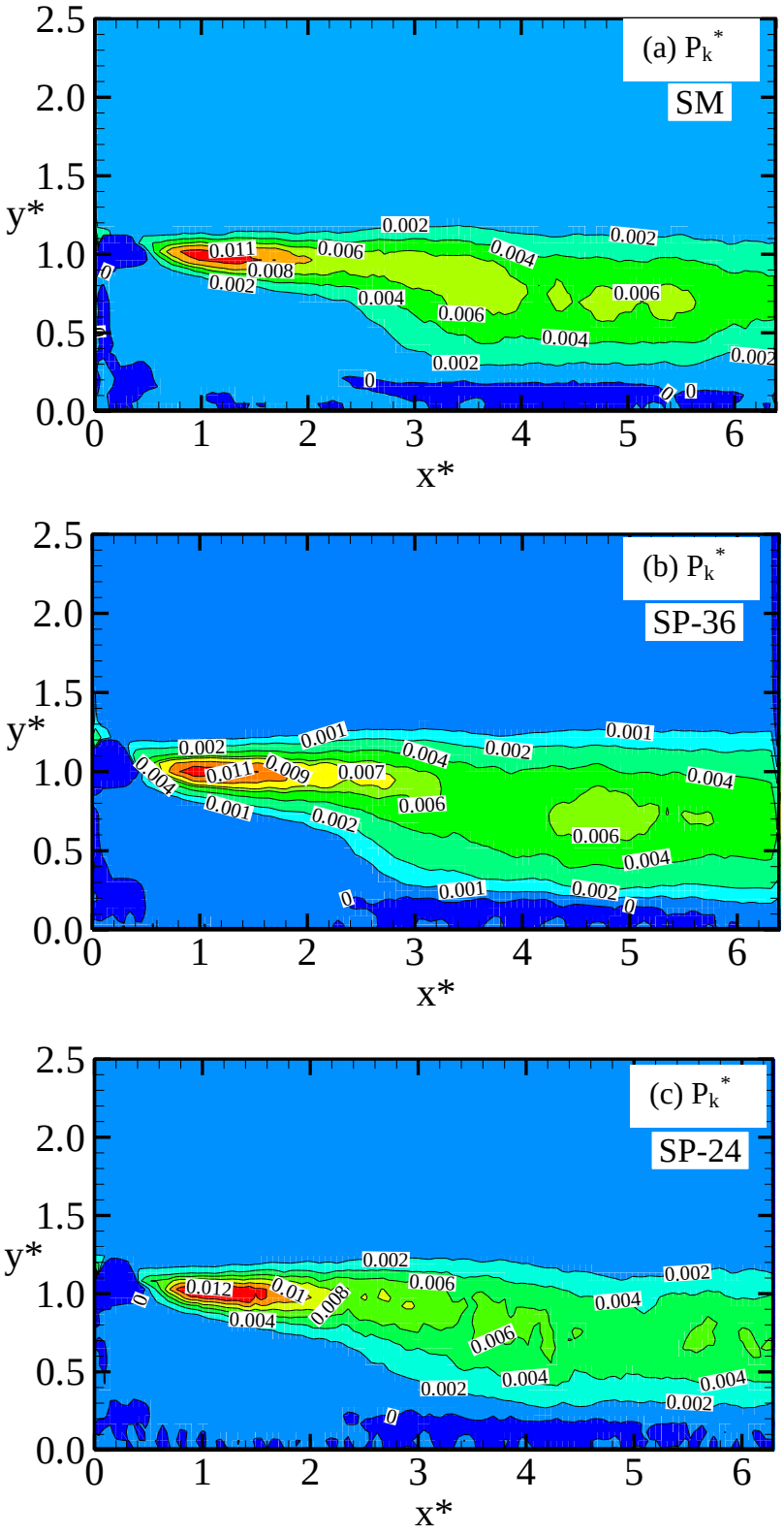

Figure 4.13: Contour plots of dimensionless production term of turbulent kinetic energy transport equation, P_k^* in the recirculation region over smooth wall, SM (a), sandpaper 36 grit, SP-36 (b) and sandpaper 24 grit, SP-24 (c). Note that $P_k = -(u^2 \partial U/\partial x + v^2 \partial V/\partial y + uv(\partial U/\partial y + \partial V/\partial x)$.

from the trailing edge of the step and one step height away from the wall. The location of the maximum turbulence production does not coincide with the location of maximum Reynolds shear stress and wall-normal Reynolds normal stress. The enhanced turbulence production in the region of strong shear layer in the recirculation region is in agreement with results reported in previous studies over smooth wall (Kasagi and Matsunaga, 1995; Kostas et al., 2002). The effect of roughness is to enhance the level of turbulence production in the recirculation region. Table 4.3 demonstrates that the maximum production over SP-24 is 9% larger than the corresponding values over SP-36 and SM. The higher level of turbulence production observed over the rough walls is consistent with the higher Reynolds stresses observed over the rough walls in comparison to the smooth wall.

4.2 Profiles of turbulent statistics in recirculation and redevelopment regions

The effect of roughness on the distributions of the turbulent statistics at selected streamwise locations in the recirculation and redevelopment region over SM, SP-36 and SP-24 is examined in this section. In the recirculation region, profiles of the turbulent statistics were obtained at selected streamwise locations; $x^* = S_c$, 0.25 L_r, P_c, 0.75 L_r and L_r (where S_c and P_c are the streamwise locations of the centers of secondary and primary recirculating bubble, respectively, and L_r is the reattachment length) over the smooth and rough walls. An illustration of the profile locations in the recirculation region over the smooth wall, for example, is shown in Figure 4.14. In the redevelopment region, the profiles were obtained at similar dimensionless streamwise distances beyond the reattachment point of each test case, i.e. $x' = (x - L_r)/h$. This scaling is used instead of the conventional scale, $x^* = x/h$, to minimize possible effect of differences in reattachment length on the comparison between the turbulent statistics over the smooth and rough walls. For each wall condition, profiles were

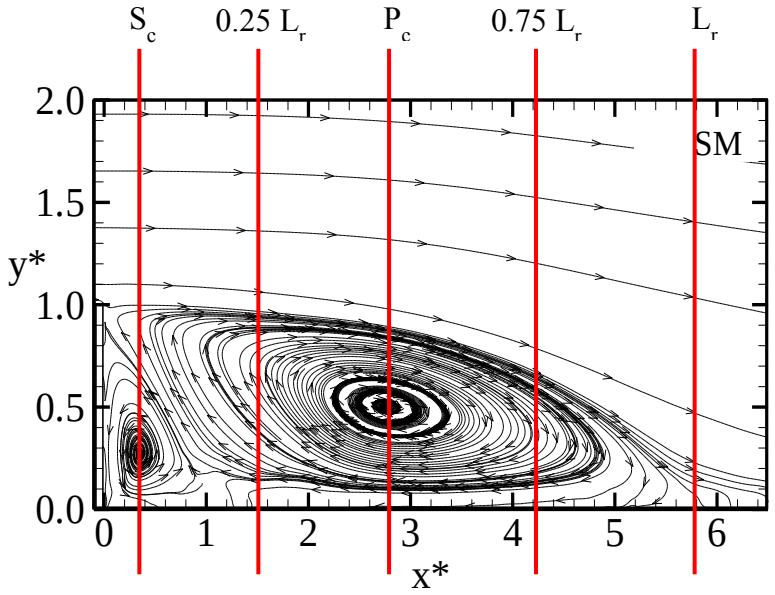

Figure 4.14: Schematic of profile locations in the recirculation region over smooth wall (SM).

obtained at streamwise locations in the redevelopment region (x' = 1, 5, 15, 30 and 45). The specific dimensionless streamwise locations (x^*) of the profiles in the recirculation and redevelopment regions over each wall condition are summarized in Table 4.4 and 4.5, respectively. For each profile, the local maximum mean velocity, U_{max} is used as the velocity scale. This scaling is more appropriate to quantify the differences between turbulent statistics over the smooth and rough walls at the selected streamwise locations downstream of the BFS.

Table 4.4: Dimensionless streamwise locations in the recirculation region over smooth wall (SM), sandpaper 36 grit (SP-36) and sandpaper 24 grit (SP-24).

x^*	SM (x/h)	SP-36 (x/h)	SP-24 (x/h)
S_c	0.3	0.3	0.3
0.25 L_r	1.5	1.5	1.6
P_c	2.8	2.8	2.9
0.75 L_r	4.4	4.6	4.7
L_r	5.8	6.1	6.2

Table 4.5: Dimensionless streamwise locations in the redevelopment region over smooth wall (SM), sandpaper 36 grit (SP-36) and sandpaper 24 grit (SP-24).

x'	SM (x/h)	SP-36 (x/h)	SP-24 (x/h)
1	6.8	7.1	7.2
5	10.8	11.1	11.2
15	20.8	21.1	21.2
30	35.8	36.1	36.2
45	50.8	51.1	51.2

The distributions of the local maximum mean velocity over the smooth and rough walls at the selected streamwise locations are shown in Figure 4.15 (a). Irrespective of the wall condition, the local maximum mean velocity decays rapidly from the value of the approach centerline mean velocity (U_e) to about 0.9 U_e at approximately 10 step heights from the trailing edge of the step. Beyond 10 step heights, the distribution of the local maximum mean velocity is approximately constant for each wall condition. The rapid decay of the local maximum mean velocity in the region $x^* < 10$ is attributed to the sudden expansion which induced a strong APG in the recirculation and early redevelopment regions. The distribution and wall-normal locations of the local maximum mean velocity are nearly independent of wall roughness.

4.2.1 Mean velocities

The profiles of the streamwise mean velocity in the recirculation and redevelopment regions over the smooth wall (SM) and rough walls (SP-36 and SP-24) are shown in Figure 4.16. For each wall condition, the effects of APG caused by sudden expansion at the trailing edge of the step dramatically altered the profiles by decreasing the mean velocity in the region adjacent to the wall ($y^* < 1$). As the flow evolves, the effect of APG reduces and the streamwise mean velocity profiles gradually regain velocity variation from the no-slip condition ($U^* = 0$) at the wall to the maximum local mean velocity further way from wall. In the recirculation region and early redevelopment

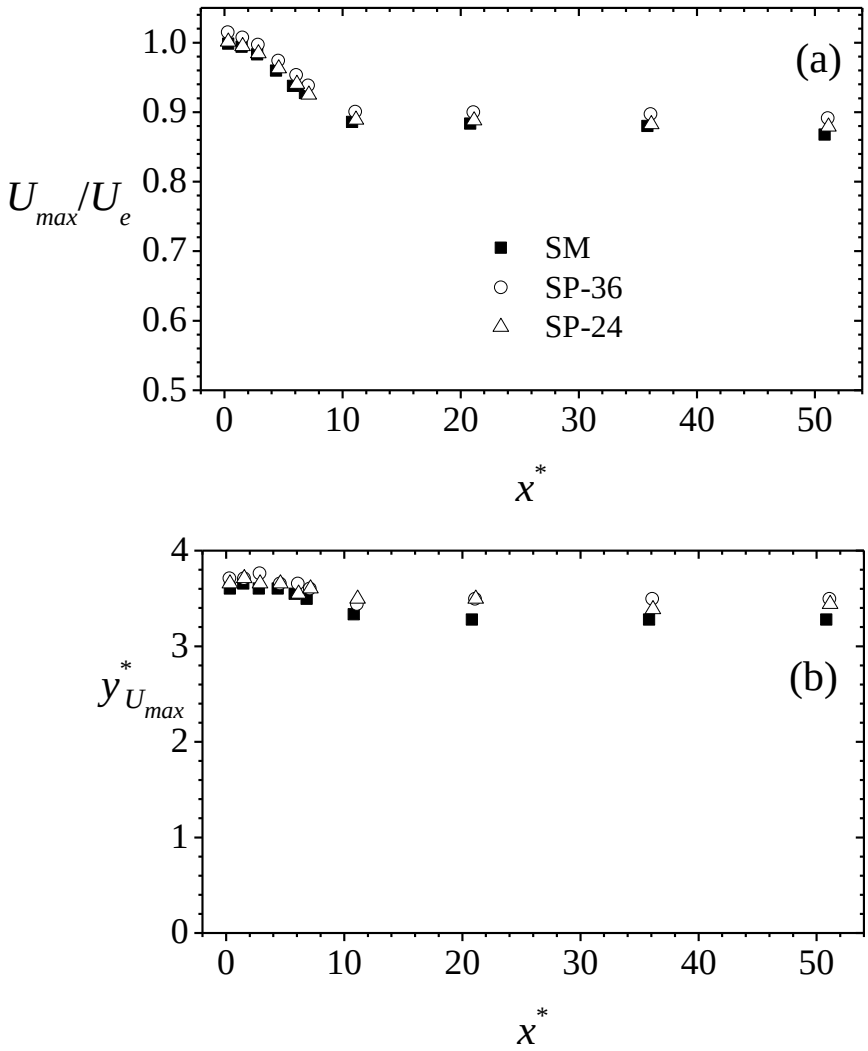

Figure 4.15: Distribution of dimensionless local maximum mean velocity, U_{max} (a) and wall-normal locations of local maximum streamwise mean velocity, y_{Umax} (b) in the recirculation region over smooth wall (SM), sandpaper 36 grit (SP-36) and sandpaper 24 grit (SP-24).

region ($x' = 1$) no significant effect of roughness are observed. Further downstream of the redevelopment region (i.e., $x' \geq 5$), roughness significantly reduced the streamwise mean velocity in the region adjacent to the rough walls. At the furthest measurement location ($x' = 45$), for example, the streamwise mean velocity over SP-36 and SP-24 at 0.2 step height from the wall was reduced by 30% compared with the corresponding value over the smooth wall. The similarity of the profiles over the smooth and rough walls in the recirculation and early redevelopment regions indicate

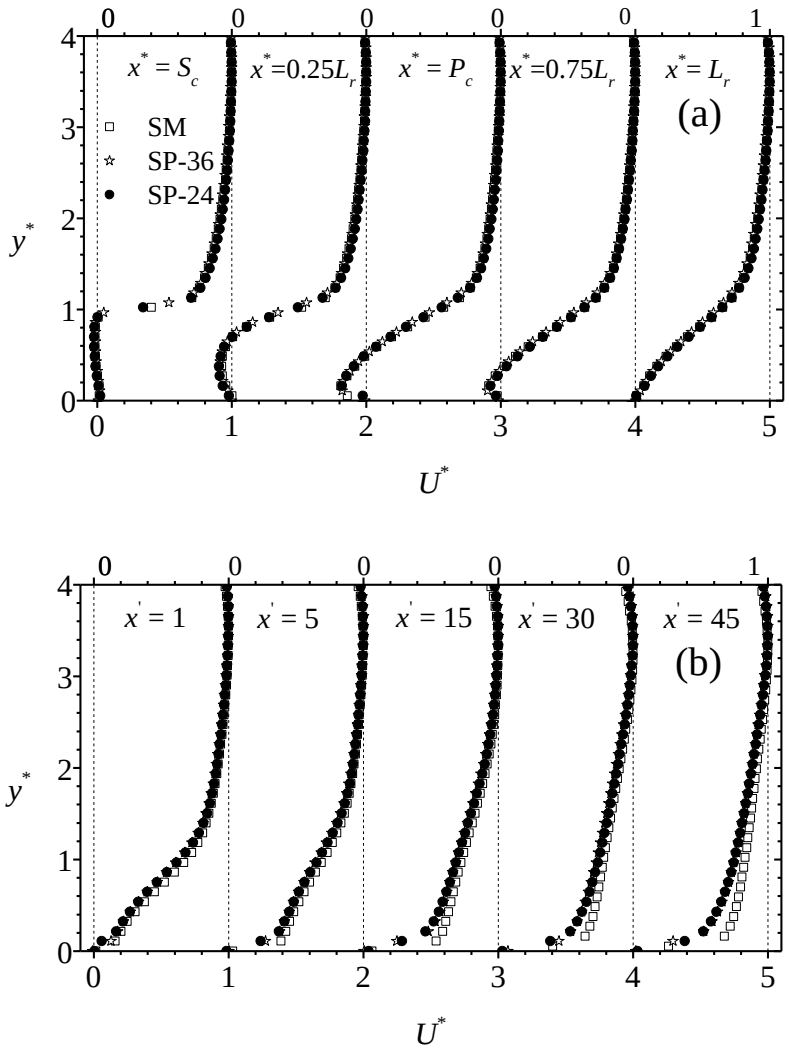

Figure 4.16: Profiles of dimensionless streamwise mean velocity (U^*) in the recirculation region (a) and redevelopment region (b) over smooth wall (SM), sandpaper 36 grit (SP-36) and sandpaper 24 grit (SP-24).

that the effect of severe APG prevail over wall roughness in these regions. A similar observation was made in the recent PIV measurements over wire mesh and sandpaper 36 grit rough walls in open channel by Ampadu-Mintah et al., 2012. Kim and Chung, 1995, on the other hand, observed that wall roughness reduced the streamwise mean velocity in the recirculation region but in the early redevelopment region, streamwise mean velocity distribution was independent of roughness. The reduction of the streamwise mean velocity profiles adjacent to the rough walls in the region $x' \geq 5$ is attributed to enhanced drag produced from the rough walls. Similar observation has

been reported in previous rough-wall turbulent boundary layer studies (Krogstad et al., 1999). The results presented in Figure 4.16 suggest that the effect of wall roughness outweighs that of APG after 5 step height from reattachment.

The distribution of the wall-normal mean velocity in the recirculation and redevelopment regions over the smooth and rough walls are shown in Figure 4.17. The profiles in the recirculation and early redevelopment regions are predominantly negative, and this is an indication of a strong interaction between the freestream flow

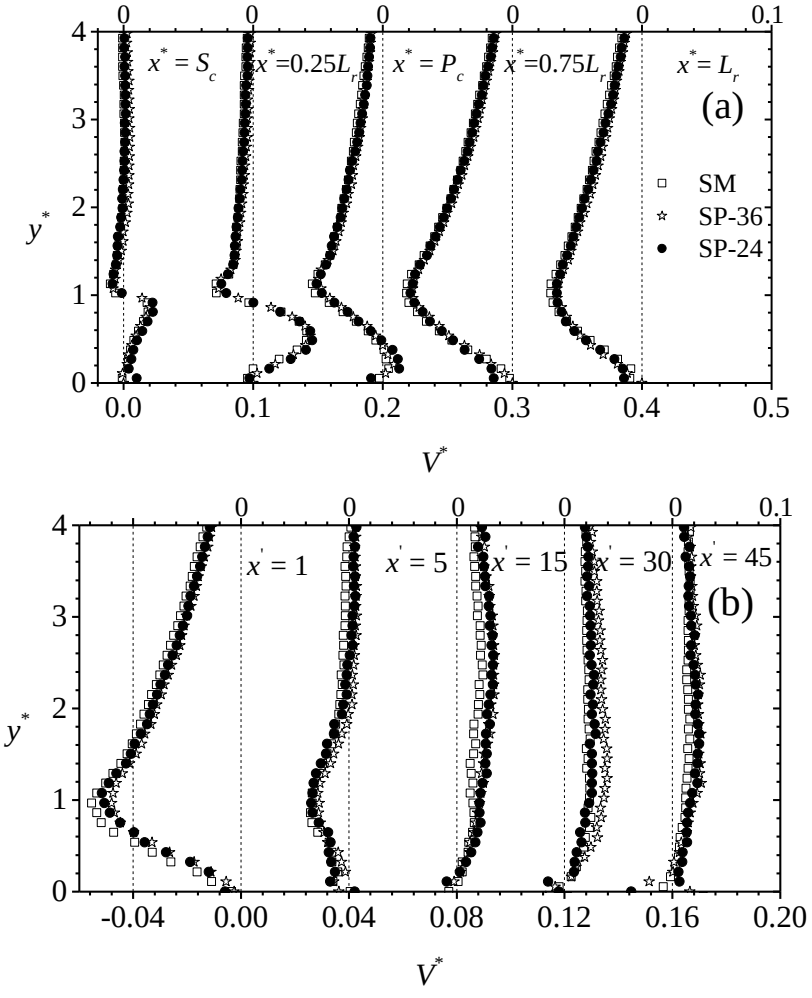

Figure 4.17: Profiles of dimensionless wall-normal mean velocity (V^*) in the recirculation region (a) and redevelopment region (b) over smooth wall (SM), sandpaper 36 grit (SP-36) and sandpaper 24 grit (SP-24).

and the recirculation bubble as well as the reattachment region. Such interactions may facilitate the transport of momentum from the outer region into the momentum-depleted region adjacent to the wall. It should be noted that the effect of APG is the major cause of momentum-deficit in the near wall region of the recirculation and early redevelopment regions. Further downstream within the redevelopment region, the profiles of the wall-normal mean velocity changed sign (i.e. become positive) but the velocities are relatively smaller than the predominant negative velocities observed in the recirculation region and early redevelopment region.

The effect of roughness on the wall-normal mean velocity is not significant in the recirculation and early redevelopment regions. Further downstream of the reattachment point, roughness enhanced the levels of the wall normal mean velocity and the impact is more significant at the measurement locations 15 and 30 step heights from reattachment. At $x' = 15$, for example, the wall-normal mean velocity over SP-36 and SP-24 at one step height from the wall is 65% and 15% larger than the corresponding velocity over the smooth wall (SM).

4.2.2 Reynolds stresses and turbulent kinetic energy

The distributions of the streamwise and wall-normal Reynolds normal stresses, Reynolds shear stress and turbulent kinetic energy in the recirculation and redevelopment regions over the smooth and rough walls are shown in Figure 4.18, 4.19, 4.20 and 4.21, respectively. For each wall condition, the levels of the Reynolds stresses and turbulent kinetic energy are significantly larger in the recirculation and early redevelopment regions than further downstream of the redevelopment region. For example, the turbulent kinetic energy over the smooth wall at the center of primary recirculation bubble and one step height away from the wall, is about 54%

larger than the corresponding turbulent kinetic energy at 15 step heights from reattachment. The elevated Reynolds stresses and turbulent kinetic energy in the recirculation and early redevelopment regions is attributed to the presence of energetic large scale structures associated with a separated shear layer. The decreased levels of Reynolds stresses and turbulent kinetic energy in the redevelopment region may be attributed to the mixing and spreading of the new boundary layer which cause a gradual breakdown of the large scale structures (Bradshaw and Wong, 1972). The enhanced levels of Reynolds stresses and turbulent kinetic energy in the recirculation region and the subsequent decay of the levels in the redevelopment region observed in

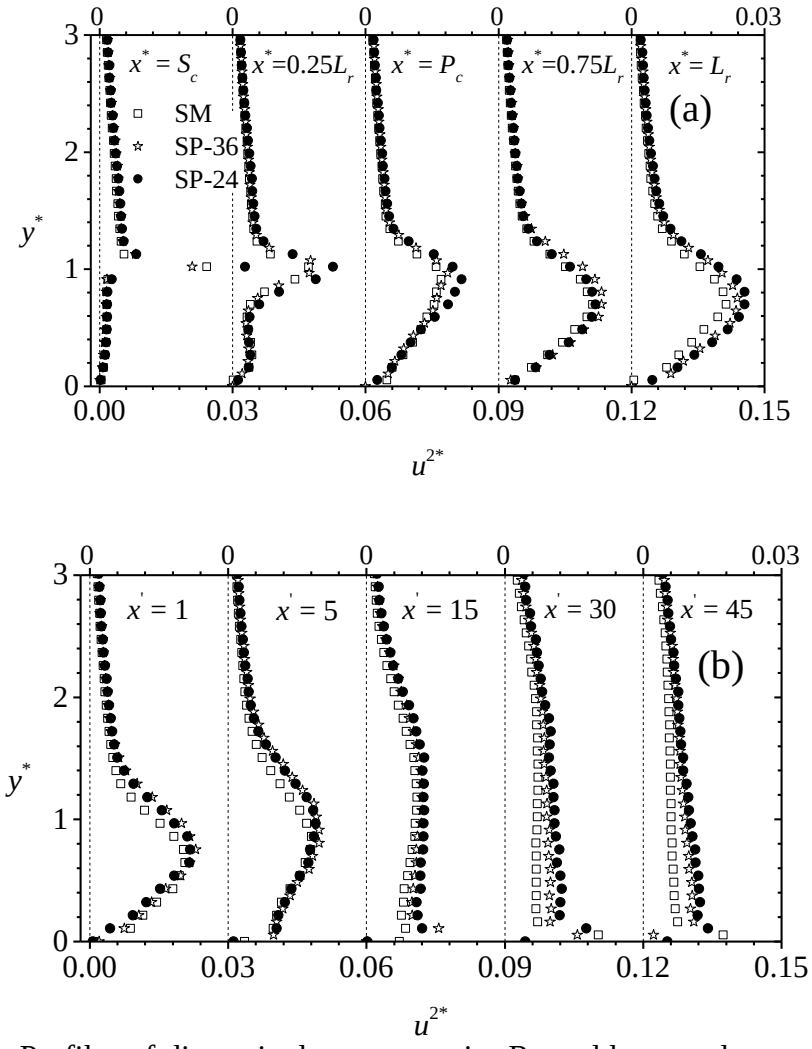

Figure 4.18: Profiles of dimensionless streamwise Reynolds normal stress (u^{2*}) in the recirculation region (a) and redevelopment region (b) over smooth wall (SM), sandpaper 36 grit (SP-36) and sandpaper 24 grit (SP-24).

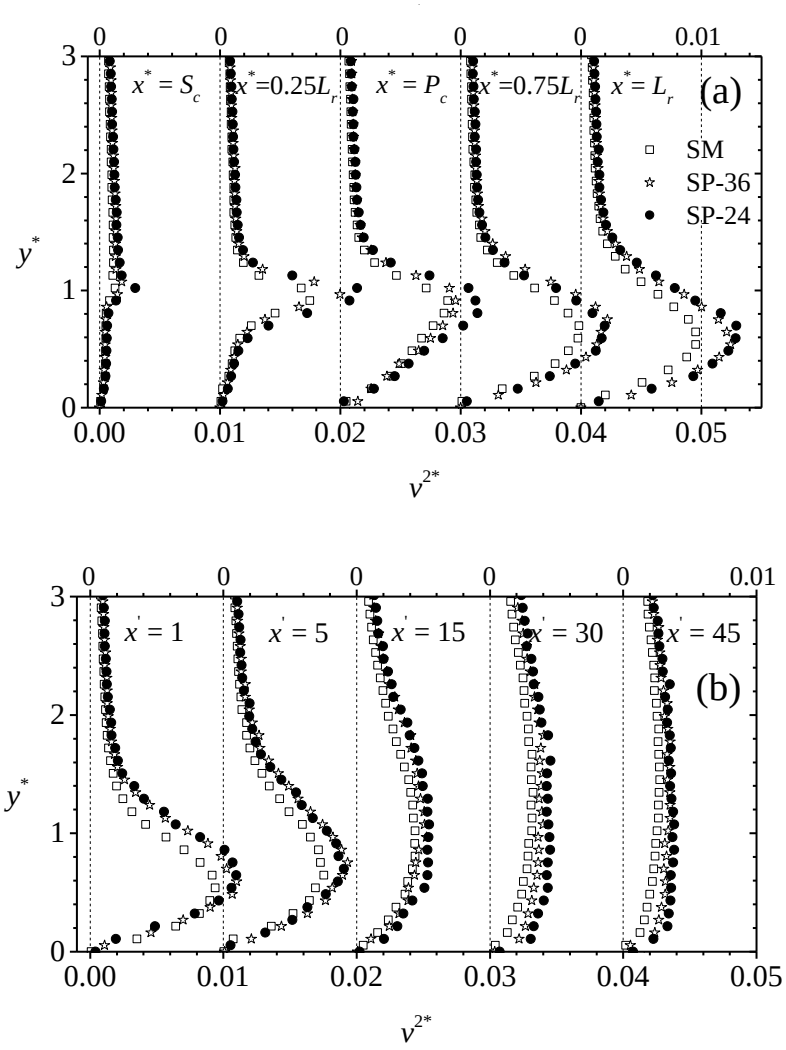

Figure 4.19: Profiles of dimensionless wall-normal Reynolds normal stress (v^{2*}) in the recirculation region (a) and redevelopment region (b) over smooth wall (SM), sandpaper 36 grit (SP-36) and sandpaper 24 grit (SP-24).

the present study, is consistent with previous results obtained in the recirculation and redevelopment region over smooth walls (Kasagi and Matsunaga, 1995; Le et al., 1997). The results also demonstrate that the effects of roughness gradually enhanced the peaks of the Reynolds stresses and turbulent kinetic energy in the recirculation region after ¼ of the reattachment length. At the center of the primary recirculation bubble, for example, the peak value of the turbulent kinetic energy over SP-36 and SP-24 is 9% and 36%, respectively, larger than the corresponding value over the smooth wall. The enhanced levels of streamwise Reynolds normal stress in the

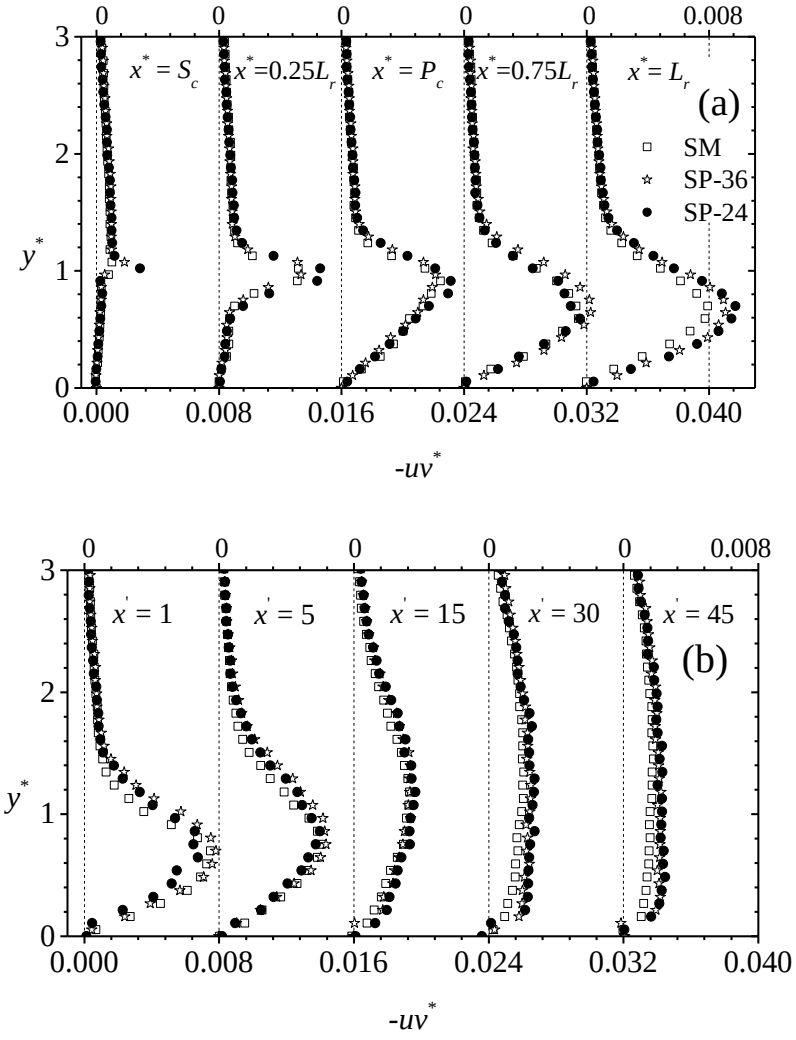

Figure 4.20: Profiles of dimensionless Reynolds shear stress ($-uv^*$) in the recirculation region (a) and redevelopment region (b) over smooth wall (SM), sandpaper 36 grit (SP-36) and sandpaper 24 grit (SP-24).

recirculation region over the rough walls is contrary to the reduced levels of Reynolds normal stresses over rough walls reported by Kim & Chung, 1995 and Ampadu-Mintah et al., 2012. It should be noted that the recirculation region is a rapidly evolving region and effects such as APG, wall roughness and initial flow conditions compete or may combine to significantly alter the flow dynamics. The type of roughness elements, roughness height and topography may also contribute to the impact of roughness that may be observed in the recirculation region. In the redevelopment region, wall roughness enhanced the level of Reynolds stresses and

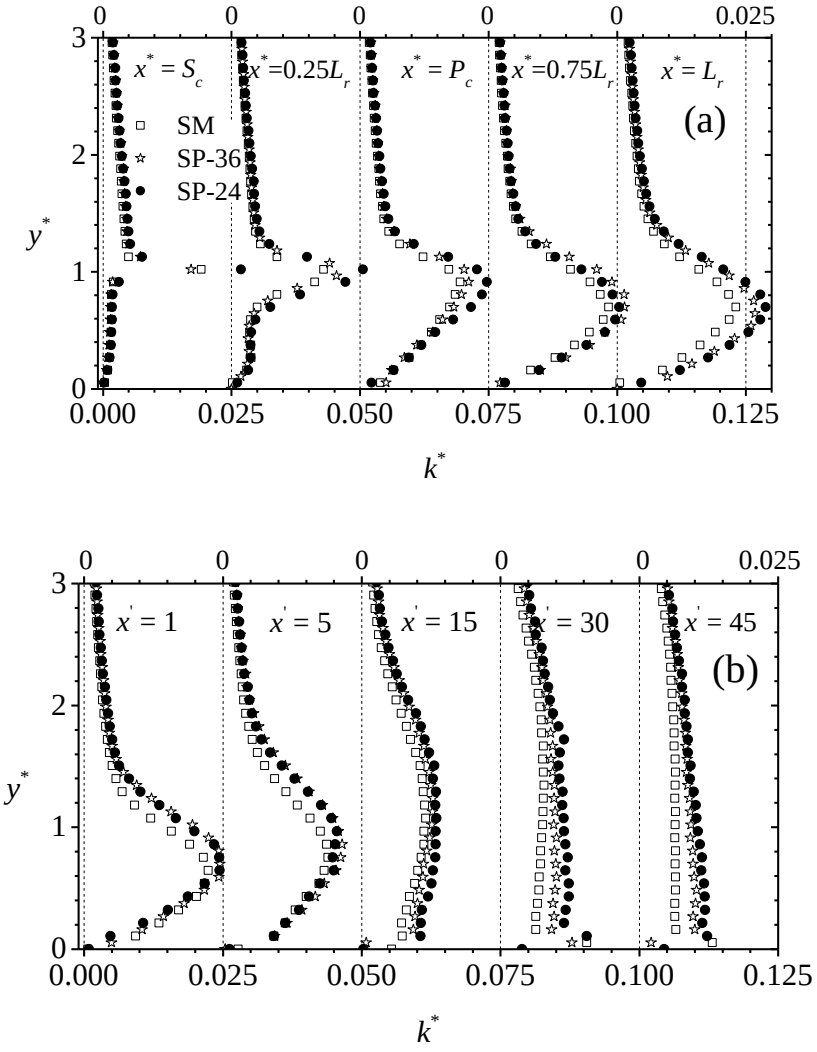

Figure 4.21: Profiles of dimensionless turbulent kinetic energy (k^*) in the recirculation region (a) and redevelopment region (b) over smooth wall (SM), sandpaper 36 grit (SP-36) and sandpaper 24 grit (SP-24).

turbulent kinetic energy in the region adjacent to the rough walls. At the last measurement location ($x' = 45$), for example, the streamwise Reynolds normal stress at 0.4 step height from SP-36 and SP-24 is 61% and 85%, respectively, larger than the corresponding value over SM. The wall-normal Reynolds normal stress at the same location ($x' = 45$ and $y^* = 0.4$) over SP-36 and SP-24 is 60% and 92%, respectively, larger than the corresponding value over SM. At the same location ($x' = 45$ and $y^* = 0.4$), the turbulent kinetic energy over SP-36 and SP-24 is 59% and 80%, respectively, larger than the corresponding value over SM. The profiles of the

Reynolds shear stress at $x' = 45$ show that the Reynolds shear stress at 0.4 step height from the SP-36 and SP-24 wall is 61% and 87%, respectively, larger than the corresponding value over SM. The enhanced levels of Reynolds stresses and turbulent kinetic energy observed in the region adjacent to the rough walls have been reported in previous rough-wall turbulent boundary layer studies (Krogstad et al., 1999; Tachie et al., 2003). Krogstad et al., 1999, for example, observed that the streamwise Reynolds normal stress, wall-normal Reynolds normal stress and Reynolds shear at 0.2 δ from a rough wall is 12%, 42% and 12% larger than corresponding values over a reference smooth wall. In the present study, the levels of Reynolds stresses and turbulent kinetic energy are larger over SP-24 than SP-36 and these may be attributed to the relatively larger average roughness height of SP-24 and the differences in roughness topography between the two rough walls. It should be recalled that the average roughness height of SP-24 is approximately 15% larger than that of SP-36. Furthermore, roughness caused a larger increase in the levels of the wall-normal Reynolds stress than observed in the streamwise Reynolds normal stress. This conclusion is, indeed, consistent with previous studies that examined roughness effects in canonical wall-bounded shear flows (Krogstad et al., 1999).

4.2.3 Reynolds stress ratios and Townsend's structure parameter

The Reynolds stress ratios are often used to investigate the effect of roughness on the large scale anisotropy in the recirculation and redevelopment regions. The ratio of the Reynolds normal stresses (v^2/u^2) is shown in Figure 4.22. It is observed that, for all the three wall conditions, the flow is anisotropic (i.e., $v^2/u^2 \neq 1$) in recirculation and redevelopment regions. Departure from isotropy in the region adjacent to the wall is, however, less dramatic in the recirculation region than in the redevelopment region. For example, the ratio of Reynolds normal stresses (v^2/u^2) at the streamwise location

corresponding to the center of primary recirculation bubble ($x^* = P_c$) and 0.2 step heights away from the smooth wall is 0.50 while the corresponding value at 45 step heights from the reattachment point ($x' = 45$) is 0.23. The increased level of isotropy in the recirculation region is as a result of a more intense mixing in the wall-normal direction in the recirculation region compared to the redevelopment region. It was observed that the individual Reynolds normal stresses were significantly modified by wall roughness both in the recirculation and redevelopment regions but the ratio of the

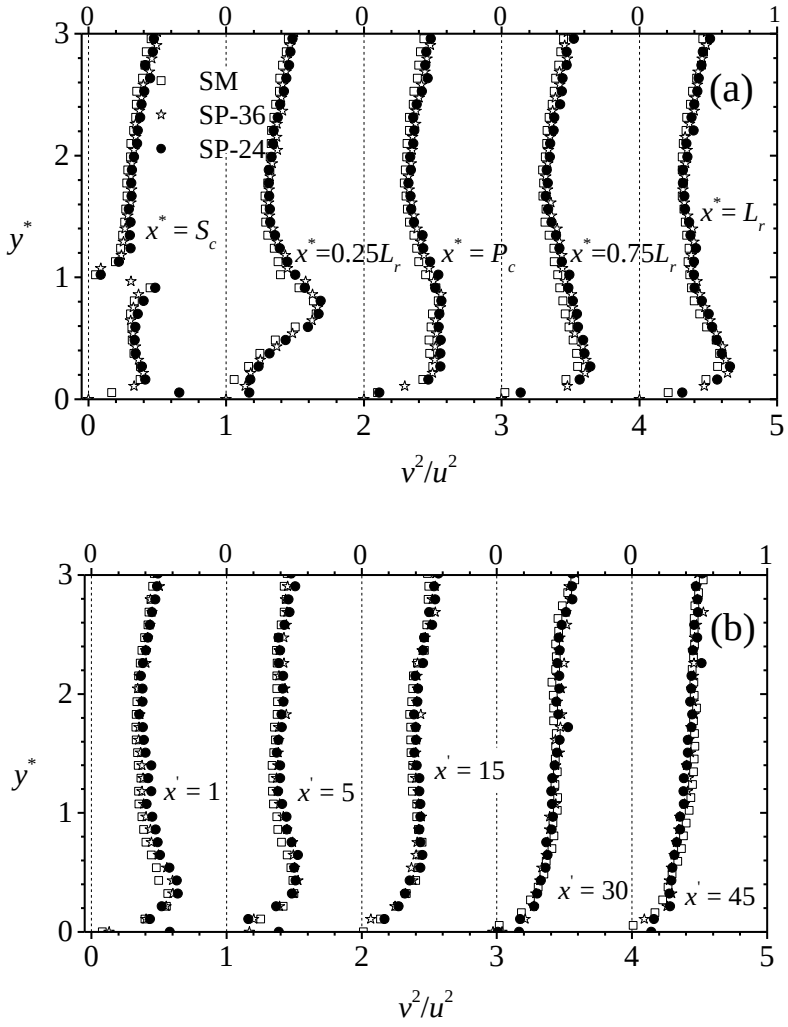

Figure 4.22: Profiles of Reynolds stress ratio, v^2/u^2 in the recirculation region (a) and redevelopment region (b) over smooth wall (SM), sandpaper 36 grit (SP-36) and sandpaper 24 grit (SP-24).

Reynolds normal stresses is independent of roughness in the recirculation and redevelopment regions. The ratio of Reynolds shear stress to the sum of the normal stresses was also evaluated. This ratio, which is often called the Townsend's structure parameter (-*uv*/2*k*), is an important parameter for calibrating the model coefficient, C_μ in the Kolmogorov-Prandtl expression ($\nu_\tau = C_\mu k/L$, where ν_τ is the eddy viscosity, *k* is turbulent kinetic energy and *L* is a length scale). Based on the local equilibrium assumption (i.e., turbulence production = dissipation rate), a value of -*uv*/2*k* = 0.15

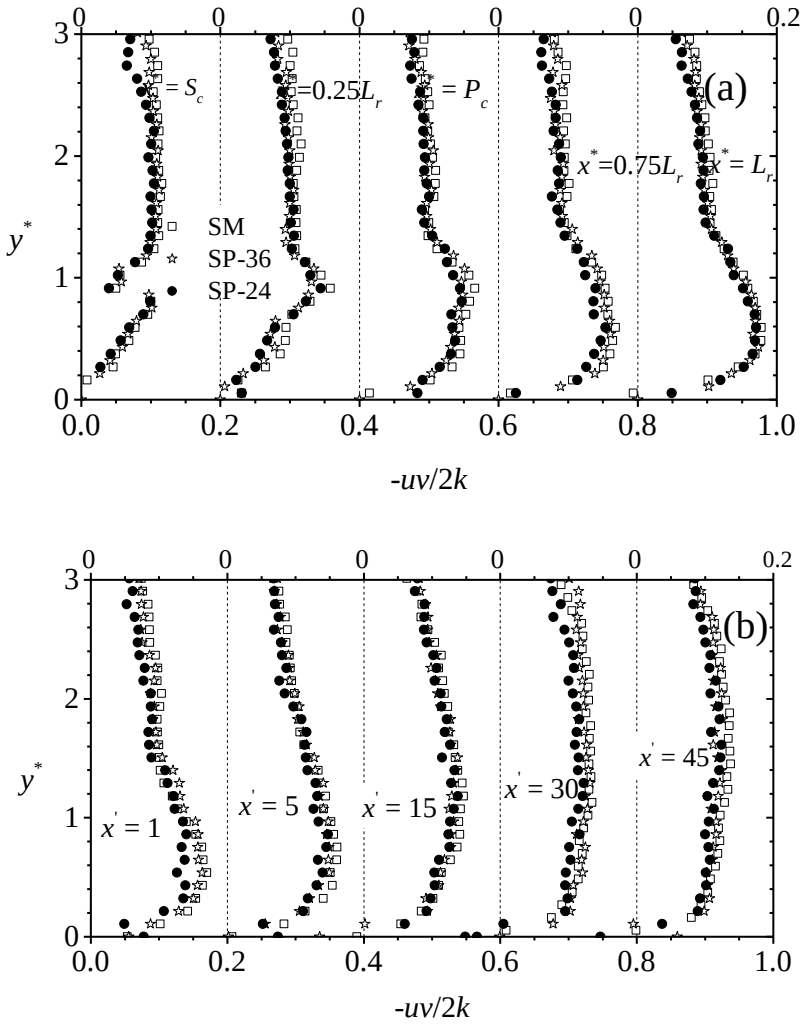

Figure 4.23: Profiles of Townsend's structure parameter, -*uv*/2*k* in the recirculation region (a) and redevelopment region over smooth wall (SM), sandpaper 36 grit (SP-36) and sandpaper 24 grit (SP-24).

(which corresponds to C_μ = 0.09), is often adopted in standard eddy viscosity turbulence models. The results presented in Figure 4.23 demonstrate that, irrespective of wall condition and measurement location, $-uv/2k$ varies appreciably with wall-normal distance. For example, at the center of the primary recirculation bubble ($x^* = P_c$) over the smooth wall, the structure parameter at 0.4 and 1.5 step heights from the wall is 0.14 and 0.10, respectively. At the last measurement station ($x' = 45$) over the smooth wall, the structure parameter at 0.4 and 1.5 step heights from the wall, is 0.11 and 0.14 respectively. Based on the distribution of the structure parameter in the recirculation and redevelopment regions, it can be concluded that the appropriate choice of structure parameter for this complex flow depends on the streamwise distance from the trailing edge of the step and also the wall-normal distance from the wall. Wall roughness does not significantly affect the structure parameter in the recirculation and redevelopment regions.

4.2.4 Triple velocity correlations

The triple velocity correlations are important turbulent statistics because their spatial derivatives constitute the turbulent diffusion terms of the transport equation of Reynolds stresses and turbulent kinetic energy. For example, $\partial(u^3 + uv^2 + uw^2)/\partial x$ and $\partial(u^2v + v^3 + vw^2)/\partial y$ constitute the streamwise and wall-normal diffusion of the turbulent kinetic energy, respectively. Since turbulence diffusion is one of the transport terms that require modelling, refined measurements of triple velocity correlations are critically important for providing the knowledge base necessary to develop more accurate predictive models for the rapidly evolving complex turbulent shear flow investigated in the present study.

The following four triple velocity correlations were evaluated in the present study: u^3, u^2v, v^2u and v^3. The terms uw^2 and vw^2 were not evaluated because the spanwise velocity fluctuation, w, was measured. To have a better insight into the transport of turbulent kinetic energy, the distributions of the streamwise turbulent transport ($u^3 + uv^2$) and wall-normal turbulent transport ($v^3 + u^2v$) in the recirculation and redevelopment regions over the smooth and rough walls are plotted in Figure 4.24 and 4.24, respectively, instead of the conventional u^3, u^2v, v^3, and v^2u. It can be observed from these plots that the transport of turbulent kinetic energy is more intense in the

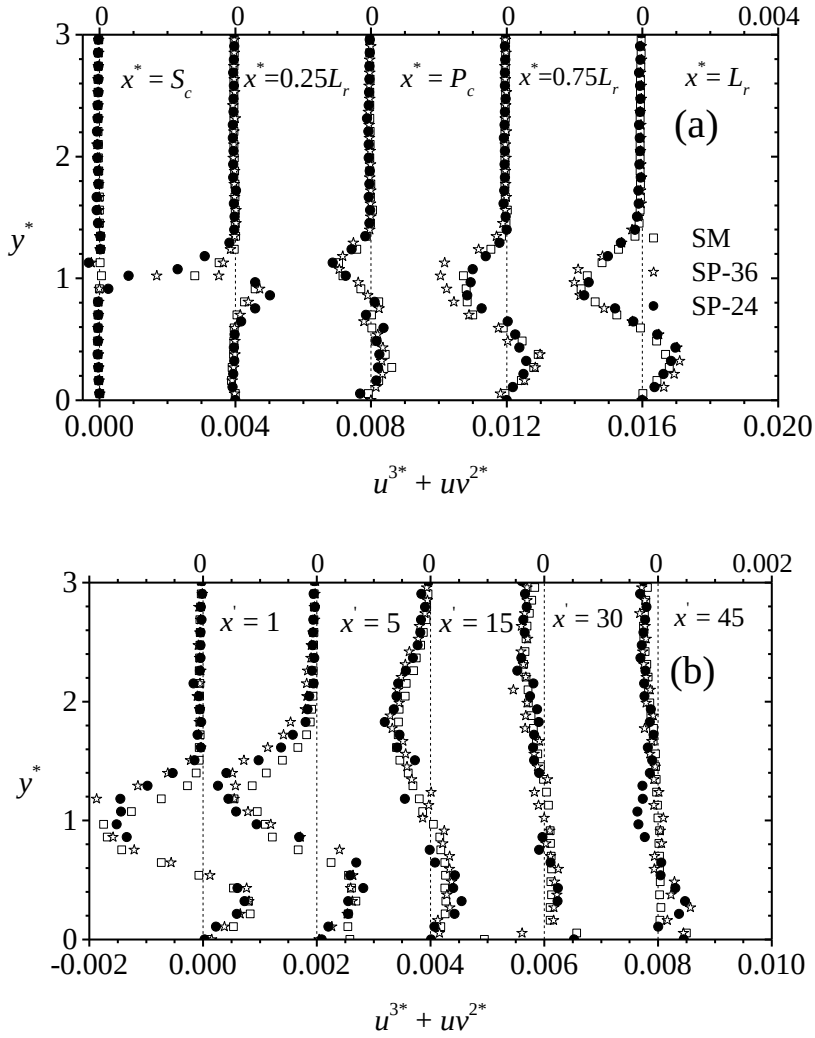

Figure 4.24: Profiles of dimensionless streamwise transport, $u^{3*} + uv^{2*}$ in the recirculation region (a) and redevelopment region (b) over smooth wall (SM), sandpaper 36 grit (SP-36) and sandpaper 24 grit (SP-24).

region prior to reattachment ($P_c \leq x^* \geq L_r$) and the early redevelopment region ($x' = 1$). The intense negative and positive peaks of the streamwise transport ($u^3 + uv^2$) and wall-normal transport ($v^3 + u^2v$) decay as the flow evolves further downstream of reattachment. The decay of the triple velocity correlations in the redevelopment region may be attributed to the mixing and spreading of the new boundary layer which causes the breakdown of the large scale structures responsible for turbulent transport. The profiles of the triple velocity correlation are independent of roughness in the recirculation and redevelopment regions.

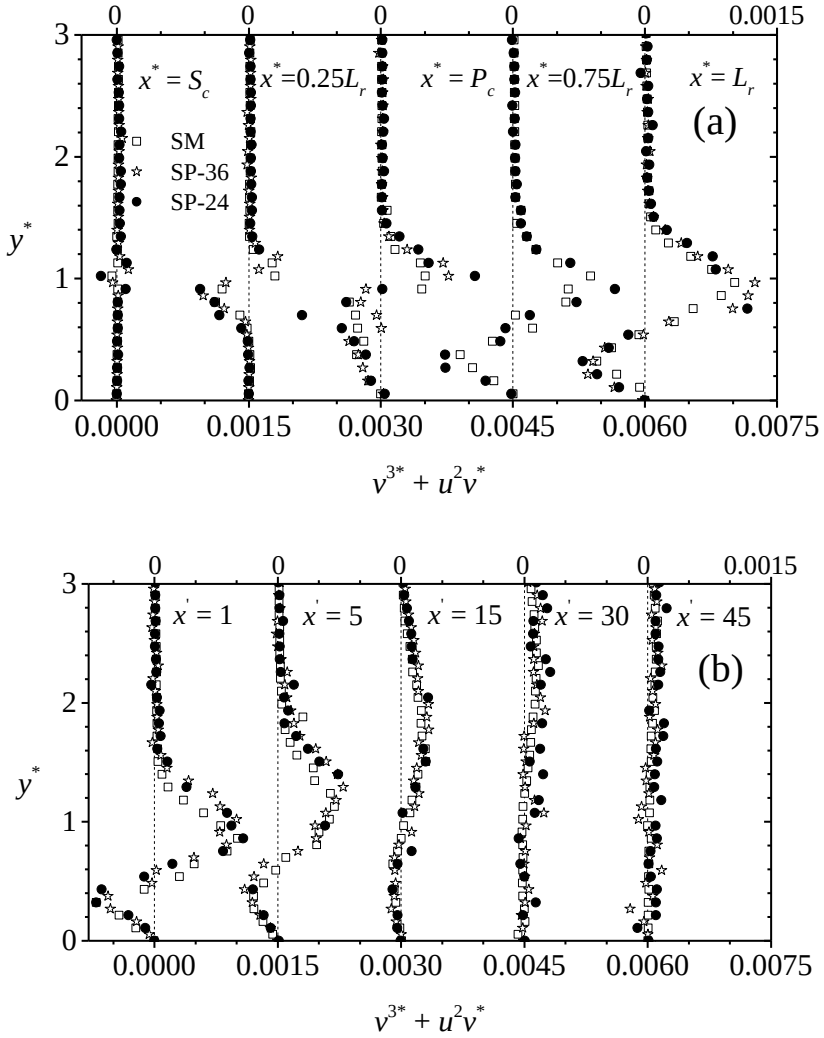

Figure 4.25: Profiles of dimensionless wall-normal transport, $v^{3*}+ u^2v^*$ in the recirculation region (b) and redevelopment region (b) over smooth wall (SM), sandpaper 36 grit (SP-36) and sandpaper 24 grit (SP-24).

4.2.5 Turbulent production

The contributions of the individual terms in the production term of the turbulent kinetic energy transport equation are examined in the recirculation region and redevelopment region. Profiles of the individual terms and the total production term at selected streamwise locations in the recirculation region ($x^* = P_c$, $0.75L_r$ and L_r) and redevelopment region ($x' = 1$, 15, and 45) over SM are shown in Figure 4.26. The results for the two rough walls were observed to be qualitatively similar to those over the smooth wall. Figure 4.26 (a) demonstrates that, the major contributor to turbulent production in the recirculation region is $-uv\partial U/\partial y$ while $-uv\partial V/\partial x$ does not make any

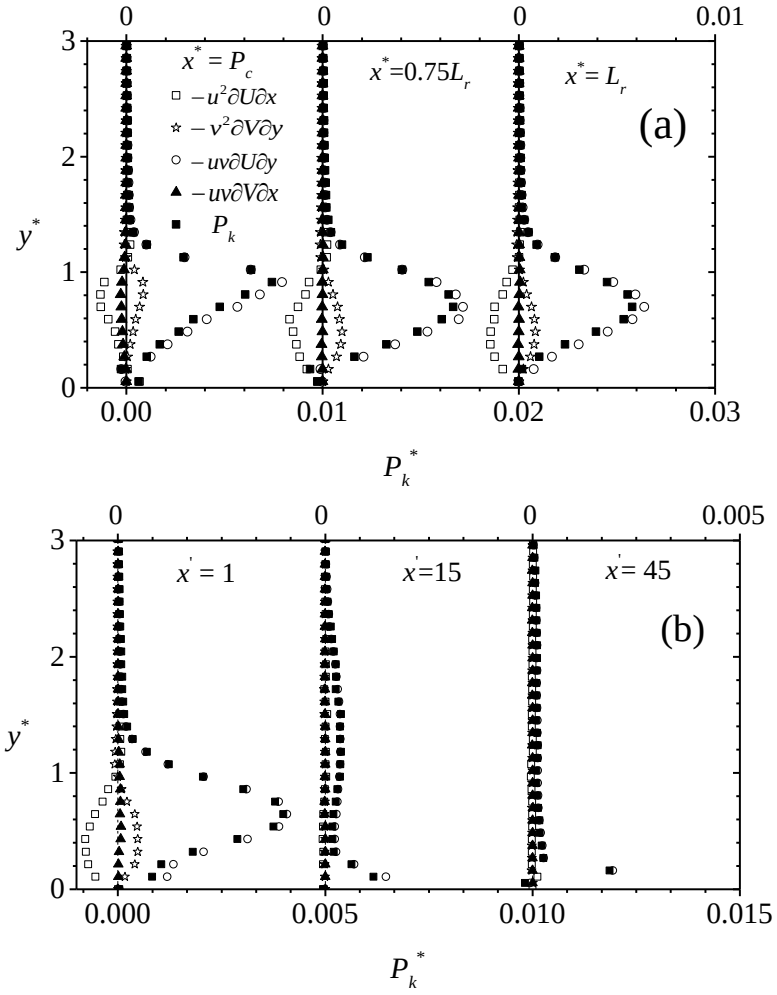

Figure 4.26: Profiles of the individual terms of the total production term of the transport equation of turbulent kinetic energy (P_k^*) in the recirculation region (a) and redevelopment region (b) over smooth wall (SM).

substantial contribution. Individually, the levels of $-u^2\,\partial U/\partial x$ and $-v^2\,\partial V/\partial y$ are not negligible in the recirculation regions. However, they are of similar magnitude but opposite in sign so that their sum is small in comparison to $-uv\partial U/\partial$y. It should be recalled that the sum of $-u^2\,\partial U/\partial x$ and $-v^2\,\partial V/\partial y$ was observed in contour plots of P_n (Figure 4.12 (a)) to be marginally negative. Thus, the contribution from the normal stresses acts as an 'energy sink', and lead to a marginal reduction in the level of production of turbulent kinetic energy in the separated shear layer. Although the normal stresses ($-u^2\partial U/\partial x$ and $-v^2\,\partial V/\partial y$) do not contribute significantly to the

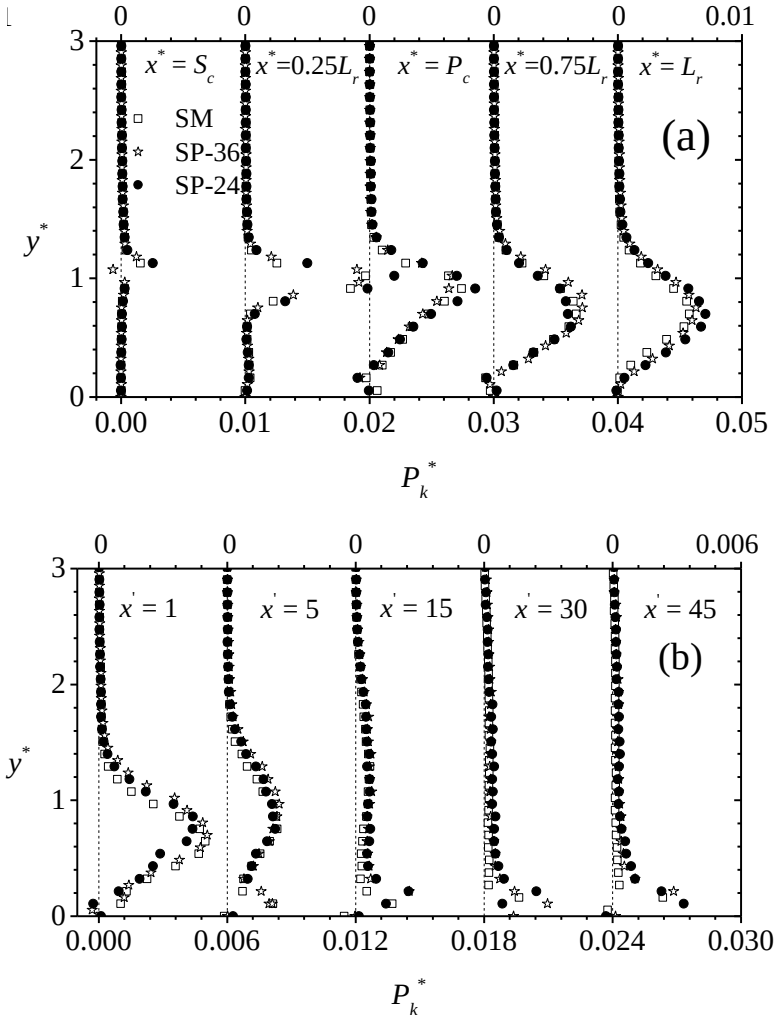

Figure 4.27: Profiles of dimensionless turbulent production of the transport equation of turbulent kinetic energy (P_k^*) in the recirculation region (a) and redevelopment region (b) over smooth wall (SM), sandpaper 36 grit (SP-36) and sandpaper 24 grit (SP-24).

production of turbulent kinetic energy because of their opposing effects, they have substantial impact on the level of the Reynolds normal stresses in the recirculation regions. For example, the negative values of $-u^2\ \partial U/\partial x$ will attenuate the level of production of streamwise Reynolds normal stress ($P_{uu} = -u^2\ \partial U/\partial x - uv\ \partial U/\partial y$). On the contrary, the positive values of $-v^2\ \partial V/\partial y$ will enhance the production ($P_{vv} = -v^2\ \partial V/\partial y - uv\ \partial V/\partial x$) and hence the level of the wall-normal Reynolds normal stress. The reduction in production of streamwise Reynolds normal stress and an increase in production of wall-normal Reynolds normal stress within the recirculation region are partly responsible for the higher degree of isotropy observed in the recirculation than in the redevelopment region.

As can be observed at $x' = 15$ and 45 (Figure 4.26 (b)), the contributions from $-u^2\ \partial U/\partial x$ and $-v^2\ \partial V/\partial y$ are negligible or identically zero at the later stage of flow redevelopment so that $-uv\partial U/\partial y$ accounts for virtually the entire production of turbulence (since $-uv\partial V/\partial x$ is also negligible).

The distributions of the total turbulent production in the recirculation and redevelopment regions over SM, SP-36 and SP-24 are compared in Figure 4.27 to examine any effects of wall roughness. Similar to the distributions of the Reynolds stresses, the level of turbulent production over all the wall conditions is significantly larger in the recirculation and early redevelopment region than it is further downstream of reattachment. Roughness also increases the level of production in the recirculation and redevelopment regions, which is consistent with the enhanced level of Reynolds stresses observed in Section 4.2.3. For example, the peak of the production at the center of primary recirculating bubble ($x^* = P_c$) over SP-24 is 14% larger than the corresponding value over SM. On the contrary, the peak of the

production term at the center of primary recirculating bubble ($x^* = P_c$) over SP-36 is 10% smaller than the corresponding value over SM. At the last measurement location, $x' = 45$, for example, the peak of the production over SP-36 and SP-24 is 54% and 24%, respectively, larger than the corresponding value over SM.

4.3 Multi-point turbulent statistics

In this section, two-point auto correlation function and proper orthogonal decomposition are applied to extract some statistical features of coherent structures and to examine the impact of roughness on these structures within the recirculation and redevelopment regions.

4.3.1 Two-point auto-correlation

Traditionally, two-point correlations are used to analyse spatial correlation between the velocity fluctuations, evaluate the integral length scales and Taylor micro-scales and investigate statistical features in both wall-bounded and free shear turbulent flows. For example, Christensen and Wu, 2005 and Volino et al., 2007 employed two-point correlation functions to estimate the average extents and angle of inclination of the hairpin packets in smooth and rough wall turbulent boundary layers.

The two-point auto-correlation function (R_{AB}) between any two arbitrary quantities A (x_{ref}, y_{ref}) and B (x_{ref}, y_{ref}) is evaluated as follows:

$$R_{AB}(x_{ref}, y_{ref}) = \frac{\langle A(x_{ref},y_{ref})B(x_{ref}+\Delta x,y_{ref}+\Delta y)\rangle}{\langle \sigma_A(x_{ref},y_{ref})\sigma_B(x_{ref}+\Delta x,y_{ref}+\Delta y)\rangle} \quad (4.1)$$

where the point (x_{ref}, y_{ref}) denotes the reference location, Δx and Δy are the spatial separations between A and B in the streamwise and wall-normal directions, respectively, and σ_A and σ_B are the root-mean-square values of A and B at (x_{ref}, y_{ref}) and ($x_{ref} + \Delta x$, $y_{ref} + \Delta y$), respectively.

In the present study, the two-point correlation functions of the velocity fluctuations were calculated for each PIV realization and then ensemble-averaged point-by-point. To visualize the spatial coherence of the structures, typical contours of the streamwise (R_{uu}) and wall-normal (R_{vv}) auto-correlation functions obtained at streamwise locations in the recirculation region ($x^* = P_c$), early redevelopment region ($x' = 1$) and later stage of redevelopment ($x' = 45$) over the smooth (SM) and rough (SP-24) walls are shown in Figure 4.28 to 4.33. At each streamwise location, the contours were extracted at two different wall-normal locations, $y^* = 0.5$ and $y^* = 1.0$, to explore the effect of roughness on the spatial structures with increasing distance from the wall. In

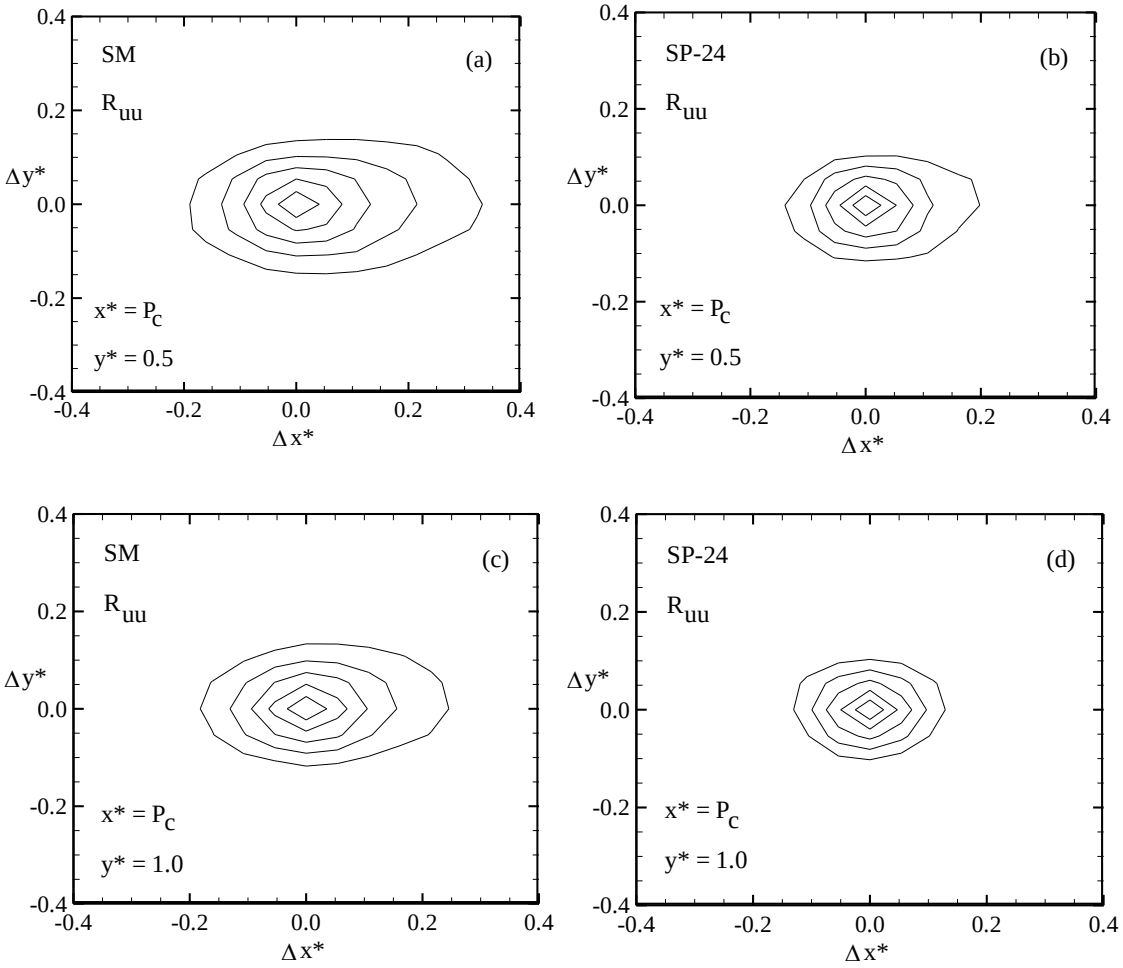

Figure 4.28: Contour plots of streamwise two-point auto-correlation function (R_{uu}) at $x^* = P_c$ over smooth wall, SM (a, c) and sandpaper 24 grit, SP-24 (b, d). Note that contour levels range from 0.5 to 0.9 in each plot.

each plot, the highest and lowest contour levels are respectively 0.9 and 0.5, and the contours are at intervals of 0.1. Figure 4.28- 4.29 demonstrate that, irrespective of the wall condition, the physical size of the spatial structures embodied in the streamwise auto-correlation function increases as the flow evolves from the recirculation region and to the redevelopment region. The elongated shape of the contours suggest that the spatial structures embodied in the streamwise auto- correlation functions are more organised in the streamwise direction than in the wall-normal direction. In the recirculation region (Figure 4.28), the contours of the streamwise auto-correlation functions over the smooth and rough walls at y^* = 0.5 are larger than the

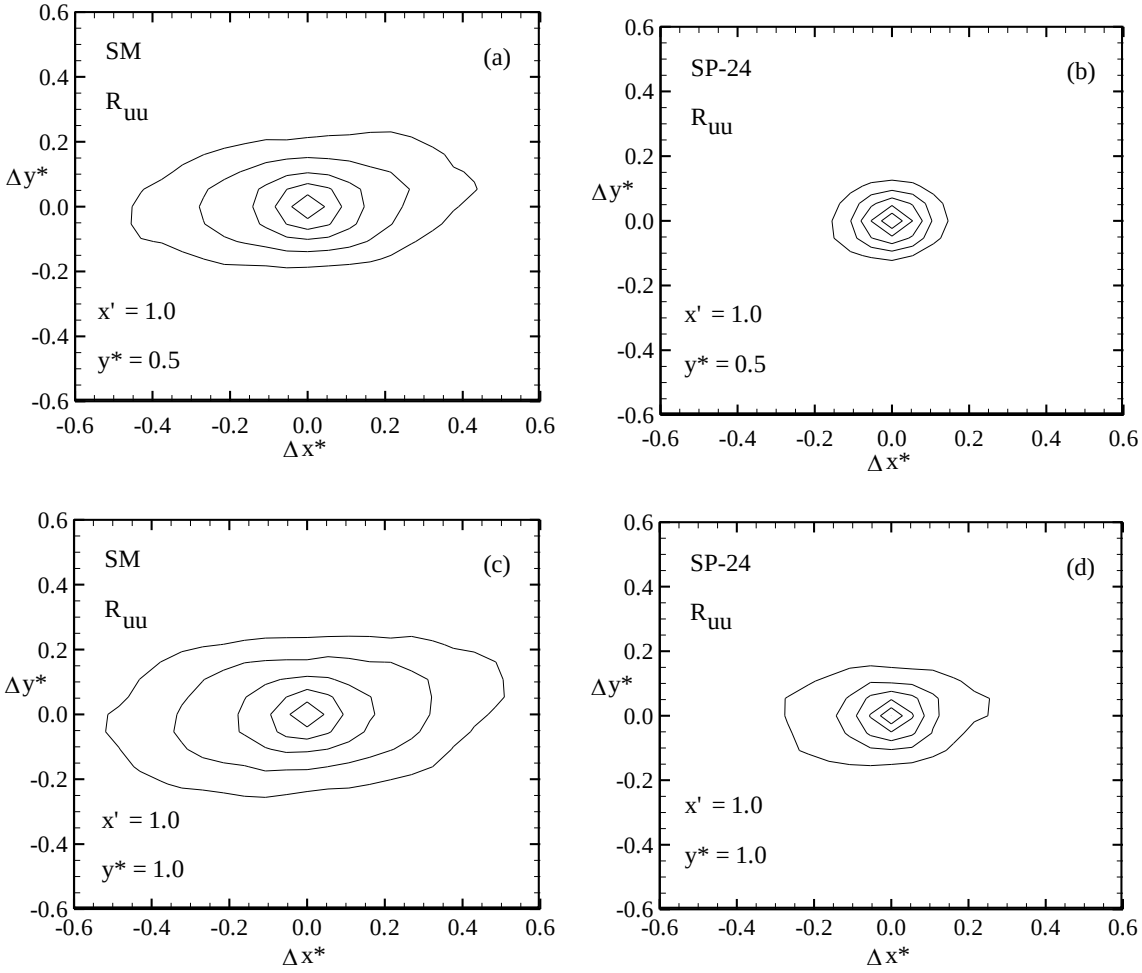

Figure 4.29: Contour plots of streamwise auto-correlation function (R_{uu}) at x' = 1.0 over smooth wall, SM (a, c) and sandpaper 24 grit, SP-24 (b, d). Note that contour levels range from 0.5 to 0.9 in each plot.

corresponding contours at y^* = 1.0. On the contrary, the contours of the streamwise auto-correlation functions at y^* = 0.5 in the redevelopment region (Figure 4.29 - 4.30) are smaller than the corresponding contours at y^* = 1.0, irrespective of the wall condition. The enhanced size of the contours at y^* = 0.5 in the recirculation region indicate that the spatial structures embodied in the streamwise auto- correlation functions are more strongly correlated in the recirculation bubble (i.e. y^* = 0.5) than one step height away from the wall (y^* = 1.0). In the redevelopment region, the large scale structures in the outer region may be responsible for the larger size of the contours further away from the wall. The contours of streamwise auto-correlation

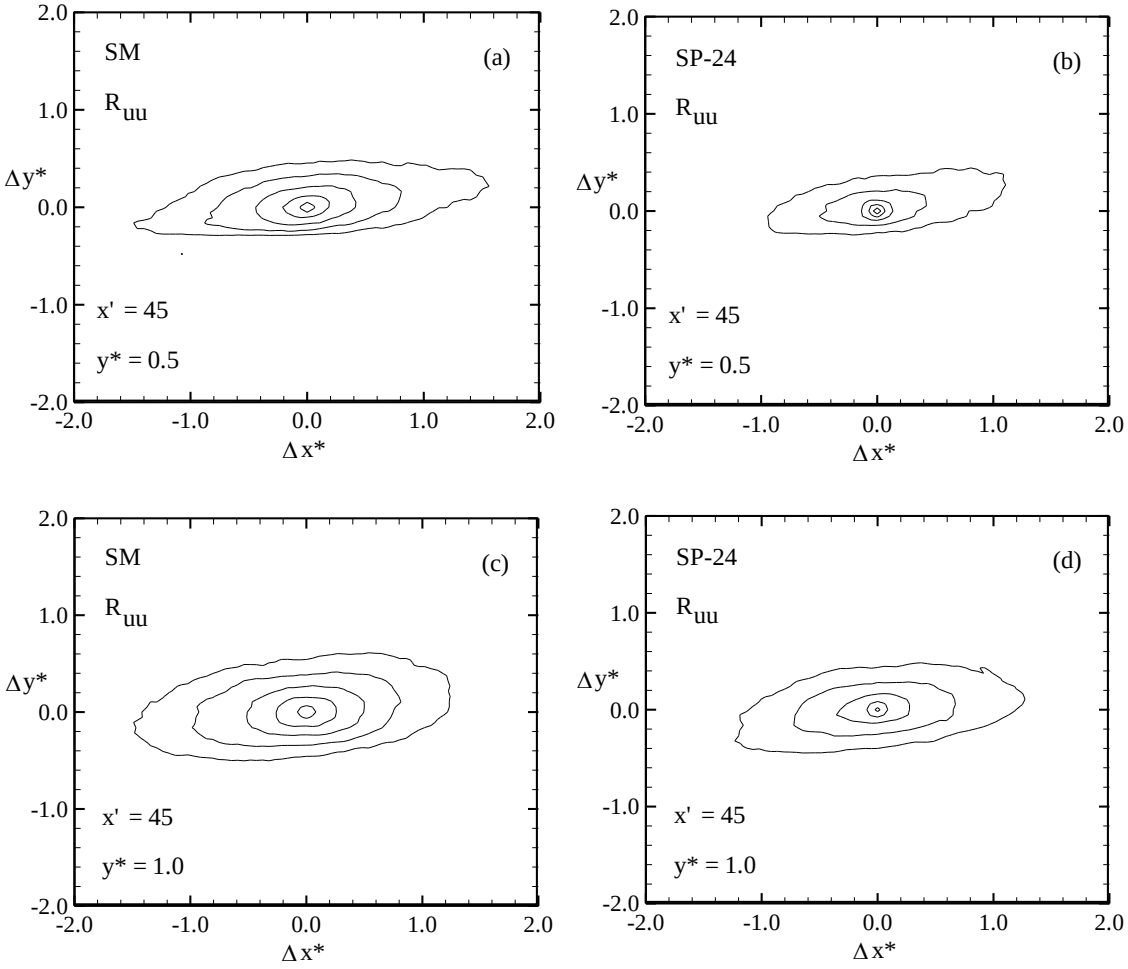

Figure 4.30: Contour plots of streamwise auto-correlation function (R_{uu}) at x' = 45 over smooth wall, SM (a, c) and sandpaper 24 grit, SP-24 (b, d). Note that contour levels range from 0.5 to 0.9 in each plot.

function at $x' = 45$ show streamwise inclinations which are thought to be related to the average inclination of the hairpin packets. The average angle of inclination was estimated to be 10° for the smooth and rough walls. The impact of roughness reduced the size of the contours of the streamwise auto-correlation function, irrespective of the measurement location.

The size of the spatial structures embodied in the wall-normal auto-correlation function (as shown in Figure 4.31 - 4.33), increases with increasing streamwise distance away from the trailing edge of the step. Unlike the streamwise auto-

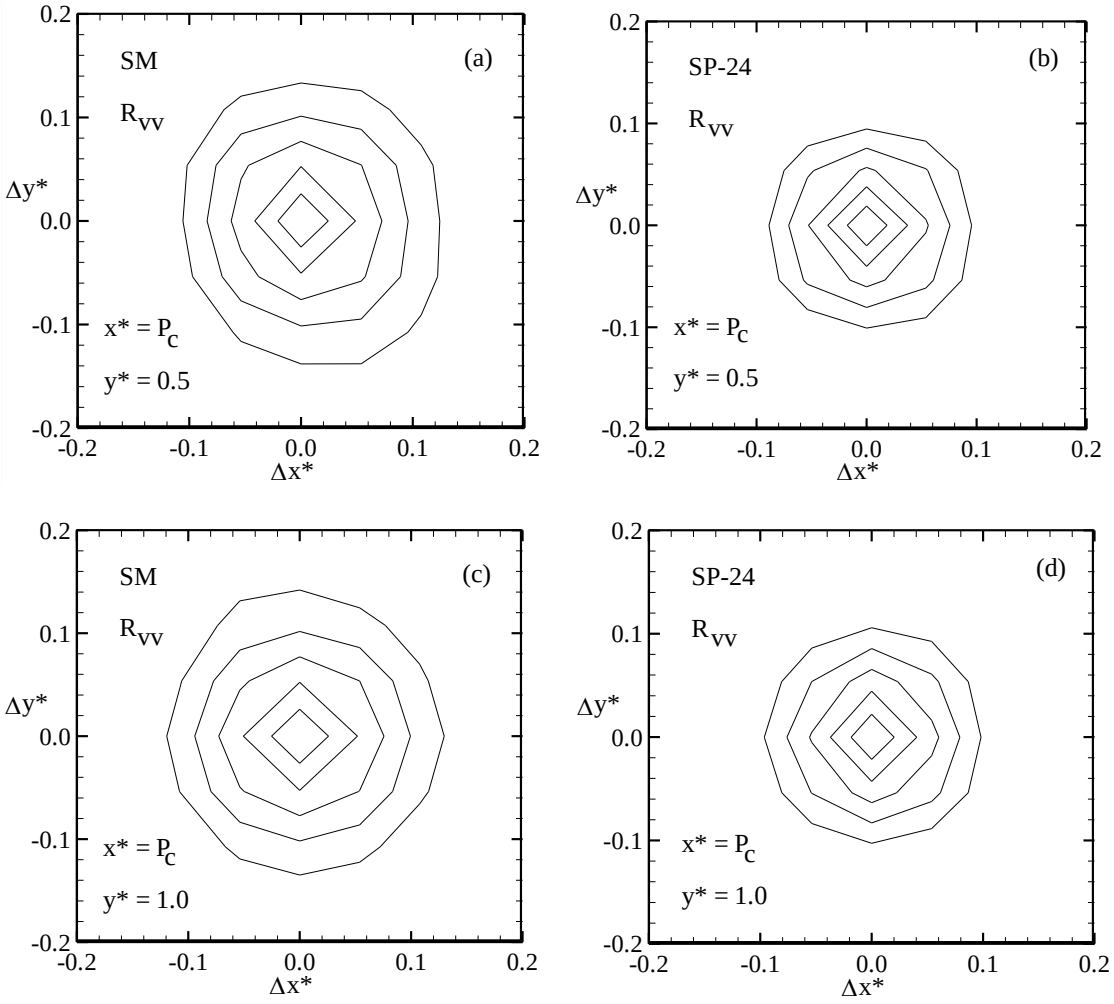

Figure 4.31: Contour plots of wall-normal auto-correlation function (R_{vv}) at $x^* = P_c$ over smooth wall, SM (a, c) and sandpaper 24 grit, SP-24 (b, d). Note that contour levels range from 0.5 to 0.9 in each plot.

correlation function, the contours of wall-normal auto-correlation function over the smooth and rough walls are more rounded and compact, in agreement with previous studies on smooth and rough wall turbulent boundary layers (Volino et al., 2007; Wu and Christensen, 2010). In the recirculation region (Figure 4.31) and early redevelopment region (Figure 4.32), the contours of the wall-normal auto-correlation function at y^* = 0.5 and y^* = 1.0 are similar in size but at the later stage of the redevelopment region (Figure 4.33), the size of the contours increases with increasing wall-normal distance from the respective smooth and rough wall. Similar to the

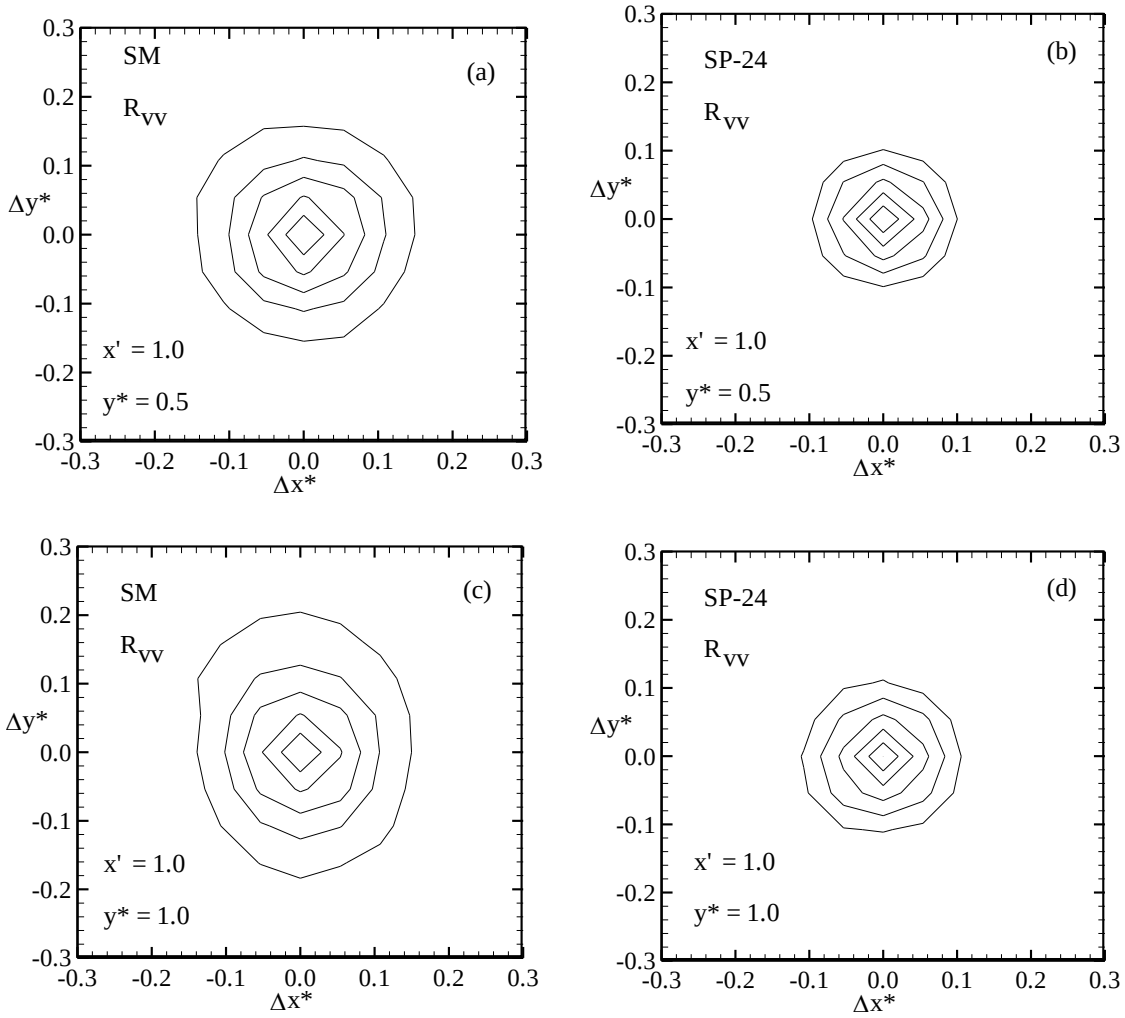

Figure 4.32: Contour plots of wall-normal auto-correlation function (R_{vv}) at x' = 1.0 over smooth wall, SM (a, c) and sandpaper 24 grit, SP-24 (b, d). Note that contour levels range from 0.5 to 0.9 in each plot.

streamwise auto-correlation function, wall roughness reduced the spatial coherence of the structures embodied in the wall-normal auto-correlation function in both the recirculation and redevelopment regions.

The size of the turbulence structure can be estimated using streamwise and wall-normal extents of the streamwise and wall-normal auto-correlation function contours. These extents are thought to represent the average size of the hairpin packets (Christensen and Wu, 2005; Volino et al., 2007). The streamwise extent (Lx_{uu}) of the streamwise auto-correlation function (R_{uu}) is defined as twice the distance from the

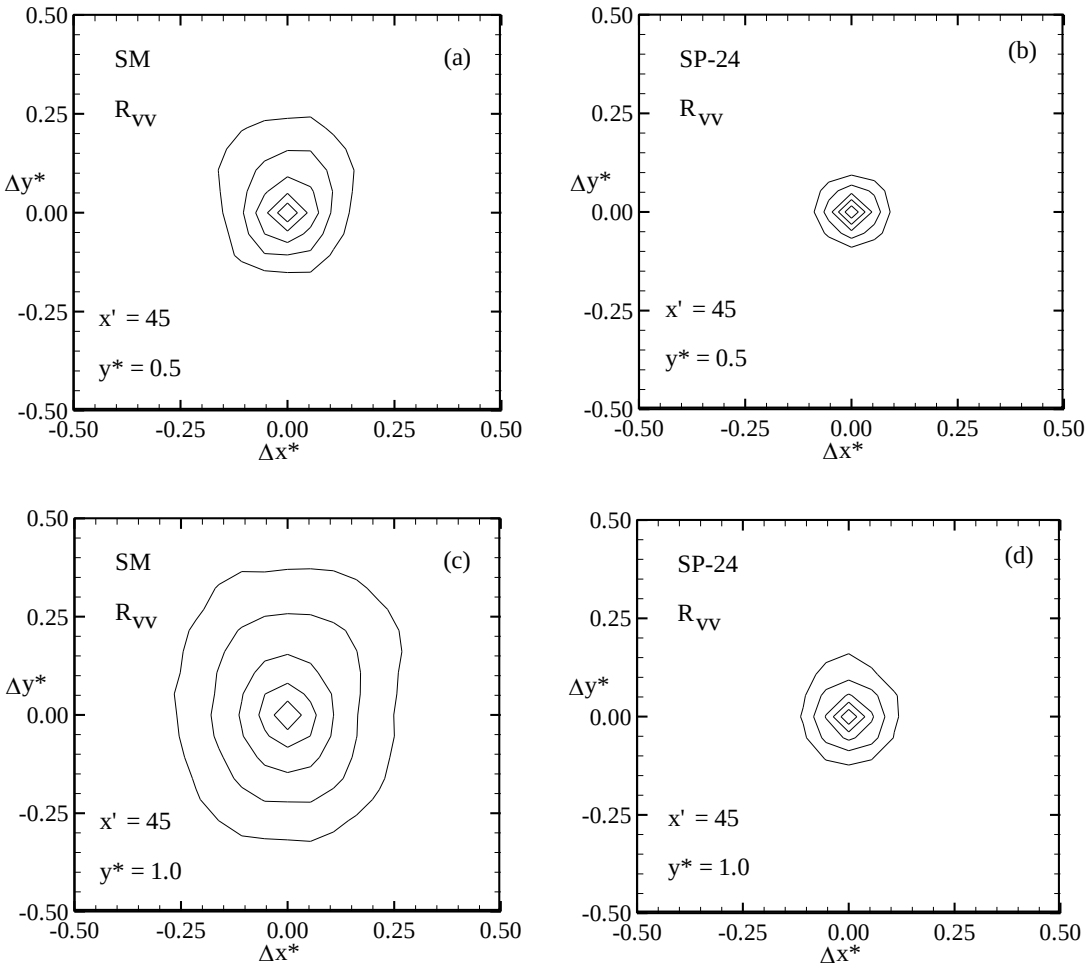

Figure 4.33: Contour plots of wall-normal auto-correlation function (R_{vv}) at $x' = 45$ over smooth wall, SM (a, c) and sandpaper 24 grit, SP-24 (b, d). Note that contour levels range from 0.5 to 0.9 in each plot.

self-correlation peak to the most downstream location on the 0.5 contour while the wall-normal extent (Ly_{uu}) is defined as the wall-normal distance between points closest and farthest on the 0.5 contour level. The streamwise (Lx_{vv}) and wall-normal (Ly_{vv}) extents of wall-normal auto-correlation function (R_{vv}) are defined as the respective streamwise and wall-normal distances between points closest and farthest on the 0.5 contour level. To quantify the impact of roughness on the characteristic size of the turbulence structures, distributions of the average extents of streamwise and wall-normal auto-correlation function contours were obtained at selected streamwise locations in the recirculation region ($x^* = P_c$) and redevelopment region ($x' = 1$ and 45) over the smooth wall (SM) and rough walls (SP-36 and SP-24).

The distributions of the streamwise and wall-normal extents of the streamwise auto-correlation function are shown in Figure 4.34 and 4.35, respectively. For each wall condition, the distributions of the streamwise and wall-normal extents of the streamwise auto-correlation function are significantly different at each measurement location. In the recirculation region, for example, the streamwise wall-normal extents gradually decrease with increasing wall-normal distance from the center of the primary recirculation bubble ($y^* = 0.3$) to one step height away from the wall. Beyond one step height, the distributions of extents rapidly increase with increasing wall-normal distance. For example, the value of Lx_{uu} at the center of the primary recirculation bubble ($y^* = 0.3$) over the smooth wall is 25% larger than the corresponding value at 0.9 step height from the wall but 120% smaller than the corresponding value at 1.5 step height way from the wall. In the early redevelopment region ($x' = 1$), the streamwise and wall-normal extents of the streamwise auto-correlation function show a gradual increase with increasing wall-normal distance away from the wall. Further downstream ($x' = 45$), these distributions rapidly increase

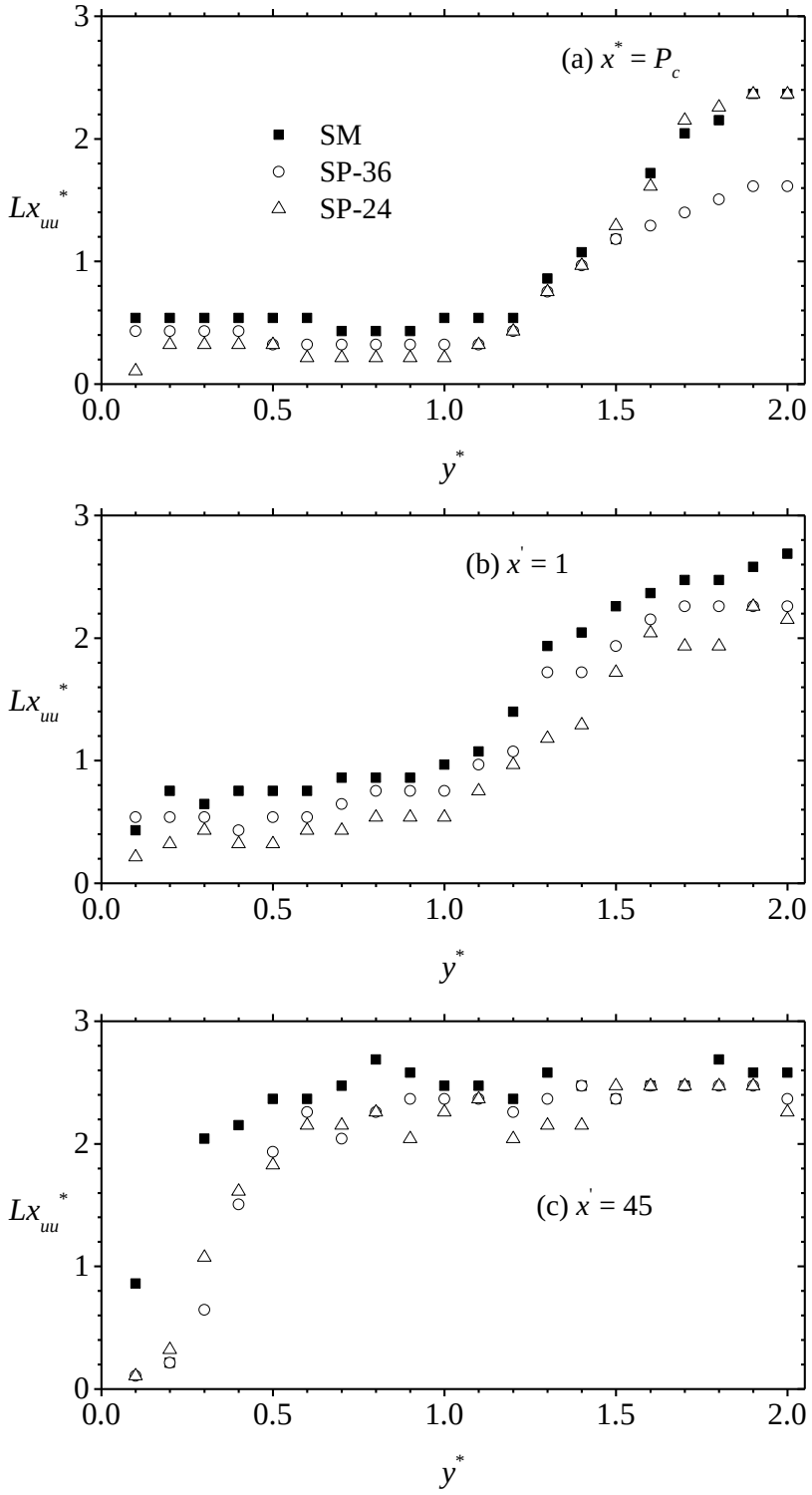

Figure 4.34: Distribution of the streamwise extents (Lx_{uu}) of the streamwise auto-correlation function (R_{uu}) in the recirculation region (a), early redevelopment region (b) and further downstream of the redevelopment region (c) over smooth wall (SM), sandpaper 36 grit (SP-36) and sandpaper 24 grit (SP-24).

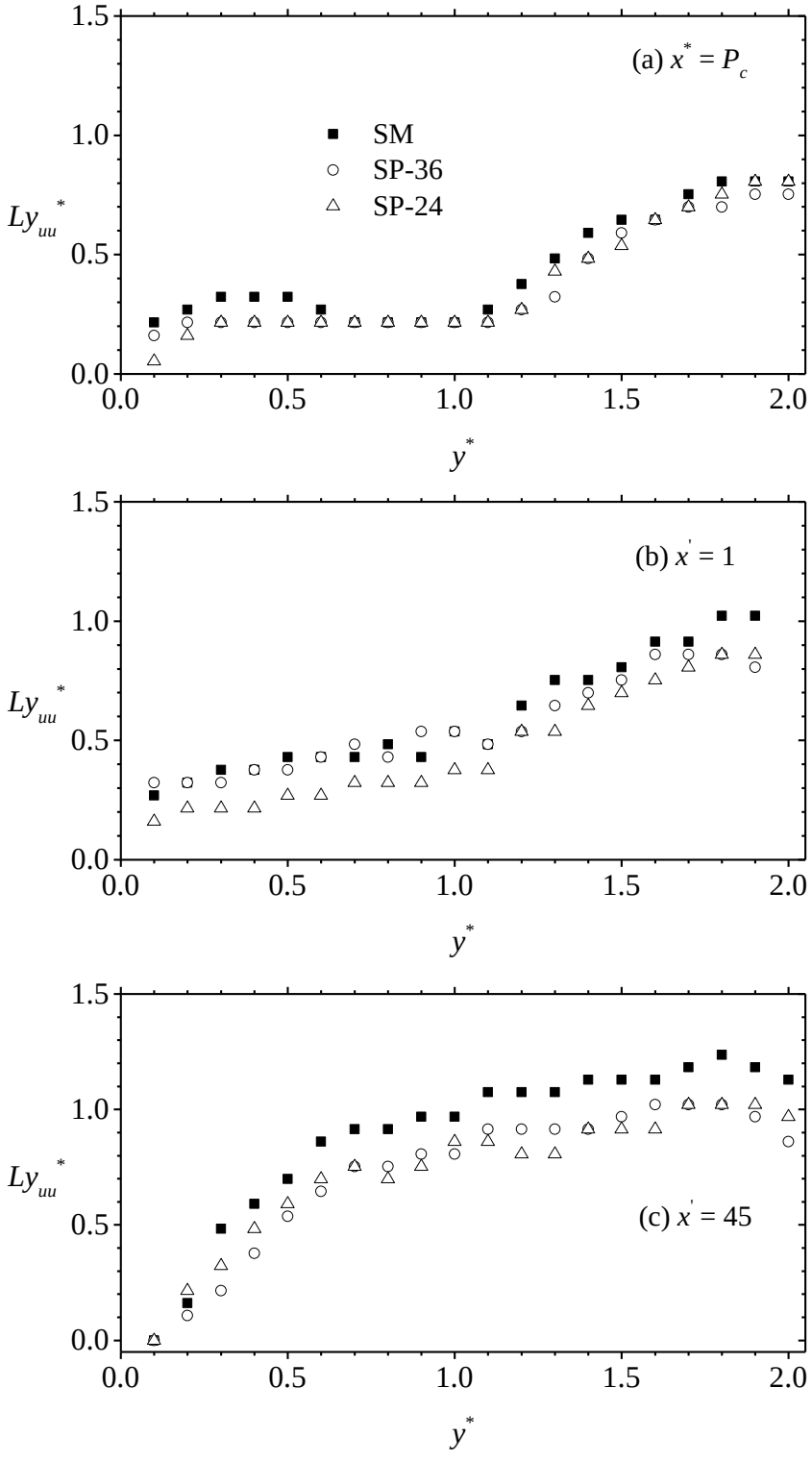

Figure 4.35: Distribution of the wall-normal extents (Ly_{uu}) of the streamwise auto-correlation function (R_{uu}) in the recirculation region (a), early redevelopment region (b) and further downstream of the redevelopment region (c) over smooth wall (SM), sandpaper 36 grit (SP-36) and sandpaper 24 grit (SP-24).

with increasing wall-normal distance in the region extending from the wall to 0.7 step height away from the wall ($y^* < 0.7$) but remain approximately constant beyond 0.7 step height away from the wall. The distributions of the streamwise and wall-normal extents of the streamwise auto-correlation function at $x' = 45$ compare well with previous measurements in smooth and rough wall turbulent boundary layers (Volino et al., 2007).

In agreement with the contour plots, the distributions of the streamwise and wall-normal extents of the streamwise auto-correlation function are reduced over the rough walls compared to the smooth wall. At the center of primary recirculation bubble ($x^* = Pc$, $y^* = 0.3$), for example, SP-36 and SP-24 reduced the values of Lx_{uu} by 20% and 40%, respectively, compared with the corresponding value over SM. The value of Ly_{uu} over the rough walls at the center of primary recirculation bubble ($x^* = P_c$, $y^* = 0.3$) is 33% smaller than the corresponding value over the smooth wall. Further downstream, ($x' = 45$) and 0.5 step height way from wall, the values of Lx_{uu} over SP-36 and SP-24 are 18% and 33%, respectively, smaller than the corresponding value over SM. At the same location ($x' = 45$, $y^* = 0.5$), roughness effect due to SP-36 and SP-24 reduced the wall-normal extent of the streamwise auto-correlation function by 23% and 15% compared with the corresponding value over SM. The results presented in Figure 4.34 and 4.35 suggest that the impact of roughness is stronger on the streamwise extent than the wall-normal extent of the streamwise auto-correlation function in the region adjacent to the rough walls ($y^* < 1$). The reduced streamwise extent of the streamwise auto-correlation function over the rough walls is in agreement with results for smooth and rough wall turbulent boundary layers (Krogstad and Antonia, 1994). However, the reduced wall-normal extent of the streamwise auto-correlation function over the rough walls is contrary to the results

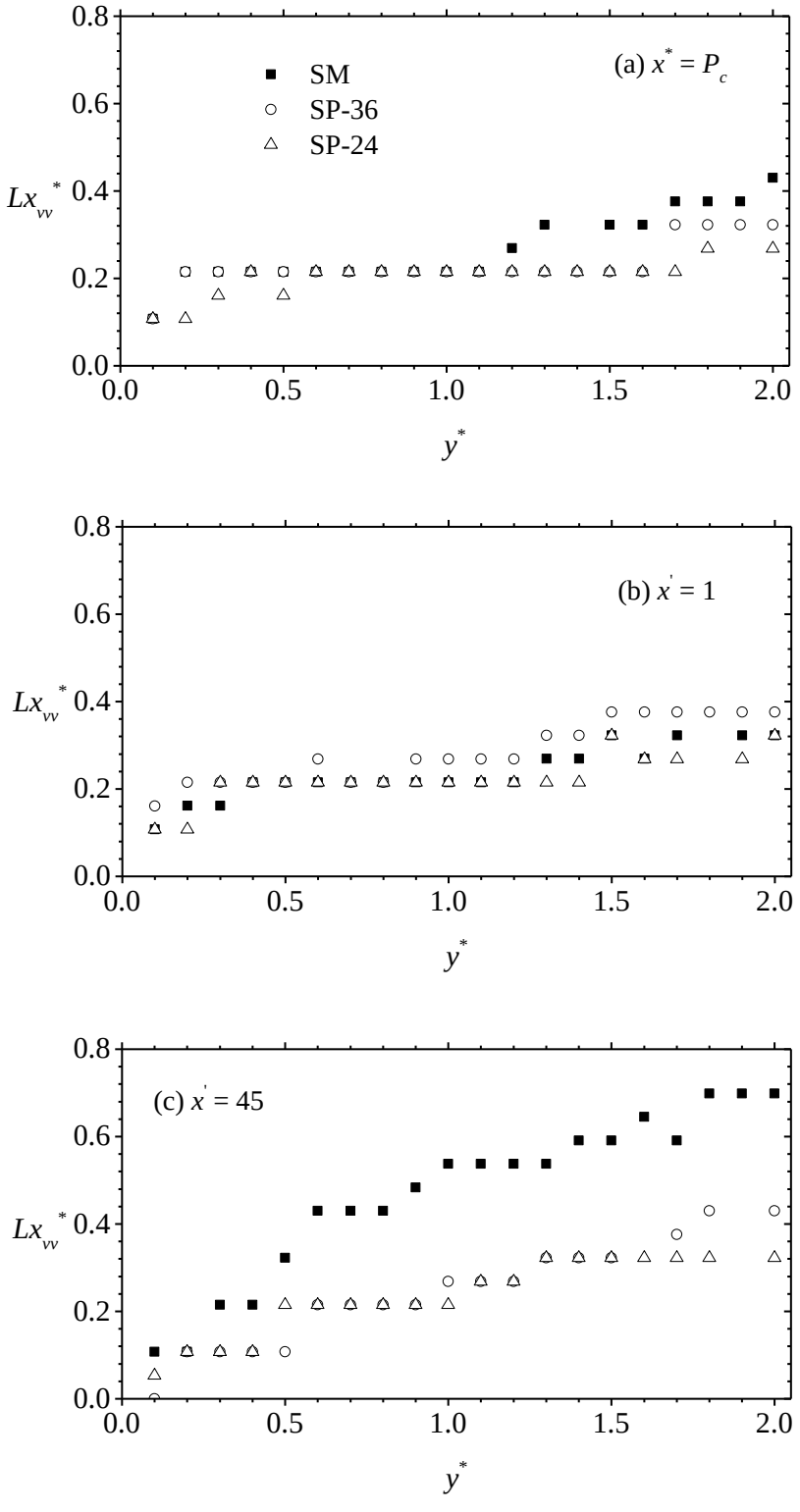

Figure 4.36: Distribution of the streamwise extents (Lx_{vv}) of the wall-normal auto-correlation function (R_{vv}) in the recirculation region (a), early redevelopment region (b) and further downstream of the redevelopment region (c) over smooth wall (SM), sandpaper 36 grit (SP-36) and sandpaper 24 grit (SP-24).

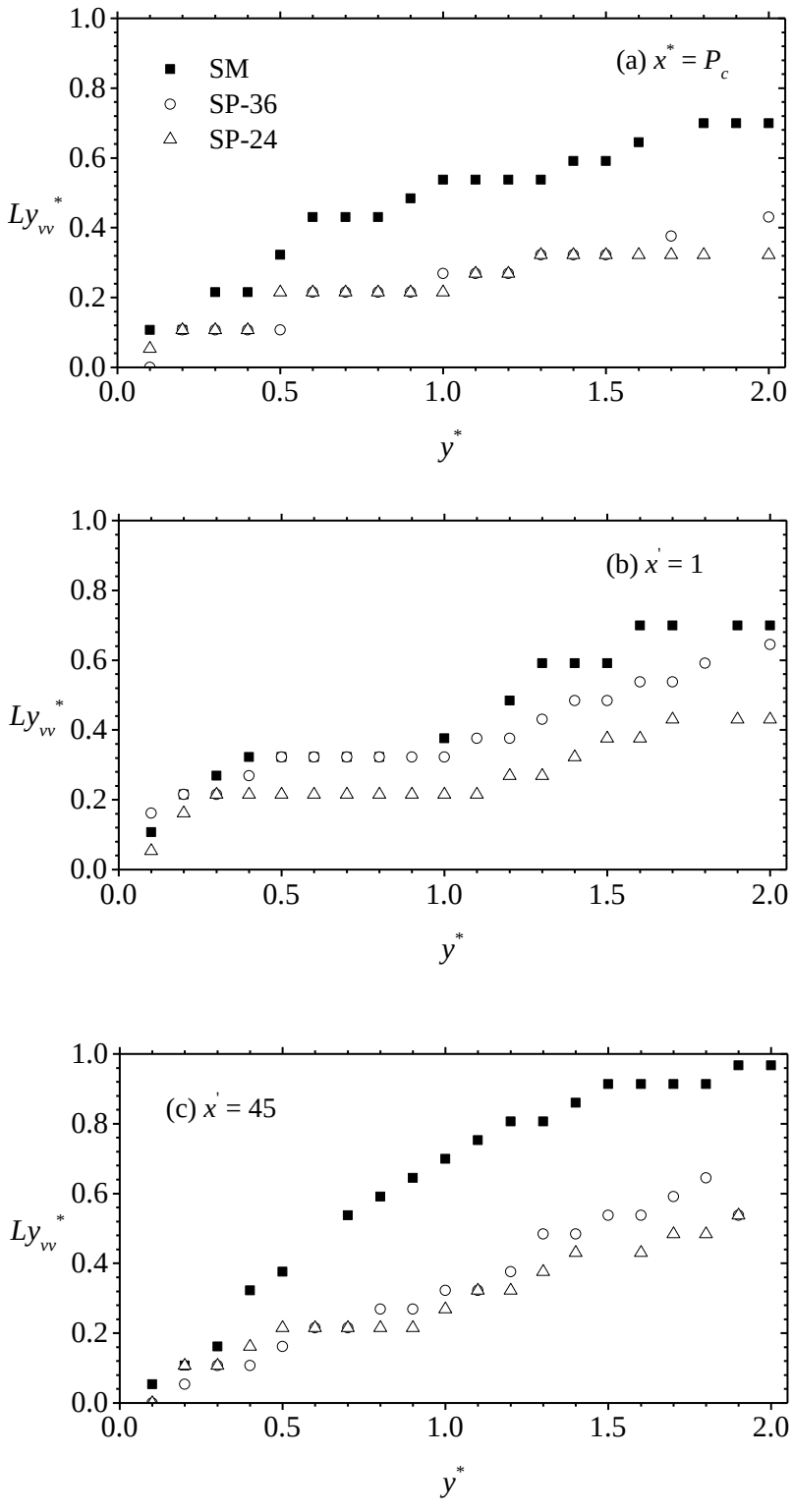

Figure 4.37: Distribution of the wall-normal extents (Ly_{vv}) of the wall-normal auto-correlation function (R_{vv}) in the recirculation region (a), early redevelopment region (b) and further downstream of the redevelopment region (c) over smooth wall (SM), sandpaper 36 grit (SP-36) and sandpaper 24 grit (SP-24).

reported for turbulent boundary layers by Krogstad and Antonia, 1994.

The streamwise extent (Lx_{vv}) and wall-normal extent (Ly_{vv}) of the wall-normal auto-correlation function (R_{vv}) are shown in Figure 4.36 and 4.37. The values of Lx_{vv} and Ly_{vv} increase with increasing wall-normal distance away from the wall, irrespective of the wall condition and measurement location. Wall roughness significantly reduced the streamwise and wall-normal extents of the wall-normal auto-correlation function (R_{vv}) in the recirculation and redevelopment region. However, the impact of roughness on these extents is stronger further downstream of reattachment point ($x' = 45$) than in the recirculation region. For example, at one step height away from the wall, the distribution of Lx_{vv} is independent of roughness at the center of primary recirculation bubble but roughness reduced the values of Lx_{vv} by 60% at $x' = 45$. Also, at one step height way from the wall, SP-24 reduced the values of Ly_{vv} by 33% and 62% at the center of primary recirculation bubble and $x' = 45$, respectively. For each measurement location, the impact of roughness on the streamwise and wall-normal extents of the structure embodied in the wall-normal auto-correlation function increases with increasing distance away from the wall.

4.3.2 Proper orthogonal decomposition

In turbulent shear flows, dominant flow features, often referred to as coherent structures, repeatedly appear and undergo a characteristic temporal life cycle (Berkooz et al., 1993). The proper orthogonal decomposition (POD) is one of the statistical techniques for extracting these coherent structures. POD decomposes the flow using a set of basis functions which are optimal in terms of energy. This implies that the first few modes which are usually associated with the large scale structures can be used to satisfactorily capture the dominant flow structures that play dynamic roles in turbulence generation and transport. The POD also facilitates a reduced order

model which attempts to describe the flow using only the largest and most energetic scales. The POD analysis was first used to identify coherent structures in turbulent shear flows by Lumley, 1967.

In the present study, the snapshot approach proposed by Sirovich, 1987 and described in detail by Meyer et al., 2007 is implemented. In this method, each instantaneous PIV data is considered a snapshot of the flow. The total number of snapshots is denoted by N while the total number of vectors in each velocity field (snapshot) is denoted by M. The POD analysis is performed on the fluctuating part of the velocity components (u_j^n, v_j^n), where the index n runs through the N snapshots and j runs through the M positions of velocity vectors in a given snapshot (i.e. $u_j = u(x_j, y_j)$). All the fluctuating velocity components from the N snapshots are arranged in a matrix U, and the $N \times N$ auto-covariance matrix is obtained from $C = U^T U$. A set of N eigenvalues, λ^i, and a corresponding set of orthonormal eigenvectors, A^i which satisfy $CA^i = \lambda^i A^i$ are evaluated from the auto-covariance matrix, where i spans from 1 to N. The eigenvalues are then ordered by decreasing value as follows: $\lambda^1 > \lambda^2 > \ldots > \lambda^N > 0$. The normalized eigenfunction or POD modes (ϕ^i) are constructed from the projection of the eigenvectors on the original fields as follows:

$$\emptyset^i = \sum_{n=1}^{N} A_n^1 \, u^n \; / \; \| \sum_{n=1}^{N} A_n^1 \, u^n \|, \;\; i = 1, \ldots, N \qquad (4.2)$$

where A_n^i is the nth component of the eigenvector corresponding to λ^i and $\| \, . \, \|$ is the L_2-norm. The expansion or POD coefficients, a_i, of each mode were calculated by projecting the data set corresponding to the fluctuating part of the velocity onto the calculated POD modes: $a^n = \Psi^T u^n$ where, $\Psi = [\phi^1 \; \phi^2 \; \ldots \; \phi^N]$. The expansion of the fluctuating part of a snapshot n is obtained from:

$$u^n = \sum_{i=1}^{N} a_i^n \emptyset^i = \Psi a^n \quad (4.3)$$

Equation 4.3 gives the best approximation of the data ensemble in the sense that the average least-squares truncation error is a minimum for any given number $m \leq N$ of basis functions over all possible sets of orthogonal basis functions. The ensemble-averaged energy of the fluctuating component is given by the sum of all the eigenvalues:

$$E = \sum_{i=1}^{N} \lambda^i \quad (4.4)$$

It should be noted that the spatial eigenfunction represents a typical dynamical structure, while the corresponding eigenvalue represents the portion of energy associated with it.

The number of snapshots required to adequately capture the energy content for a given POD mode depends on the complexity of the flow. As the number of snapshots increases, the computed energy spectra approaches the analytical spectra and the fidelity of the results improves (Breuer and Sirovich, 1991).

4.3.2.1 Implementation of POD and convergence test

An energy convergence test was performed to verify that the N = 6000 sample size or snapshots acquired in each measurement plane was adequate to perform the POD analysis. Each snapshot was trimmed to an equivalent area of 6.2 h × 3 h in the x-y directions and the fractional energy associated with the most dominant mode, mode 1 ($\lambda_1/\Sigma\lambda$) was computed from an increasing number of snapshots. The POD analysis was performed on the velocity data obtained in the upstream region (P0), recirculation region (P1), and two planes within the redevelopment region (P2 and P5) over the smooth wall (SM) and sandpaper grit 24 rough wall (SP-24). Table 4.6 demonstrates

Table 4.6: Energy convergence for increasing number of snapshots (N) of the first mode, $\lambda_1^* = \lambda_1/\Sigma\lambda\%$.

	PO	SM- P1	SP-24- P1	SM- P2	SP-24 - P2	SM- P5	SP-24- P5
10	25.8	18.8	17.5	25.1	20.0	24.9	32.2
50	13.9	11.7	8.7	15.1	15.6	17.4	18.8
100	13.1	11.6	6.8	14.8	15.4	17.2	16.1
250	12.8	10.3	7.1	14.8	14.5	16.6	14.8
500	13.8	9.6	7.1	14.7	13.6	16.6	15.7
1000	14.0	8.9	7.3	14.8	12.6	17.6	17.1
2000	14.1	9.0	7.3	15.1	12.3	17.0	17.6
4000	14.2	9.0	7.4	14.7	12.1	17.3	17.3
6000	13.9	8.9	7.3	14.7	12.1	17.4	17.6

that the fractional energy contribution of the most dominant mode ($\lambda_1/\Sigma\lambda$) decreases as the number of snapshots increases until a threshold number is reached beyond which the variation in energy among successive number of snapshots is negligible. In the upstream region, beyond $N = 50$, $\lambda_1/\Sigma\lambda = 13.7 \pm 0.5$. In the recirculation region, beyond $N = 500$, $\lambda_1/\Sigma\lambda = 9.1 \pm 0.3$ over the smooth wall whereas over the rough wall, $\lambda_1/\Sigma\lambda = 7.2 \pm 0.2$ for $N \geq 250$. The distribution of $\lambda_1/\Sigma\lambda$ in the early redevelopment region (P2) shows that beyond $N = 50$, $\lambda_1/\Sigma\lambda = 14.9 \pm 0.2$ over the smooth wall and $\lambda_1/\Sigma\lambda = 12.3 \pm 0.2$ for $N \geq 1000$ over the rough wall. At the later stage of the redevelopment region (P5), $\lambda_1/\Sigma\lambda = 17.3 \pm 0.4$ for $N \geq 50$ over the smooth wall and $\lambda_1/\Sigma\lambda = 17.4 \pm 0.2$ for $N \geq 1000$ over the rough wall. For all the measurement planes, the variation in $\lambda_1/\Sigma\lambda$ is less than 1% when $N > 500$ snapshots are used. This implies that the 6000 snapshots acquired in each measurement plane are sufficient to perform the POD analysis.

The 6000 snapshots used in the present study are comparable to those used in previous POD studies. For example, Kostas et al., 2005 used 1024 snapshots to preform POD analysis downstream of a backward facing step. Shah and Tachie, 2009

used 2040 snapshots to conduct POD analysis in separated and reattached flow over a rib. In smooth and rough wall turbulent boundary layer studies, Alfonsi and Primavera, 2007 and Sen et al., 2007 used 2000 and 6000 snapshots, respectively, to perform POD analysis.

Table 4.6 demonstrates that the value of $\lambda_1/\Sigma\lambda$ computed from N = 6000 snapshots is larger in the upstream region than in the recirculation region. For example, the value of $\lambda_1/\Sigma\lambda$ over the smooth wall (SM-P1) is 57% smaller than the corresponding value in the upstream region. However, the value of $\lambda_1/\Sigma\lambda$ over the smooth and rough walls monotonically increases as the flow evolves further downstream of reattachment point. The value of $\lambda_1/\Sigma\lambda$ at the later stage of the redevelopment region (P5) over the smooth wall, for example, is 25% and 97% larger than the corresponding value in the upstream and recirculation regions, respectively. The progressive increment of the value of $\lambda_1/\Sigma\lambda$ as the flow evolves from the recirculation region through the redevelopment region was also reported by Kostas et al., 2005 and Shah and Tachie, 2009.

The reduced energy content of the most dominate mode in the recirculation region has been attributed to the complexity of the flow structures in the recirculation region which causes a more uniform distribution of the energy among the various modes. In the recirculation and early redevelopment region, the additional flow structural complexity induced by the rough wall reduced the value of $\lambda_1/\Sigma\lambda$ by 22% compared with corresponding value over the smooth wall. The effect of roughness on the most dominant mode was, however, not significant at the later stage of flow redevelopment.

4.3.2.2 Energy Spectra

The spectra of fractional and cumulative energy contributions of the first 50 modes of the measurement plane of the recirculation region (P1) and redevelopment region (P5) over the smooth and rough walls are plotted in Figure 4.38. As expected, the fractional energy associated with the modes decreases exponentially with increasing mode. In each measurement plane, after the first 14 modes, the energy content of successive modes is less than 1% for both wall conditions. The decay rate of energy

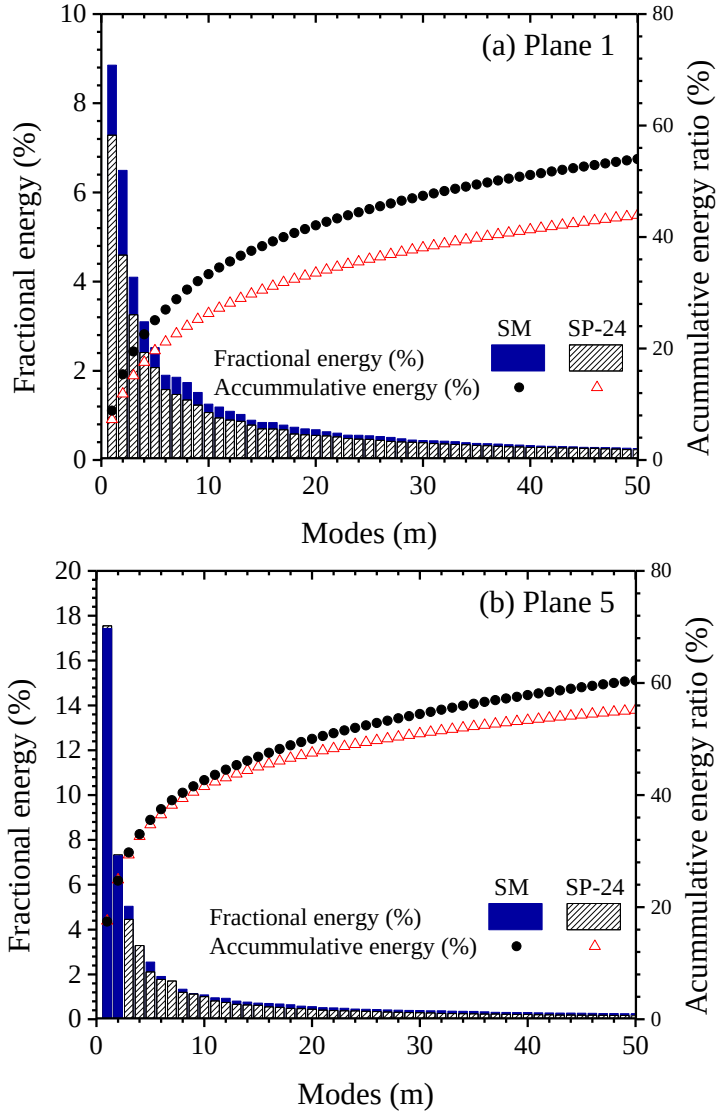

Figure 4.38: Fractional and cumulative energy spectra in recirculation region (plane 1) and further downstream of the redevelopment region (plane 5) over the smooth wall (SM) and sandpaper 24 grit (SP-24)

content for increasing mode number is more rapid over the smooth wall compared to the rough wall. The cumulative energy spectra show that the majority of the total energy over the rough wall is captured by a larger number of modes as compared to that over the smooth wall. In the recirculation region, 50% and 90% of the total energy over the rough wall is captured by the first 83 and 1575 modes, respectively, while only 37 and 1038 modes are required to capture 50% and 90% of the total energy over the smooth wall. At the later stage of the redevelopment region, the first 27 and 1750 modes over the rough wall and 20 and 890 modes over the smooth wall contribute to 50% and 90% of the total energy, respectively.

4.3.2.3 Eigenfunctions and Reconstruction

The eigenvectors are thought to represent the spatial shape of the coherent structures, and have the same boundary conditions as the velocity field (Reichert et al., 1994). The eigenvectors may not correspond to the instantaneous structures since the POD structures are defined over an ensemble. However, vector plots of the eigenfunctions can be used to reveal some spatial flow features of the coherent structures embodied in the dominant POD modes. Detailed analysis of the spatial flow features was performed in the recirculation region (P1) and redevelopment region (P5) over the smooth and rough walls.

The vector plots of the eigenfunctions of POD mode 1, 2, 3, 5 and 10 in the recirculation and redevelopment regions are plotted in Figure 4.39 and 4.40, respectively. The mean dividing streamline is shown on the plots in the recirculation region. In each plot, curved arrows are used to facilitate visualization of the rotational direction of the structures. The angle of inclination of some structures is demarcated by a dashed line. The vector plots reveal distinct clockwise and counter-clockwise

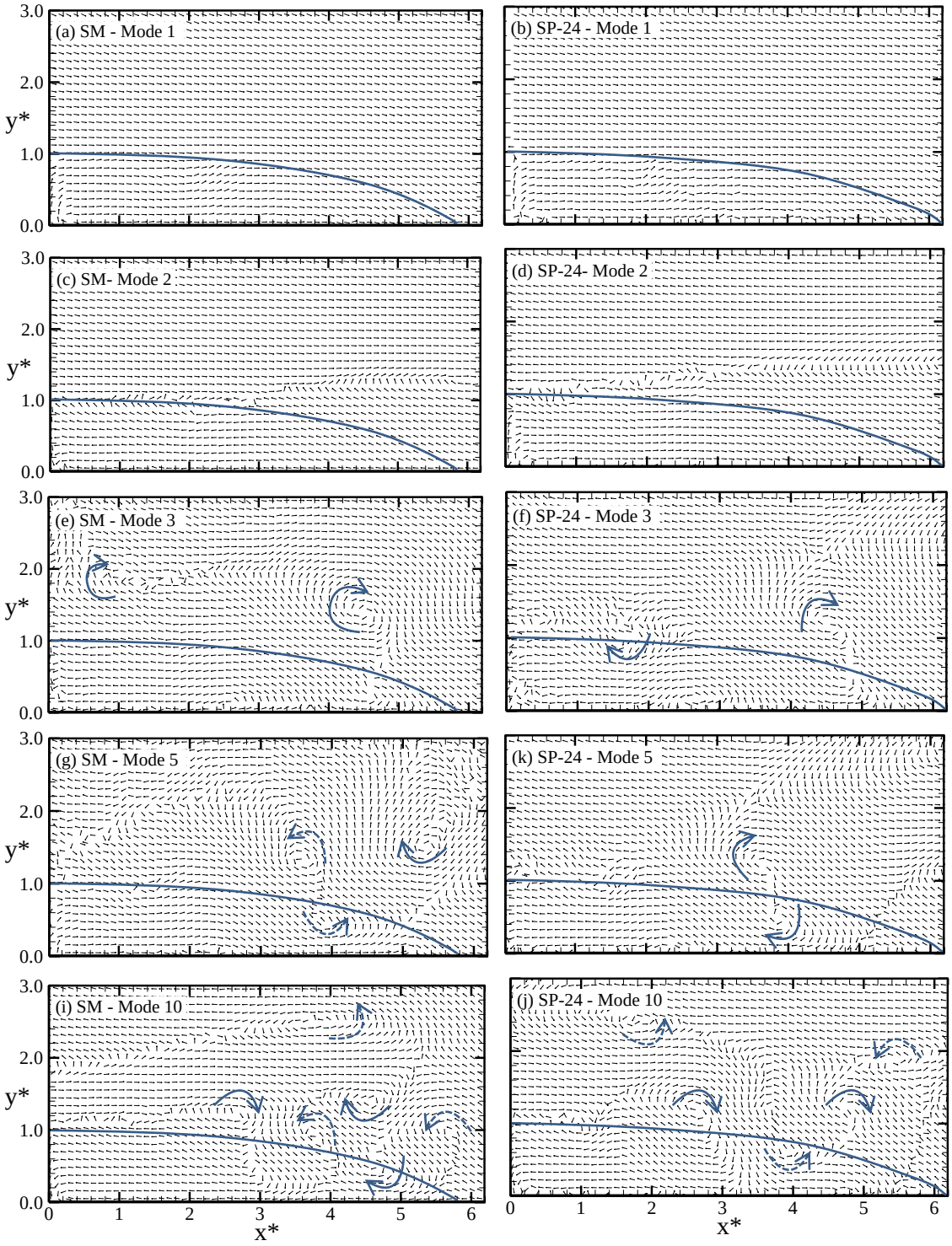

Figure 4.39: Vector plots of the eigenfunction of POD mode 1, 2, 3, 5 and 10 in the recirculation region over smooth wall, SM (a, c, e, g, i) and sandpaper 24 grit, SP-24 (b, d, f, h, j).

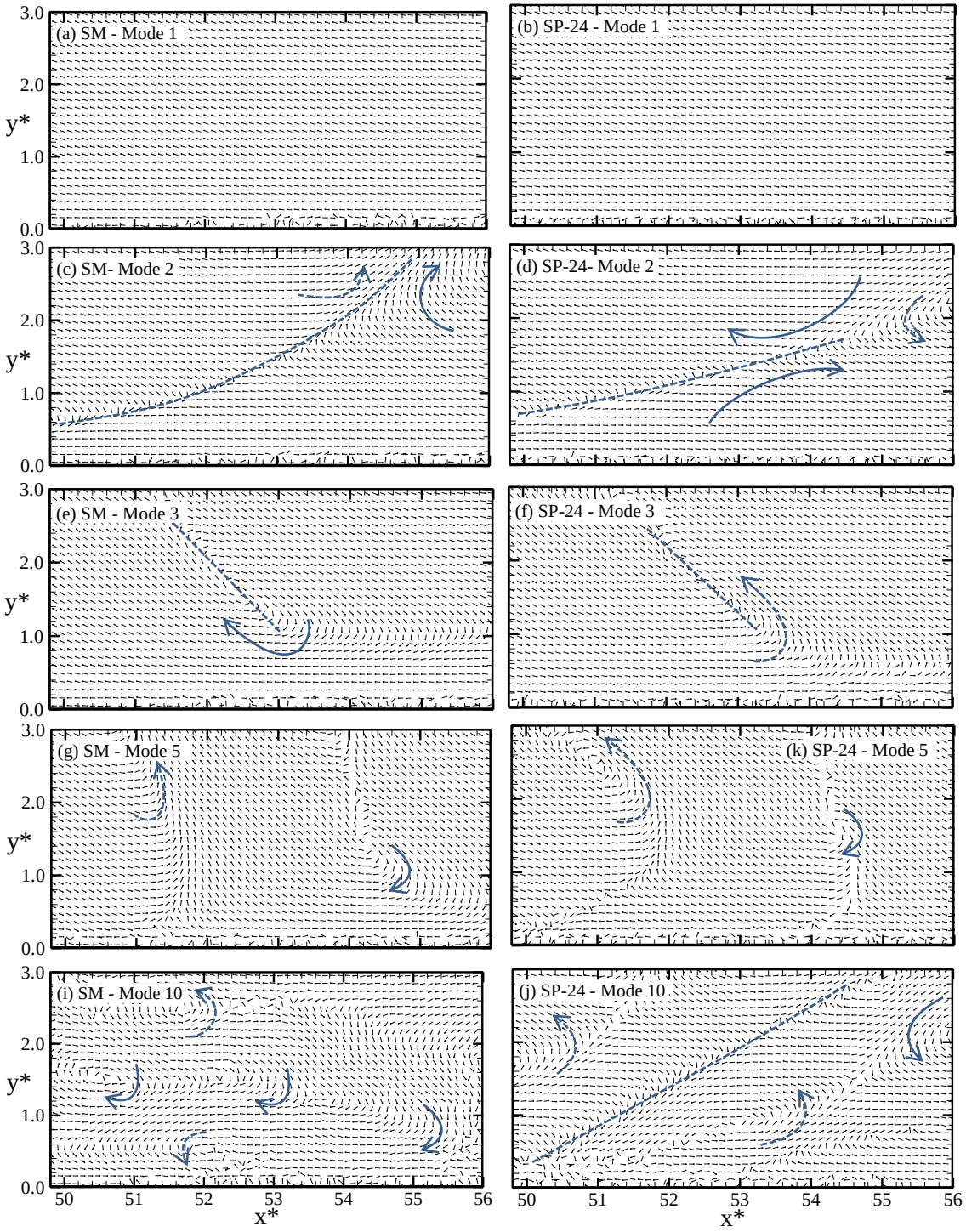

Figure 4.40: Vector plots of eigenfunction of POD mode 1, 2, 3, 5 and 10 obtained further downstream of the redevelopment region over smooth wall, SM (a, c, e, g, i) and sandpaper 24 grit, SP-24 (b, d, f, h, j).

rotating structures in the recirculation and redevelopment regions over both wall conditions. In the recirculation region, the spatial distributions of the rotating structures found in mode 1, 2 and 3 are qualitatively similar over both wall conditions. For example, mode 3 of both wall conditions reveal two clockwise rotating structures. Modes 5 and 10 on the other hand, show significant differences between the spatial distributions of the structures over the smooth and rough walls. Irrespective of the wall condition, the number of rotating structures increases and the structures move closer for wall as mode number increases. For example, two clockwise rotating structures are observed in mode 3 over the smooth wall but mode 10 reveals six (i.e. three clockwise and three anticlockwise) rotating structures.

In the redevelopment region, the size of the spatial structures for both smooth and rough walls reduces as the mode number increases. The spatial distribution of the structures over the smooth and rough walls is qualitatively similar for mode 1, 2, 3, and 5. For example, mode 3 reveals a large clockwise rotating structure backwardly inclined at about 45° over the smooth wall and in the case of the rough wall this structure rotates anticlockwise and is also backwardly inclined at about 41°. The rotating structures in mode 10 are fewer and larger over the rough wall than observed over the smooth wall. Irrespective of the wall condition, the sizes of the spatial structures are larger within the redevelopment region than the recirculation region.

Low-order representations of the instantaneous velocity fields in the recirculation and redevelopment region over the smooth and rough walls were reconstructed with the POD modes and the corresponding turbulent statistics were computed from the reconstructed velocity fields. Contour plots of cumulative turbulent kinetic energy obtained from the first 1, 5 and the respective number of modes that contribute to 50%

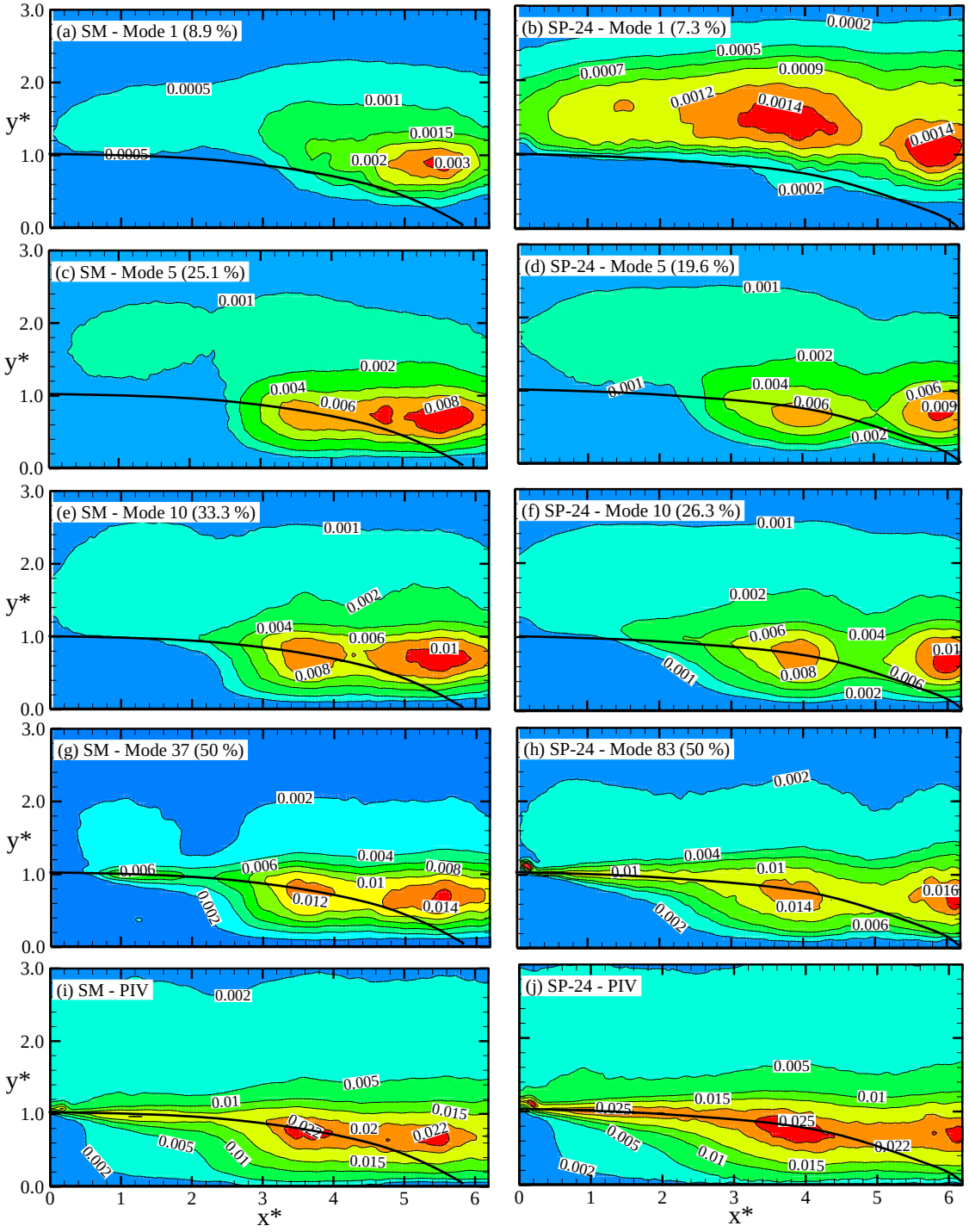

Figure 4.41: Contour plots of dimensionless cumulative turbulent kinetic energy in the recirculation region over smooth wall, SM (a, c, e, g, i) and sandpaper 24 grit, SP-24 (b, d, f, h, j).

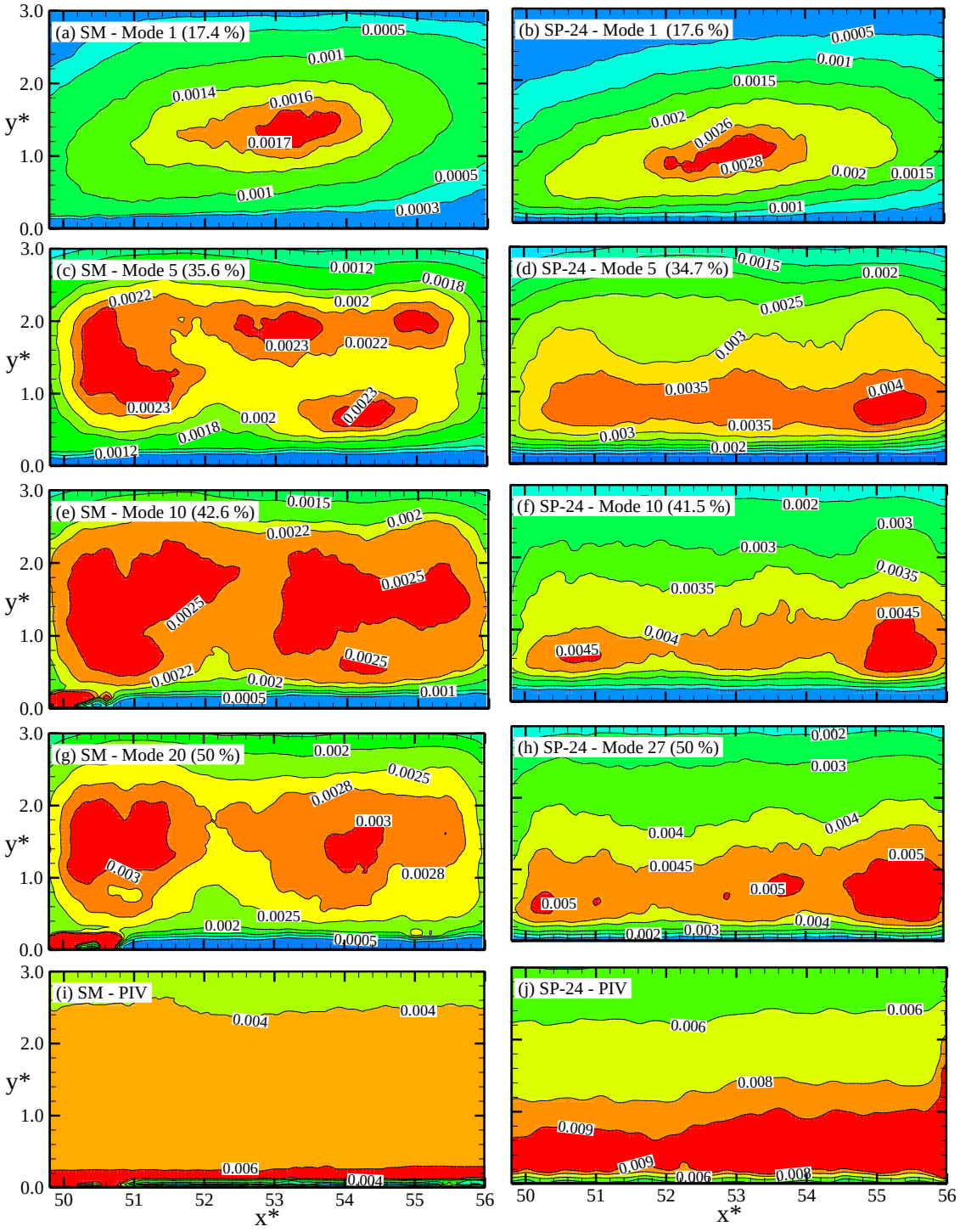

Figure 4.42: Contour plots of dimensionless cumulative turbulent kinetic energy obtained further downstream of the redevelopment region over smooth wall, SM (a, c, e, g, i) and sandpaper 24 grit, SP-24 (b, d, f, h, j).

of the total turbulent kinetic energy in the recirculation and redevelopment regions are shown in Figure 4.41 and 4.42, respectively. It should be recalled that the first 37 and 83 modes contribute to 50% of the total turbulent kinetic energy in the recirculation region over smooth and rough walls, respectively and the corresponding number of modes in the redevelopment region are 20 and 27, respectively. The corresponding contours of the turbulent kinetic energy obtained from the ensemble-averaged PIV data are added to each figure for comparison. In each plot, the percentage of cumulative energy contribution of the corresponding modes is shown. The mean dividing streamline is also shown on the plots in the recirculation region. Irrespective of the wall condition and measurement plane, the contour plots of the cumulative turbulent kinetic energy show a systematic increase in intensity as the number of modes used for the reconstruction increases. Furthermore, the distributions of the turbulent kinetic energy gradually converge towards that of the PIV data as the number of modes increases. This observation is in agreement with results reported by Shah and Tachie, 2009 and Kostas et al., 2002.

It can be observed from Figure 4.41 that the contours of the reconstructed turbulent kinetic energy in the recirculation region over the smooth wall are qualitatively similar to the corresponding contours over the rough wall. For each wall condition, the intense energy zones observed in mode 1 are above the mean dividing streamline. As the number of modes increases, the intense energy zones moves closer to the region of the wall prior to the reattachment point ($3 \leq x^* \geq 6.2$). After the first 5 modes, the locations of the maximum turbulent kinetic energy observed in the PIV contours within the region $3 \leq x^* \geq 6.2$ over each wall condition are already defined and additional modes only increase the peak values towards the corresponding peak values of the PIV contours. However, the peak of the turbulent kinetic energy

observed at the early region of the separated shear layer ($x^* < 2$) in the PIV contour is not noticeable in the contours of the first 1, 5 and 10 modes over each wall conditions.

In the redevelopment region (Figure 4.41), the turbulent kinetic energy obtained from the most dominant mode (mode 1) over the smooth and rough walls are qualitatively similar. For example, the contours of mode 1 of each wall condition are inclined at an angle and the intense energy zone is located about mid-way of the measurement plane ($x^* = 53$). The angle of inclination of the mode 1 contour is about 9° and 10° over the smooth and rough walls, respectively. As the number of modes increases, significant disparities in the distributions of the contours over the smooth and rough walls become noticeable. For example, the first 5, 10 and 20 modes over the smooth wall reveal multiple intense energy zones which are mostly located away from the wall. On the contrary, the intense energy zones of the first 5, 10 and 27 modes are closer to the rough wall and located downstream of the measurement plane. The difference in the topography of the contour of the modes that contribute 50% of the total kinetic energy and the PIV contour is less significant over the rough wall as compared to the smooth wall.

Profiles of the Reynolds stresses obtained from the reconstructed velocity field using mode 1, 3, 5 and the respective number of modes that contribute to 50% and 90% of the total turbulent kinetic energy in the recirculation and redevelopment region over the smooth and rough walls are used to quantitatively examine the cumulative effect of using increasingly more modes for reconstruction of the turbulence statistics. The profiles shown in Figure 4.43 and 4.44 were obtained at $x^* = P_c$ (in the recirculation region) and $x' = 45$ (in the redevelopment region), respectively. The corresponding profiles from the ensemble-averaged PIV data are included in each plot for

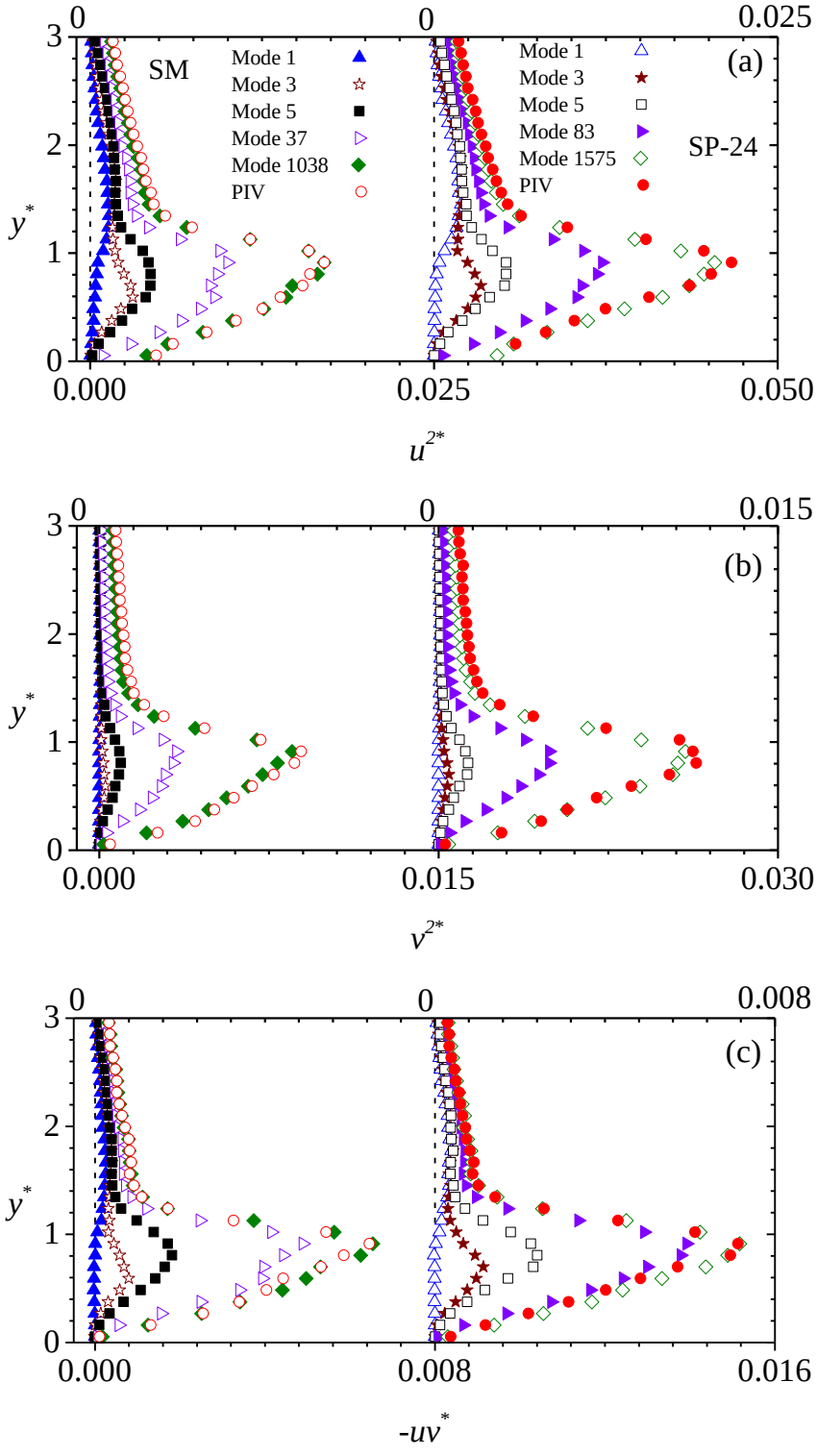

Figure 4.43: Profiles of dimensionless reconstructed streamwise, u^{2*} (a) and wall-normal, v^{2*} (b) Reynolds normal stress and Reynolds shear stress, $-uv^*$ (c) at $x^* = P_c$ over smooth wall (SM) and sand paper 24 grit (SP-24).

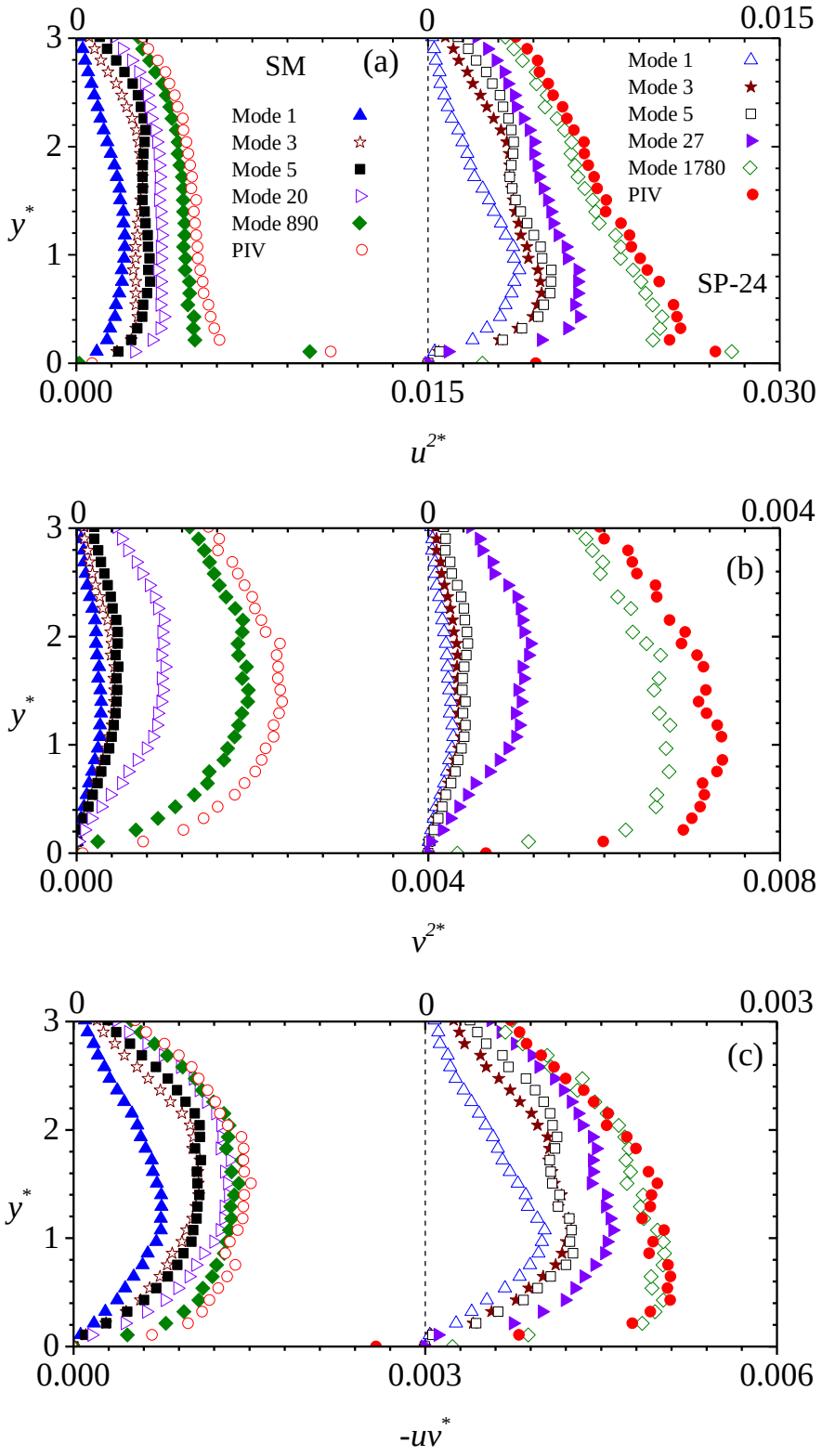

Figure 4.44: Profiles of dimensionless reconstructed streamwise, u^{2*} (a) and wall-normal, v^{2*} (b) Reynolds normal stress and Reynolds shear stress, $-uv^*$ (c) at $x' = 45$ over smooth wall (SM) and sand paper 24 grit (SP-24).

comparison. It should be recalled that the first 20 and 27 modes contribute to 90% of the total turbulent kinetic energy in the recirculation region over smooth and rough walls, respectively and the corresponding number of modes in the redevelopment region are 890 and 1780.

Similar to the contour plots of the turbulent kinetic energy, the peak of the profiles of mode 1 of the Reynolds stresses in the recirculation region are location above one step height. For example, the peak of mode 1 of the streamwise Reynolds normal stress is located at about 1.4 step heights way from the smooth and rough walls. As the number of modes increases, the profiles of reconstructed Reynolds stresses over each wall condition show a consistent progression of level to that of the corresponding PIV profile. For each wall condition, the distinct peaks of the streamwise Reynolds normal stress and Reynolds shear stress in the recirculation region are noticeable after the first mode. In the case of the wall-normal Reynolds normal stress, the distinct peak is noticeable after the first 3 modes over each wall condition. Similar to the distributions of the Reynolds stresses observed in Section 4.2.2, the levels of the Reynolds stresses of the first few modes (1, 3 and 5) are larger over the rough wall than the smooth wall. For example, the peak of the streamwise and wall-normal Reynolds normal stresses and Reynolds shear stress obtained from the first 5 modes over the rough wall is 20%, 37% and 33%, respectively, larger than corresponding values over the smooth wall.

Figure 4.44 demonstrates that the profiles of the reconstructed Reynolds stresses in the redevelopment region converge towards the corresponding PIV profile faster over the smooth wall as compared to the rough wall. This is an indication that, similar to the turbulent kinetic energy; less number of modes are required to reconstruct the Reynolds stresses over the smooth wall compared to the rough wall.

The levels of profiles of the first 1, 3, and 5 modes of the reconstructed Reynolds stresses are also larger over the rough wall than the smooth wall. At one step height from the wall, for example, roughness increased the level of the streamwise and wall-normal Reynolds normal stress and the Reynolds shear stress obtained from the first 5 modes by 53%, 2% and 25%, respectively, compared to corresponding values over the smooth wall. The effects of roughness on the Reynolds stresses reconstructed from the first few modes (1, 3 and 5) are more significant on the streamwise Reynolds normal stress and the Reynolds shear stress than the wall-normal Reynolds normal stress, in agreement to the effects of roughness on the Reynolds stresses in the redevelopment region observed in Section 4.2.2.

CHAPTER 5

SUMMARY AND CONCLUSIONS

5.1 Summary

An experimental study was conducted to investigate the effect of wall roughness on separated and reattached turbulent shear flow downstream of a backward facing step (BFS). Detailed velocity measurements were conducted over three wall conditions; a reference smooth made from a clear acrylic plate and rough walls produced from sandpaper 36 and 24 grit positioned downstream of a BFS, one after another. A particle image velocimetry (PIV) system was used to perform the velocity measurements. Each of the three sets of experiments was conducted at the same Reynolds number based on the step height and the centerline mean velocity, Re_h = 7050. The velocity data over the three wall conditions were post-processed to obtain the mean velocities, Reynolds stresses, turbulent kinetic energy, Reynolds stress ratio, Townsend's structure parameter, triple velocity correlations and the production term of the turbulent kinetic energy transport equation. These statistics were compared to evaluate roughness effects on the flow characteristics. Two-point correlation functions and proper orthogonal decomposition were also applied to reveal coherent structures within the flow fields, and to investigate the impact of wall roughness on the large scale structures.

5.2 Conclusions

The major conclusions are summarized as follows

- Wall roughness increased the reattachment length over sandpaper 36 and 24 grits by 5% and 7%, respectively, compared with corresponding value over the reference smooth wall.

- The mean velocity distributions in the recirculation region were independent of wall roughness. Further downstream of reattachment, wall roughness reduced the level of the streamwise mean velocity but increased the level of the wall-normal mean velocity in the region adjacent to the rough walls.
- Wall roughness enhanced the levels of the Reynolds stresses, turbulent kinetic energy and turbulent production in both the recirculation and redevelopment region.
- The Reynolds stress ratios showed that the flow is anisotropic in both the recirculation and redevelopment region but due to the enhanced mixing in the wall-normal direction in the recirculation region, departure from isotropy is less dramatic in the recirculation region compared to the redevelopment region. The degree of large scale anisotropy was independent of wall roughness
- The triple velocity correlations gave the indication that transport of turbulent kinetic energy is intense in the region prior to reattachment and the early region of redevelopment over the smooth and rough walls. The triple velocity correlations did not reveal any significant roughness effect.
- Wall roughness reduced the streamwise and wall-normal extents of the two-point auto-correlation functions in the recirculation and redevelopment regions.
- The results of the proper orthogonal decomposition analysis indicated that the most dominant flow structures are more energetic in the redevelopment region than in the recirculation region. Also, a larger number of modes is required to reconstruct the velocity field over the rough wall compared to the smooth wall.

- Wall roughness increased the levels of the Reynolds stresses obtained from the first few dominant modes in both the recirculation and redevelopment regions.

5.3 Future work

It is recommended that detailed velocity measurements should be conducted over various types of roughness elements to confirm the universality of the present findings. Future work should measure the third velocity component using a stereo-PIV, for example, since this will provide a complete description of the effect of roughness on the flow dynamics.

REFERENCES

Abe, H., Kawamura, H., Matsuo, Y., 2001. Direct Numerical Simulation of a Fully Developed Turbulent Channel Flow With Respect to the Reynolds Number Dependence. J. Fluids Eng. 123, 382–393.

Adams, E.W., Johnston, J.P., 1988. Effects of the separating shear layer on the reattachment flow structure. Part 2: Reattachment length and wall shear stress. Exp. Fluids 6, 493–499.

Adams, E.W., Johnston, J.P., 1988. Effects of the separating shear layer on the reattachment flow structure. Part 1: Pressure and turbulence quantities. Exp. Fluids 6, 400–408.

Adrian, R.J., Westerweel, J., 2010. Particle image velocimetry. Cambridge Univ. Press 30.

Alfonsi, G., Primavera, L., 2007. Dynamics of POD modes in wall bounded turbulent flows. Proc. R. Soc. London 463, 593–612.

Ampadu-Mintah, A.A., Tachie, M.F., Agelin-Chaab, M., 2012. Roughness effects on separated and reattached open channel turbulent flow, in: Turbulence, Heat and Mass Transfer 7. Palermo, Sicily, Italy, pp. 1–12.

Armaly, B.F., Durst, F., Pereira, J.C.F., Schonung, B., Armalyt, B.B.F., Dursts, F., 1983. Experimental and theoretical investigation of backward-facing step flow. J. Fluid Mech 127, 473–496.

Berkooz, G., Holmes, P., Lumley, J.L., 1993. The proper orthogonal decomposition in the analysis of turbulent flows. Annu. Rev. Fluid Mech. 25, 539–575.

Bradshaw, P., Wong, F., 1972. The reattachment and relaxation of a turbulent shear layer. J. Fluid Mech. 52, 113–135.

Breuer, K.S., Sirovich, L., 1991. The use of Karhunen-Loève procedure for the calculation of linear eigenfunctions. J. Comput. Phys. 96, 277–296.

Christensen, K.T., Wu, Y., 2005. Characteristics of vortex organization in the outer layer of wall turbulence, in: Proceedings of Fourth International Symposium on Turbulence and Shear Flow Phenomena, 3. Williamsburg, Virginia, pp. 1025–1030.

Coleman, H., Steele, W., 1995. Engineering application of experimental uncertainty analysis. AIAA J. 33, 1888–1895.

Dantec Dynamics 2013. DynamicStudio users guide.

De Brederode, V., Bradshaw, P., 1972. Three-dimensional flow in nominally two-dimensional separation bubbles: flow behind a rearward-facing step. Imp. Coll. Aeronaut. Rep. 72–19.

Driver, D.M., Seegmiller, H.L., 1985. Features of a reattaching turbulent shear layer in divergent channel flow. AIAA J. 23, 163–171.

Driver, D.M., Seegmiller, H.L., Marvin, J.G., 1987. Time-dependent behavior of a reattaching shear layer. AIAA J. 25, 914–919.

Durst, F., Fischer, M., Jovanovic, J., Kikura, H., 1998. Methods to set up and investigate low Reynolds number, fully developed turbulent plane channel flows. J. Fluids Eng. 120, 496–503.

Durst, F., Tropea, C., 1981. Turbulent backward-facing step flows in two-dimensional ducts and channels, in: In Proc. Third Intl Symp. on Turbulent Shear Flows. University of California, Davis, pp. 18.1–18.5.

Eaton, J.K., Johnston, J.P., 1981. A review of research on subsonic turbulent flow reattachment. AIAA J. 19, 1093–1100.

Flack, K.A., Schultz, M.P., 2010. Review of Hydraulic Roughness Scales in the Fully Rough Regime. J. Fluids Eng. 132, 041203–10.

Forliti, D.J., Strykowski, P.J., Debatin, K., 2000. Bias and precision errors of digital particle image velocimetry. Exp. Fluids 28, 436–447.

Isomoto, K., Honami, S., 1989. The effect of inlet turbulence intensity on the reattachment process over a backward-facing step. J. Fluids Eng. 111, 87–92.

Johansson, A., Alfredsson, P., 1983. Effects of imperfect spatial resolution on measurements of wall-bounded turbulentbx shear flows. J. Fluid Mech. 137, 409–421.

Jovic, S., Driver, D., 1995. Reynolds number effect on the skin friction in separated flows behind a backward-facing step. Exp. Fluids 18, 464–467.

Kasagi, N., Matsunaga, A., 1995. Three-dimensional particle-tracking velocimetry measurement of turbulence statistics and energy budget in a backward-facing step flow. Int. J. Heat Fluid Flow 16, 477–485.

Keane, R.D., Adrian, R.J., 1992. Theory of cross-correlation analysis of PIV images. Appl. Sci. Res. 49, 191–215.

Kim, B.N., Chung, M.K., 1995. Experimental study of roughness effects on the separated flow over a backward-facing step. AIAA J. 33, 159–160.

Kostas, J., Soria, J., Chong, M.S., 2002. Particle image velocimetry measurements of a backward-facing step flow. Exp. Fluids 33, 838–853.

Kostas, J., Soria, J., Chong, M.S., 2005. A comparison between snapshot POD analysis of PIV velocity and vorticity data. Exp. Fluids 38, 146–160.

Krogstad, P., Antonia, R., 1994. Structure of turbulent boundary layers on smooth and rough walls. J. Fluid Mech. 277, 1–21.

Krogstad, P.-Å., Antonia, R.A., Krogstadt, P.-Å., 1999. Surface roughness effects in turbulent boundary layers. Exp. Fluids 27, 450–460.

Le, H., Moin, P., Kim, J., Engineering, N., 1997. Direct numerical simulation of turbulent flow over a backward-facing step. J. Fluid Mech. 330, 349–374.

Lumley, J.L., 1967. The structure ofiInhomogeneous turbulent flow, in: In Atmospheric Turbulence and Radio Wave Propagation (ed. A. M. Yaglon & V. I. Tatarski). Nauka, Moscow, pp. 167–178.

Meyer, K.E., Pedersen, J.M., Özcan, O., 2007. A turbulent jet in crossflow analysed with proper orthogonal decomposition. J. Fluid Mech. 583, 199–227.

Millikan, C.B., 1938. A critical discussion of turbulent flows in channels and circular tubes, in: Proc. 5th Int. Congr. Appl. Mech.

Ötügen, M., 1991. Expansion ratio effects on the separated shear layer and reattachment downstream of a backward-facing step. Exp. Fluids 10, 273–280.

Piirto, M., Saarenrinne, P., Eloranta, H., Karvinen, R., 2003. Measuring turbulence energy with PIV in a backward-facing step flow. Exp. Fluids 35, 219–236.

Pope, S.S.B., 2000. Turbulent flows. Cambridge University Press.

Prasad, A., Adrian, R., Landreth, C., Offutt, P., 1992. Effect of resolution on the speed and accuracy of particle image velocimetry interrogation. Exp. Fluids 116, 105–116.

Raffel, M., Willert, C.E., Kompenhaus, J., 1998. Particle image velocimetry: A practical guide. Springer Verlag.

Reichert, R.S., Hatay, F.F., Birigen, S., Huser, A., 1994. Proper orthogonal decomposition applied to turbulent flow in a square duct. Phys. Fluids 6, 3086–3092.

Sen, M., Bhaganagar, K., Juttijudata, V., 2007. Application of proper orthogonal decomposition (POD) to investigate a turbulent boundary layer in a channel with rough walls. J. Turbul. 8, N41.

Shah, M., Tachie, M., 2009. Proper orthogonal decomposition analysis of separated and reattached pressure gradient flows. AIAA J. 47, 2616–2631.

Shah, M.K., 2008. Effects of pressure gradient on two-dimensional separated and reattached turbulent flows.

Simpson, R., 1989. Turbulent boundary-layer separation. Annu. Rev. Fluid Mech. 21, 205–234.

Sirovich, L., 1987. Turbulence and the dynamics of coherent structures. part 1: coherent structures. Q. Appl. Math. 45, 561–571.

Spalart, P., 1988. Direct simulation of a turbulent boundary layer up to Reθ= 1410. J. Fluid Mech. 187, 61–98.

Tachie, M.F., Bergstrom, D.J., Balachandar, R., 2003. Roughness effects in low- Re_θ open-channel turbulent boundary layers. Exp. Fluids 35, 338–346.

Tachie, M.F., Bergstrom, D.J., Balachandar, R., Ramachandran, S., 2001. Skin friction correlation in open channel boundary layers. J. Fluids Eng. 123, 953–956.

Troutt, T.R., Scheelke, B., Norman, T.R., 1984. Organized structures in a reattaching separated flow field. J. Fluid Mech. 143, 413–427.

Volino, R.J., Schultz, M.P., Flack, K.A., 2007. Turbulence structure in rough- and smooth-wall boundary layers. J. Fluid Mech. 592, 263–293.

Westphal, R. V., Johnston, J.P., Eaton, J.K., 1984. Experimental study of flow reattachment in a single-sided sudden expansion. PHD Thesis, Mechanical Engineering Department, Stanford University.

Willert, C., Gharib, M., 1991. Digital particle image velocimetry. Exp. Fluids 10, 181–193.

Wu, Y., Christensen, K.T., 2010. Spatial structure of a turbulent boundary layer with irregular surface roughness. J. Fluid Mech. 655, 380–418.

APPENDIX

MEASUREMENT UNCERTAINTY

A complete uncertainty analysis of the velocity measurements reported in this study is presented in this section.

A.1 Measurement error

Measurement error is the difference between an experimentally determined value and the true value. Since the true value is most often unknown, an uncertainty is used to estimate the error. In general, the total error is made up of two major components; a precision (random) component, *P* and a bias (systematic) component, *B.* An error is classified as precision if it contributes to the scatter of the data; otherwise, it is a bias error. Coleman and Steele, 1995 presented a detailed uncertainty assessment methodology following the AIAA standard and this employed in the present study. In particle image velocimetry (PIV) technique, the sources of errors may include bad selection of time between image pairs, sub-pixel displacement bias, insufficient sample size, effect of velocity gradients and spatial resolution. These uncertainties include particle response to fluid motion, light sheet positioning, light pulse timing, and the error arising from the peak-finding algorithm to determine the average particle displacement.

A.2 Minimizing errors

In the present study, precautionary measures were taken to minimize errors in the data acquisition and post processing. For example, the size and refractive index of the seeding particles were chosen such that the particles have good light scattering ability. Also the settling velocity and response time of the seeding particles were calculated and results confirmed that the particles followed the flow faithfully. The laser sheet

was carefully aligned to the centerline of the test channel to reduce any possible errors from light sheet positioning. Based on the recommendation by Willert and Gharib, 1991 the time between two successive pulses of the laser was set such that the maximum particle displacement was less than 1/4 of the interrogation area size used. The interrogation area (32 pixels × 32 pixels with 50% overlap in both the *x* and *y* directions) was chosen to be small as possible to contain sufficient number of particles and also improve spatial resolution. Although the present spatial resolution was not sufficient to resolve the smallest or Kolmogorov lengthscale, the Taylor micro-scales which contribute to the turbulent statistics reported in the present study were well resolved. Keane and Adrian, 1992 suggested the use of cross-correlation algorithm to reduce errors associated with velocity gradient. Forliti et al., 2000 reported that the evaluation bias and gradient of the evaluation bias can both be minimized effectively by using Gaussian peak-fitting algorithm. In the present study, adaptive correlation algorithm with a one-dimensional Gaussian peak-fitting function was used to determine the average particle displacement within the interrogation window to sub-pixel accuracy. The adaptive correlation algorithm is an advanced form of cross-correlation algorithm which uses a multi-pass fast Fourier transform. Precautionary measures were taken to minimize peak locking in the image processing. The particle image diameter of the present study was estimated as 1.4 pixels. Raffel et al., 1998 recommended a particle image diameter of 2.0 pixels to reduce peak locking but in practical PIV experiments this is often not possible, and particle image diameters in the range 1- 2 pixels are not unusual (DynamicStudio, 2013)The particle image diameter of the present study suggests possible peak locking but the effect was minimized by using a Gaussian low-pass filter. A large sample size; 6000 image pairs was used to reduce the precision error.

A.3 Error estimation

A complete uncertainty analysis of the PIV measurement involves identifying and quantifying both the bias and the precision errors in each part of the measurement chain.

A.3.1 Bias errors

In PIV measurements, the instantaneous velocity at a given location in an average velocity field is calculated as follows;

$$U_i = \Delta s_i L_O / \Delta t L_I \qquad \text{(A. 1)}$$

where U_i is the velocity component, Δs_i is the component of the particle displacement in the *x*-*y* directions obtained from the correlation algorithm, L_O is the width of the field of view of the camera, Δt is the time interval between laser pulses, and L_I is the width of the digital image.

The bias limit of the measured velocity is determined with a root-sum-square (RSS) of the elementary bias limits based on the sensitivity coefficients given as:

$$B_{Ui}^2 = \theta_{\Delta si}^2 B_{\Delta si}^2 + \theta_{Lo}^2 B_{Lo}^2 + \theta_{\Delta ti}^2 B_{\Delta ti}^2 + \theta_{LI}^2 B_{LI}^2 \qquad \text{(A. 2)}$$

where the sensitivity coefficients, θ_x, are defined as

$$\theta_x = \partial U_i / \partial X \qquad \text{(A. 3)}$$

where X = (Δs_i, L_O, Δs_i and L_I)

The classification of bias error sources and contribution to the bias limits for streamwise and wall-normal mean velocities were performed at the near wall region (y/h = 0.3) and the freestream (y/h = 2.0) within the recirculation region (x/h = 0.3) over the rough wall (SP-24). These regions were specifically chosen due to the presence of wide range of velocities and turbulence intensity distributions. The results

Table A.1: Bias limits of the local streamwise mean velocity (U) at x/h = 3.0 and y/h = 0.3 over the rough wall (SP-24)

Variable	**Magnitude**	B_x	θ_x	$B_x\theta_x$	$B_x\theta_x/\sum B_x\theta_x$	$(B_x\theta_x)^2$
L_O(m)	6.193E-02	5.000E-04	-1.873E+00	-9.363E-04	7.760E+00	8.767E-07
L_I (pix)	2.048E+03	5.000E-01	5.663E-05	2.831E-05	-2.346E-01	8.016E-10
Δt (s)	5.029E-04	1.000E-07	2.306E+02	2.306E-05	-1.911E-01	5.318E-10
Δs (pix)	-1.929E+00	1.271E-02	6.013E-02	7.643E-04	-6.334E+00	5.841E-07
U (m/s)	-1.160E-01					
			$\sum B_x\theta_x$	-1.207E-04	$\sum (B_x\theta_x)^2$	1.462E-06
					Bias Error	1.209E-03
					% Bias Error	1.04%

Table A.2: Bias limits of the local streamwise mean velocity (U) at x/h = 3.0 and y/h = 2.0 over the rough wall (SP-24).

Variable	**Magnitude**	B_x	θ_x	$B_x\theta_x$	$B_x\theta_x/\sum B_x\theta_x$	$(B_x\theta_x)^2$
L_O(m)	6.193E-02	5.000E-04	1.167E+01	5.833E-03	-4.834E+01	3.402E-05
L_I (pix)	2.048E+03	5.000E-01	-3.527E-04	-1.764E-04	1.462E+00	3.111E-08
Δt (s)	5.029E-04	1.000E-07	-1.437E+03	-1.437E-04	1.191E+00	2.064E-08
Δs (pix)	1.201E+01	1.271E-02	6.013E-02	7.643E-04	-6.334E+00	5.841E-07
U (m/s)	7.224E-01					
			$\sum B_x\theta_x$	6.277E-03	$\sum (B_x\theta_x)^2$	3.466E-05
					Bias Error	5.887E-03
					% Bias Error	0.08%

of the bias error analysis are shown in Table A. 1 and A.4. The bias limits of Δs and Δt were obtained from the PIV system manufacturer's specifications. The bias limit for L_O is obtained from a calibration procedure.

A.3.2 Precision error

The precision error, P, of a measured variable, X is given by

$$P_x = K\sigma / \sqrt{N} \qquad \text{(A.4)}$$

Table A.3: Bias limits of the local wall-normal mean velocity (V) at x/h = 3.0 and y/h = 0.3 over the rough wall (SP-24).

Variable	**Magnitude**	B_x	θ_x	$B_x\theta_x$	$B_x\theta_x/\sum B_x\theta_x$	$(B_x\theta_x)^2$
L_O(m)	6.193E-02	5.000E-04	1.975E-01	9.876E-05	-8.184E-01	9.753E-09
L_I (pix)	2.048E+03	5.000E-01	-5.973E-06	-2.986E-06	2.475E-02	8.918E-12
Δt (s)	5.029E-04	1.000E-07	-2.432E+01	-2.432E-06	2.016E-02	5.916E-12
Δs (pix)	2.034E-01	1.271E-02	6.013E-02	7.643E-04	-6.334E+00	5.841E-07
V (m/s)	1.223E-02					
			$\sum B_x\theta_x$	8.576E-04	$\sum (B_x\theta_x)^2$	5.939E-07
					Bias Error	7.706E-04
					% Bias Error	6.30%

Table A.4: Bias limits of the local wall-normal mean velocity (V) at x/h = 3.0 and y/h = 0.3 over the rough wall (SP-24).

Variable	**Magnitude**	B_x	θ_x	$B_x\theta_x$	$B_x\theta_x/\sum B_x\theta_x$	$(B_x\theta_x)^2$
L_O(m)	6.193E-02	5.000E-04	-3.549E-01	-1.775E-04	1.471E+00	3.149E-08
L_I (pix)	2.048E+03	5.000E-01	1.073E-05	5.366E-06	-4.447E-02	2.880E-11
Δt (s)	5.029E-04	1.000E-07	4.371E+01	4.371E-06	-3.622E-02	1.910E-11
Δs (pix)	-3.655E-01	1.271E-02	6.013E-02	7.643E-04	-6.334E+00	5.841E-07
V (m/s)	-2.198E-02					
			$\sum B_x\theta_x$	5.965E-04	$\sum (B_x\theta_x)^2$	6.156E-07
					Bias Error	7.846E-04
					% Bias Error	3.57%

Table A.5: Precision limits of the local streamwise (U) and wall-normal mean velocity (V) at x/h = 3.0 and y/h = 0.3 and 2.0 over the rough wall (SP-24).

Variable	**y/h**	σ_x	K	$P_{x\%}$
U	0.3	6.825E-02	2.0	1.76E-03
	2.0	1.470E-01	2.0	1.32E-01
V	0.3	1.016E-01	2.0	2.62E-03
	2.0	9.304E-02	2.0	8.32E-02

where K is the confidence coefficient and σ is the standard deviation of the sample of N readings of the variable X. To determine the standard deviation, the sample size (6000 image pairs) used in the present study was sub-divided into 10 sets and each set was used to calculate the mean velocities. The standard deviation was then calculated from the 10 readings of the mean velocities at the locations of interest. The results of the precision error analyses are summarized in Table A.5. At 95% confidence level, K = 2. Due to the large sample size used in the present, the precision error is negligible in both the near wall region and the freestream. This implies that the uncertainty in the velocity measurement will largely depend on the bias error.

A.3.3 Total error

The total uncertainty, E, in the result U_i is the RSS of the bias and precision limits, given by

$$E = \sqrt{B_x + P_x} \qquad \text{(A. 5)}$$

The total uncertainty was obtained from the values of the bias and precision errors obtained earlier and equation A.5 to be ± 1.0% and ± 6.3% for U and V, respectively, in the near wall region and ± 0.8% and ± 3.4% for U and V, respectively, in the freestream. The uncertainties in the turbulence intensities and Reynolds shear stress are, respectively, estimated to be ± 7% and ± 10% of the peak values. The uncertainty in the triple velocity products and energy budget terms is estimated to be of the order ±14%.